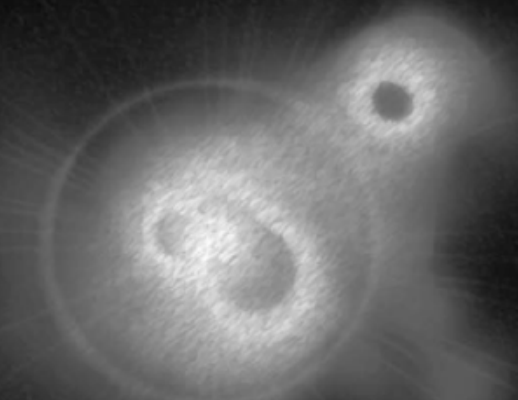


Stellar collisions in young star clusters



Evgenii Gaburov - Stellar collisions in young star clusters - 2008

Evgenii Gaburov

Stellar collisions in young star clusters



Evghenii Gaburov

Stellar collisions in young star clusters

Sterbotsingen in jonge sterrenhopen

ACADEMISCH PROEFSCHRIFT

ter verkrijging van de graad van doctor
aan de Universiteit van Amsterdam
op gezag van de Rector Magnificus
prof. dr. D. C. van den Boom
ten overstaan van een door het college voor promoties
ingestelde commissie, in het openbaar te verdedigen
in de Agnietenkapel
op dinsdag 4 november 2008, te 10:00 uur

door

Evghenii Gaburov

geboren te Chișinău, Moldavische SSR, Sovjet-Unie

Promotiecommissie

Promotores: prof. dr. R. A. M. J. Wijers
prof. dr. P. M. A. Sloot

Co-Promotores: dr. S. F. Portegies Zwart
dr. O. R. Pols

Overige leden: prof. dr. A. R. King
prof. dr. E. van den Heuvel, emeritus
prof. dr. L. Kaper
prof. dr. M. Bubak
dr. Y. Levin
dr. G. D. van Albada



Dit proefschrift werd mede mogelijk gemaakt door financiële steun van NWO.

A la memoria de Mireia Tapiador

Папе и Маме

Contents

1	Introduction	1
1.1	Stellar collisions in star clusters	1
1.2	Outline of the thesis	5
2	Mass segregation in star clusters	9
2.1	Introduction	10
2.2	The Model	11
2.3	Results	14
2.3.1	Core radii	14
2.3.2	Colour gradients	17
2.4	Discussions and Conclusions	17
3	Mass function in the central region of the Arches cluster	21
3.1	Introduction	22
3.2	Dynamical evolution of the mass function	22
3.2.1	Parameters for the simulations	22
3.2.2	Dynamical evolution towards core collapse	24
3.2.3	Post-collapse mass function	26
3.3	Mass function of the Arches cluster	27
3.4	Discussion and conclusions	29
4	Dynamics of the first collision in young star clusters	33
4.1	Introduction	34
4.2	Setup and initial conditions	35
4.3	The circumstances of the first collision	37
4.3.1	The location of the first collision	37
4.3.2	The time of the first collision	38
4.3.3	Mass distributions	43
4.4	The collision geometry	46
4.5	Discussion and conclusions	48
5	Hydrodynamics of the first collision in young star clusters	53
5.1	Introduction	54
5.2	Methods and Conventions	56
5.2.1	SPH code	56
5.2.2	Equations of motion	56

5.2.3	Integration in Time	58
5.2.4	Choice of Units	58
5.2.5	Relaxing a single star	59
5.3	Relaxing a binary star	60
5.4	Initial conditions	63
5.5	Results	67
5.6	Discussion and Conclusions	82
6	Mixing in massive stellar mergers	87
6.1	Introduction	88
6.2	Methods	89
6.2.1	Guiding Principle	89
6.2.2	Sorting method	89
6.2.3	Stability Criterion in High Mass Stars	91
6.3	Validation	92
6.3.1	Initial conditions	92
6.3.2	Results	93
6.4	Discussion and conclusions	97
7	The evolution of runaway stellar collision products	101
7.1	Introduction	102
7.2	Methods	103
7.2.1	Stellar collisions	103
7.2.2	Stellar evolution	104
7.2.3	Mass loss	105
7.2.4	Rotation	106
7.3	Results	107
7.3.1	Structure and size of the merger remnants	113
7.3.2	Final remnant masses	115
7.3.3	Surface abundances and chemical yields	116
7.3.4	Metallicity effects	119
7.4	Discussion and conclusions	120
Summary		123
Samenvatting		127
Acknowledgements		131
List of publications		133
Bibliography		135

Chapter 1

Introduction

1.1 Stellar collisions in star clusters

Observational data and numerical modelling provide strong evidence that most, if not all, stars form in star clusters (Lada & Lada, 2003; Zinnecker & Yorke, 2007). Star clusters can therefore be viewed as fundamental building blocks of the Universe. There is even tentative observational evidence that the Sun was a member of a star cluster (Looney et al., 2006).

It appears that star clusters are formed in a compact state and with a low star formation efficiency, which is the ratio of the total mass of stars to the total mass of both stars and the remaining gas. Star formation is a continuous process which, in the absence of response from young stars, would probably continue until nearly all the gas is converted into stars. However, young massive stars generate enough energy by means of stellar winds, photo-ionising (ultraviolet) radiation and supernova explosions that star formation is switched off and the left-over gas is completely expelled from the cluster within ten million years. A star cluster is considered to be born at the moment when most of the remaining gas is expelled.

The dynamical evolution of such young star clusters is very rich. Since the cluster is abundant in massive stars, the effect called *dynamical friction* heavily affects the motion of stars with the mass much higher than the average mass of stars in the surroundings. A massive star deflects trajectories of low-mass stars, and this generates a wake behind it (Fig.1.1). The net result is that stellar density is higher behind this massive star, and therefore there is a net gravitational force which pulls the star back. As with satellites orbiting the Earth, such a pull results in the decay of the orbit, and after some time, the massive star will reach the central regions of the star cluster, which is called the core. The speed of descent is proportional to the mass of the star. Hence, the most massive stars in a cluster will be the first to reach the core. The cumulative effect of dynamical friction is that the stars are segregated by mass, with high-mass stars concentrated in the centre. Such a cluster is said to be mass-segregated. (Fig.1.2).

Star clusters can also be considered as thermal systems, where central regions are hotter (stars have on average higher kinetic energy) than the

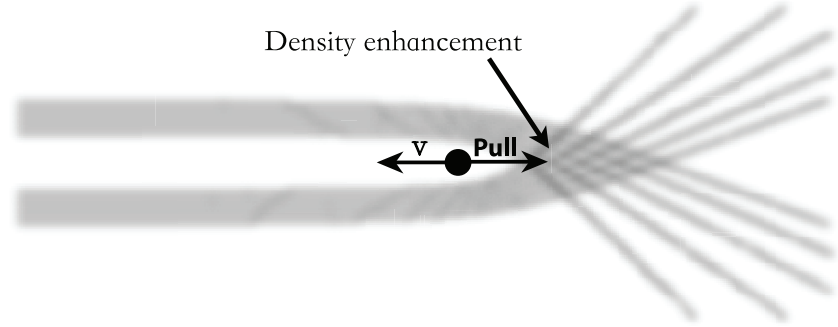


Figure 1.1: As a massive object moves through the field of low-mass stars, the trajectories of these stars deviate from a straight line. This results in the excess of low-mass stars behind the object, which generates a net gravitational pull which slows the object down.

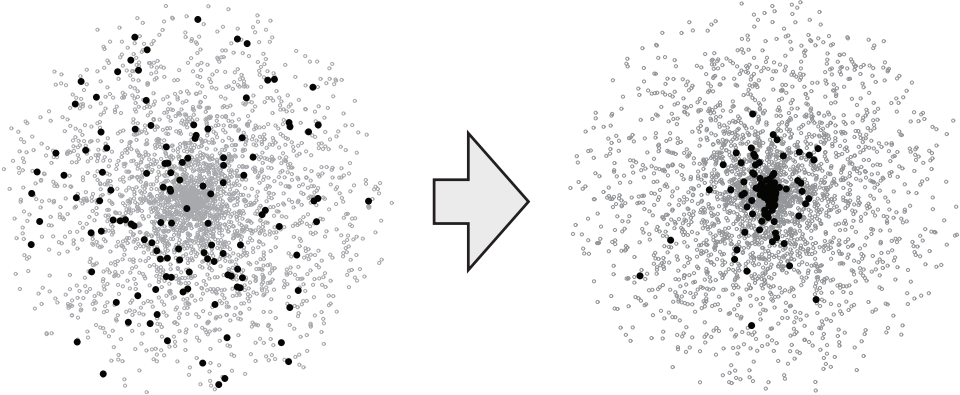


Figure 1.2: Initially, the distribution of both low- (small grey dots) and high-mass stars (large black dots) is the same. However, after some time, the massive stars are mostly found in the centre, whereas low-mass stars are still distributed as before: this is an example of a mass segregation in a star cluster.

outskirts. This can be thought of as stars of a given mass moving faster in the core than outside of it. As with other systems, the laws of thermodynamics apply here as well, and therefore there is heat transfer from the core. However, self-gravitating systems, such as stars or star clusters, have a peculiar property that if heat is lost from a system, its temperature increases: the system becomes *hotter*. It can be thought of in the following way: if a satellite loses its energy by friction with the atmosphere, as in the case of low-orbit satellites, it begins to slow down. However, the loss of

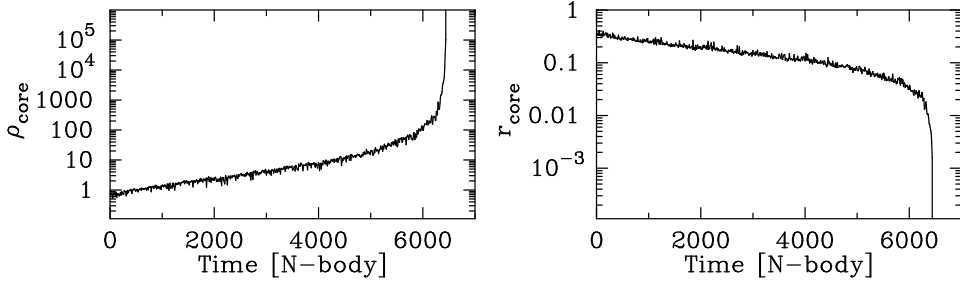


Figure 1.3: Results from N -body simulations of evolution of a star cluster consisting of 32768 equal-mass particles initially distributed according to the Plummer sphere. The left and right panel show time evolution of the core density and radius respectively. The core collapse in this system occurs at $t \simeq 6440$ dynamical time units.

speed results in the decrease of altitude, which means that it starts falling onto Earth; but this actually increases its speed even further, and therefore the speed of the satellite will be increased (becomes hotter). The same applies to the case of a star. When warm (fast moving) stars interact with cold (slow moving) stars, they transfer heat to these cold stars, and instead of slowing down they speed up even further (become hotter) and decay to the core. In this process, the cluster becomes increasingly concentrated: the core becomes smaller and the central density becomes larger. This processes is called *gravothermal instability* (Fig. 1.3). This, in principle, can continue until the core of the cluster becomes indefinitely small and its density reaches infinitely high values, a process which is called *core collapse*. However, in high density environments the occurrence of three-body encounters becomes increasingly probable. The outcome of such an encounter is the formation of a binary (Fig. 1.4). They are basically heat sources which provide enough energy to prevent the core from further collapsing; this is confirmed by both observations and numerical modelling. The further evolution of a star cluster exhibits core oscillations: the periodic collapse and subsequent expansion of the core (Fig. 1.5). This phenomenon is called *gravothermal oscillations*.

The result of both dynamical friction and gravothermal instability is that the core becomes compact enough and sufficiently rich in massive stars, that these stars quickly pair together to form binaries. These massive binaries support the core from further collapse by generating enough heat via interactions with single stars (Fig. 1.6). The result of such interactions is the decrease of the semi-major axis of the binaries. This means that the total energy of the binary decreases, and in order to conserve the total energy of this three-body system, the single star carries away more energy than it brought in. To conserve the total momentum of the system, the binary star

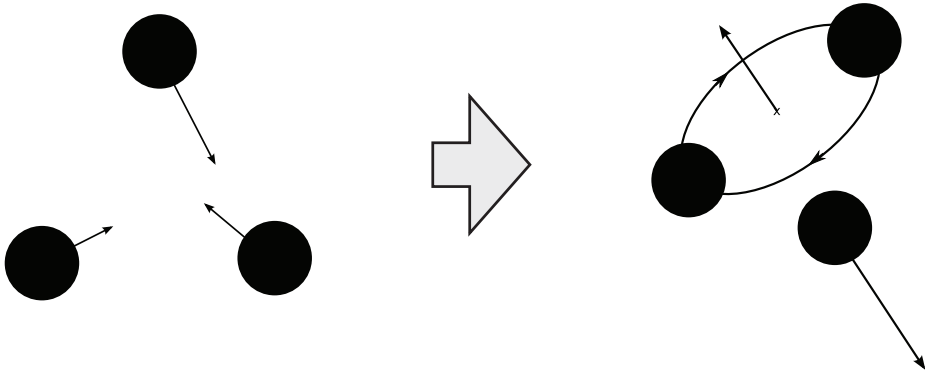


Figure 1.4: Formation of a binary by a three-body encounter. Initially, three unbound stars come close enough that a complicated three-body encounter takes place. After the interaction is complete, two stars form a binary and a third star escapes to infinity.

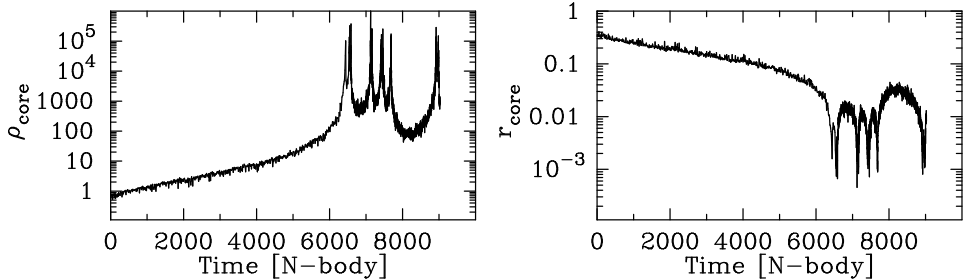


Figure 1.5: Similar to the Fig. 1.3, except that the evolution is followed beyond core collapse. Gravothermal oscillations are apparent for $t > 6440$. The duration of an oscillation is proportional to its amplitude.

recoils, and on occasion recoil velocity could be high enough that the binary is ejected from the core. This therefore deprives the core from the necessary support against collapse, and the core begins to collapse until another binary is formed. This process can be repeated multiple times, and the core could exhibit sporadic oscillations, which may not necessarily be of gravothermal nature.

Since stars are not point mass objects but have a finite radius, this gives the possibility of stellar merger events, when two stars come so close to each other that a physical contact is unavoidable. Indeed, this may happen when a tight binary interacts with an intruder star. In this case, there is a high probability that two of the three stars during this interaction may come into physical contact and merge. In crowded places, such as central regions of star clusters, collisions appear to be natural events (Hills & Day, 1976), and this has been shown in various numerical simulations (Portegies Zwart et al.,

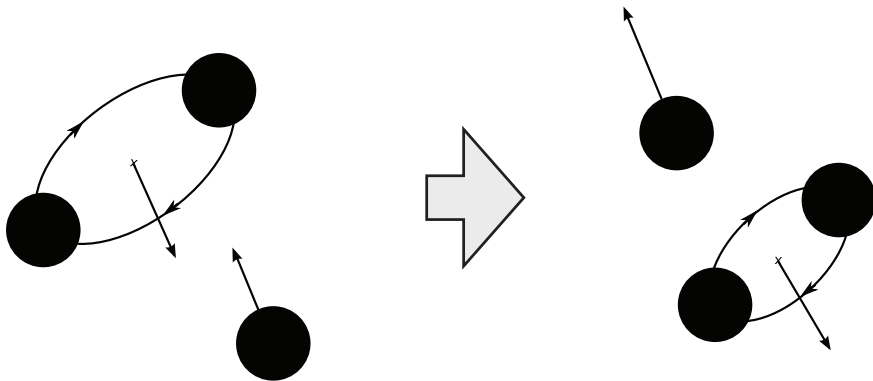


Figure 1.6: A tight binary interacts with a single star. After the interaction, binary semi-major axis decreases and the excess of the energy is removed by a single star.

1999; Hurley et al., 2001; Portegies Zwart et al., 2004; Gürkan et al., 2006; Freitag et al., 2006; Gaburov et al., 2008a).

Stellar mergers may provide a formation channel for non-canonical stars, such as blue stragglers that are observed in both open and globular clusters (Hurley et al., 2005), which cannot be explained by the standard theory of star formation (Stahler & Palla, 2005). In young star clusters, stellar mergers might be responsible for the formation of massive stars which are younger than the rest of the cluster stellar population, such as *The Pistol Star* in *The Quintuplet Cluster* (Figer et al., 1998a). Other massive stars, such as *Sher 25* in the massive Galactic cluster *NGC3603*, may have been formed via binary mergers. Along with the single merger events, some star clusters, such as *Arches* close to the Galactic Centre or *R136* in *The Large Magellanic Cloud*, are dense enough that runaway stellar mergers can occur (Portegies Zwart et al., 2004). During such event, many stars merge in succession and this forms a very massive stellar object with a final mass reaching a thousand solar masses. The outcome of such a runaway merger event is still a matter of debate, but this could be a formation channel for an intermediate-mass black hole—a black hole with a mass $m \gtrsim 10^{2-3} M_{\odot}$, or an extremely luminous supernova explosion (Portegies Zwart & van den Heuvel, 2007).

1.2 Outline of the thesis

This thesis is the result of an attempt to understand stellar collisions in young star clusters by carrying out dynamic, hydrodynamic and stellar evolution calculations.

Chapter 2 sets the scene, by introducing young star clusters. In particular, we introduce the concept of mass segregation and its influence on the integrated photometric properties of a young star cluster. It is sometimes assumed that in a young mass-segregated star cluster, the core radius strongly depends on the colour of light in which it is observed, for the following reason: massive stars are the first stars to leave the main-sequence and become red, and it is therefore assumed that most of the red light comes from the most massive stars, whereas most of the blue light comes from stars of lower mass. Since most massive stars are expected to be found in the centre of the cluster, it is usually assumed that if the star cluster is observed in red colour, its observed core radius will appear smaller than in blue colour. In this chapter, we use an analytical model to quantify the dependence of the core radius on the colour. We find that the dependence is weak, and the reason is that most of the light for *all* colours comes from stars of similar mass, namely those that are located around turn-off point at a given epoch. But stars with similar masses have a similar spatial distribution, and this therefore results in a weak dependence of core radius on the colour. Therefore, integrated photometric properties are not the best tracer of mass segregation in a young star cluster. Nevertheless, mass segregation still may be detectable by studying the colour of a cluster as a function of the distance to the cluster centre.

In **Chapter 3**, we extend the research further by carrying out a set of *N*-body simulations of young star clusters with properties similar to the Arches cluster situated close to the Galactic centre. This study is motivated by an observational result on the mass function in the central regions of this star cluster. In particular, it was found that the mass function in the central region of the cluster can be approximated as a broken power-law, where the slope becomes shallower for $m > 6M_{\odot}$, and this was interpreted as due to mass segregation. By carrying out a set of *N*-body simulations of initially non-segregated star clusters, similar in properties, such as mass and size, to the Arches cluster, we are able to reproduce the observations. In addition, we are able to determine from numerical data the time dependence of the slope of the mass function for massive stars, which allows us to constrain the dynamical state of the Arches cluster.

Stellar collisions are brought to the scene in **Chapter 4**. In particular, we modelled star clusters similar to the Arches, R136 or MGG11 clusters, and studied the occurrence of collisions as a function of cluster size. In this work, we were able to identify the main processes which drive collisions, and in addition we have determined initial conditions of collisions, such as the number of participating stars, their mass and their geometry. We found that the time of the first collision is, in general, similar to the time the massive colliding star takes to reach the centre of the cluster from its birth location. Moreover, these collisions occur between a massive binary and a single star, and they could be qualitatively different from the collisions between two

single stars, which occur in globular clusters. For massive stars, binary formation by a three-body encounter is much more probable than a collision between two stars. Hence, a massive binary is initially formed, and this binary eventually collides with the third, intruder, star. By detailed studies of the simulation data, we were able to construct a set of initial conditions which can be used for further hydrodynamic studies of such collisions.

Detailed hydrodynamic studies of interactions between binary and single stars is presented in **Chapter 5**. The aim of this chapter is to understand the outcome of an event where a tight massive binary is being strongly perturbed by a massive star. In particular, the number of stars which merge, if any, the final configuration of the system after the collision, mass loss during the collision, and most importantly the comparison against the “sticky sphere” approximation which is commonly used in N -body codes to detect stellar merger events. In the latter approximation stars are hard spheres with a prescribed radius, which is usually equal to the radius of a star of a given mass and age. In the “sticky sphere” approximation, a collision is detected when two spheres touch, or in other words when the separation between centres of these spheres is equal to or less than the sum of their corresponding radii.

While Chapter 5 is focused on the global properties of the outcome of stellar collisions, such as mass loss and geometry, **Chapter 6** studies the internal structure of the collision product. In this case, one has to resort to high resolution simulations, which are computationally demanding. We therefore restricted this study to head-on collisions, which are much faster events than binary-single star mergers, and yet capture the most important processes governing mixing and redistribution of stellar fluid. Since collisions between main-sequence stars occur on time scales which are much shorter than the thermal relaxation time-scale, the fluid elements do not have time to exchange heat; therefore, one can resort to a pure hydrodynamic study of such collisions. Using Archimedes’ principle, we found that the fluid redistributes itself such that the fluid with low buoyancy—a quantity which is proportional, but not equal, to entropy—settles, usually, in the centre of the collision product and is surrounded by the fluid with higher buoyancy; in other words, less buoyant fluid is usually below more buoyant fluid. However, if there is a strong chemical composition gradient, it is possible to have a stable configuration of fluid with lower buoyancy on top of the fluid with higher buoyancy. As paradoxical as it may appear on first sight, such a configuration is stabilised by a strong gradient in chemical composition. Since heat exchange was ignored in these calculations, we found that the buoyancy and composition, and therefore temperature, may become multi-valued functions of the radius. This implies that neighbouring fluid elements may have distinctly different values of composition and entropy. Using a semi-analytical method to approximate the structure of a collision product, we found that these multi-valued functions are not

an artifact of the simulations, but are a direct consequence of ignoring the microscopic mixing processes. Therefore, we suggest that the microscopic mixing may be an important component in mergers between massive stars, which is currently missing in such type of calculations.

Finally, in **Chapter 7** we study the scenario of forming an intermediate mass black hole (IMBH) by a runaway stellar merger event. Using runaway sequences from the results of N -body simulations, we study the evolution of a runaway collision product. By approximately modelling the structure of the collision product, as presented in Chapter 6, we followed the evolution of such a product between its subsequent collisions with other stars. In N -body simulations, in which the intermediate evolution of the product is usually ignored, the final mass of the product is about a thousand solar masses at the end of the runaway sequences. However, once stellar evolution is taken into account, strong stellar winds appear to drastically modify this result, such that an IMBH is not likely to be formed by means of runaway stellar collisions.

Chapter 2

Mass segregation in young star clusters: can it be detected from the integrated photometric properties?

Based on:

E. Gaburov and M. Gieles

Monthly Notices of the Royal Astronomical Society, in press

ABSTRACT

We consider the effect of mass segregation on the observable integrated properties of star clusters. The measurable properties depend on a combination of the dynamical age of the cluster and the physical age of the stars in the cluster. To investigate all possible combinations of these two quantities, we propose an analytical model for the mass function of segregated star clusters that agrees with the results of N-body simulations, in which any combination can be specified. For a realistic degree of mass segregation and a fixed density profile, we find with increasing age an increase in the measured core radii and a central surface brightness which decreases in all filters more rapidly than what is expected from stellar evolution alone. Within a Gyr the measured core radius increases by a factor of two and the central surface density in all filters of a segregated cluster will be overestimated by a similar factor if mass segregation is not taken into account during the conversion from light to mass. We find that the $V - I$ colour of mass segregated clusters decreases with radius by about 0.1-0.2 mag, which could be observable. From recent observations of partially resolved extra-galactic clusters, a decreasing core radius with increasing wavelength was observed, which was attributed to mass segregation. However, our models predict that mass segregation has weaker dependence of the core radius on the wavelength, and therefore it is doubtful that the observed dependence can be attributed to the effects of mass segregation. These observations can not be reproduced by our models. In addition, we provide physical arguments based on the evolution of individual stars that one should not expect strong dependence of core radius as a function of the wavelength. We find that the differences between measured radii in different filters are always smaller than 5%.

2.1 Introduction

Observations of star clusters are often used as test-beds for theories of star formation, the stellar initial mass function (IMF) and dynamical evolution. An important ingredient in most of these theories is the differential distribution of stellar masses within a cluster, or *mass segregation*.

In several resolved clusters, evidence of mass segregation has been claimed on the basis of observed variations of the stellar mass function (MF) with distance to the cluster centre (see for example Brandl et al. 1996; Hillenbrand & Hartmann 1998; de Grijs et al. 2002; Stolte et al. 2002 for R136 in 30 Doradus, the Orion Nebula Cluster, clusters in the LMC and the Arches cluster, respectively). These observations claim an overabundance of massive stars in the cluster centre. This stratification of stellar masses is expected from dynamical evolution, since dynamical friction slows down the most massive stars. As a result, these stars sink to the cluster centre on a time-scale that is inversely proportional to their mass. Because the aforementioned clusters are dynamically young, the observations advocate a primordial origin for this segregation of stellar masses.

From the “competitive accretion” star formation model (see for example Bonnell et al. 1997), it is expected that the most massive stars form in the highest density environments, corresponding to the inner parts of the clusters. The preferential formation of massive stars in the centre of the cluster is often used to explain the observations of dynamically young, but mass segregated clusters.

The determination of the stellar MF in different annuli around the cluster centre, which is the most common technique used to “detect” mass segregation in resolved clusters, is hampered by several observational difficulties. First, crowding and blending of stars in the core can mimic a shallower MF at that location (Maíz Apellániz, 2008; Ascenso et al., 2007). Second, the determination of stellar masses from the observed luminosities depends on the adopted age, which is usually taken constant for all stars in the cluster. However, only a small spread in age is enough to cause misinterpretations (see Hunter et al. 1995, who show that the MF of the R136 cluster is consistent with Salpeter when this effect is taken into account).

Alternatively, integrated properties, such as the surface brightness profile in different filters can be employed to study radial variations of the stellar MF. In this way one does not have to rely on individual star counts, thus avoiding possible biases; moreover, this method can be used for clusters at larger distances. It was shown that metal-rich (red) star clusters appear to have smaller half-light radii than their metal-poor (blue) counterparts (Jordán, 2004). In addition, one could expect that segregated star clusters appear larger in the ultra-violet (UV) than in the near infra-red (NIR) as most of the light at these red wavelengths comes from the massive stars, whereas the bluer wavelengths are dominated by intermediate mass stars.

Tentative evidence for this is given by McCrady et al. (2005) who find a decreasing half-light radius, or effective radius (r_{eff}), with increasing wavelength for the young massive cluster M82-F. Larsen et al. (2008) find for NGC 1569-B that the r_{eff} measured in the U -band is around 30-50% larger than the r_{eff} measured in the I -band. A smaller radius in the redder filters is qualitatively what one would expect when the massive (red) stars are more centrally concentrated, but it has thus-far not been quantified how large the expected difference is.

Although the integrated properties are free of the biases that are encountered in methods that rely on individual star counts, there are other problems such as variations of the point spread function (PSF) between the different filters (Larsen et al., 2008), differential foreground extinction (Bastian et al., 2007) and intra-cluster extinction (Stolte et al., 2002), that make it a challenging task to accurately determine intrinsic differences between the cluster properties in different filters.

To quantify the expected variations in different filters, we present a method to rapidly simulate integrated luminosity profiles of a mass segregated star cluster in different filters. We choose to do this analytically to avoid statistical fluctuations which one has to deal with when considering (realistic) N -body systems, and therefore we do not include the dynamical evolution. Instead, we apply our method to clusters with different concentrations, which may result from dynamical evolution.

In Sect. 2.2 we introduce a model of the mass function of a segregated star cluster and in Sect. 2.3 we present simulated observational properties of such clusters. A discussion and our conclusions are presented in Sect. 2.4.

2.2 The Model

Recent numerical (Portegies Zwart et al., 2007a; Gaburov et al., 2008b) and observational (Kim et al., 2006) results suggest that the mass function in the inner parts of young (dynamically) segregated star clusters has a broken power-law form with the slope on the high mass end being shallower. We assume a segregated mass function (SMF) of the following form. For $r < r_{\text{hm}}$, with r_{hm} being the cluster's half-mass radius in three dimensions, the SMF is

$$g(m, r) \propto \begin{cases} m^{\alpha_0}, & m_{\text{lo}} < m < \mu = 2\langle m \rangle_0, \\ \mu^{\alpha_0} \left(\frac{m}{\mu}\right)^{\alpha(r)}, & \mu < m < m_{\text{up}}. \end{cases} \quad (2.1)$$

Here $\langle m \rangle_0$ is the mean mass of the initial MF (IMF), r is the distance to the cluster centre, α_0 is the index of the IMF which is assumed to be a power-law, m_{lo} and m_{up} are the lower and upper limits of the MF, respectively, and $\alpha(r)$ is the r dependent power-law index of the SMF at the high-mass end. The outer part of the SMF ($g(m, r > r_{\text{hm}}) = g_\infty(m)$) does not depend

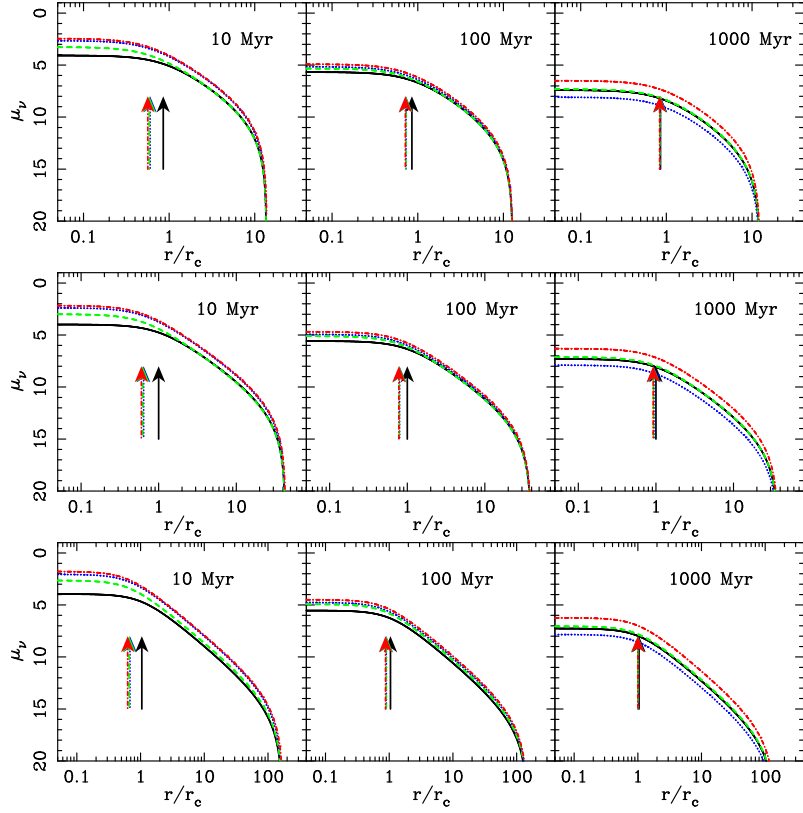


Figure 2.1: Surface brightness as a function of a distance to the cluster centre, which is given in units of core radius of non-segregated star cluster. The dotted blue line shows a surface brightness profile in U -band, dashed green line is for V -band and dash-dot red line is for I -band. The black line represents the surface brightness profile of a non-segregated cluster in V -band. The mass density profile for all the clusters of different ages is kept the same. The density profiles are King models with $W_0 = 5, 7$ and 9 for top, middle and bottom panels, respectively.

on the distance to the cluster centre. It can be uniquely constructed in such a way that the integrated cluster mass function results in the IMF, which we assume to be a Salpeter (1955) mass function between $0.15M_\odot$ and $100M_\odot$. In other words, the excess of massive stars in the centre of the star cluster occurs at the expense of reducing the number of these stars in the outer regions.

The form of the mass function depends on the choice of the index $\alpha(r)$, which can be arbitrary. Guided by N -body simulations (Portegies Zwart et al., 2007a), we choose the following “Ansatz”

$$\alpha(r) = \frac{\alpha_c - \alpha_\infty}{1 + \left(\frac{r}{r_c}\right)^{\frac{3\phi}{2}}} + \alpha_\infty. \quad (2.2)$$

Here α_c is a free parameter determining the degree of mass segregation in the cluster centre, ϕ is a free parameter that specifies the functional form of $\alpha(r)$, r_c is the core radius of the underlying density profile $\rho(r)$, and α_∞ is a parameter which is constrained by the condition that the mean stellar mass is a continuous function of r , so that there is no jump at r_{hm} . For a given $\rho(r)$ there is a maximum possible α_c that can be achieved in our model in order to satisfy the constraint set by the initial MF. We compute this maximum α_c by solving $g_\infty(m_{\text{up}}) = 0$. Physically, this means that the most massive stars from the outer region are already in the inner region. Therefore, any further increase in α_c will result in a negative $g_\infty(m)$ for some m below m_{up} , and this is clearly an unphysical situation.

Given $g(m, r)$ and $\rho(r)$ we can calculate the surface brightness profile in different broad-band filters. We use the Padova isochrones for solar metallicity ($Z = 0.019$) (Bertelli et al., 1994; Girardi et al., 1996, 2000) and the conversion to the Johnson-Cousins-Glass $UBVRIJHK$ photometric system (Girardi et al., 2002) to convert mass to light. Our results do not depend on the adopted metallicity. Also, we explicitly note that all stars in the cluster have the same age and metallicity, which might be an oversimplification, since star cluster with multiple populations are known, both young (for example Mackey et al. 2008) and old (for example Piotto et al. 2007). The spatial luminosity profile in a filter centred at wavelength λ , $L_\lambda(r)$, is computed using the following conversion $L_\lambda(r) = \rho(r)[l_\lambda(g(m, r))/\langle m \rangle(r)]$, in which $\langle m \rangle(r) = \int m g(m, r) dm$ is the mean stellar mass as a function of r , and $l_\lambda(g(m, r)) = \int L_\lambda(m) g(m, r) dm$ with $L_\lambda(m)$ being the luminosity of a star of mass m in a filter with central wavelength λ .

We used a series of King (1966) models parameterised by a scaled central potential W_0 (Binney & Tremaine, 1987) as the input density profiles; these models were generated by the `starlab` software package (Portegies Zwart et al., 2001)¹. We obtain the projected core radius and the surface brightness profile by fitting a King (1962) profile to our models after projecting them in 2D.

Currently, our model contains three free parameters: W_0 , α_c , ϕ . However, by considering only the maximal value of α_c , we reduce the number of free parameters to two because the index α_c is constrained by W_0 . In this case, the value of α_c corresponds to the maximum degree of segregation which is reached at the moment of core collapse and remains roughly constant after that (Portegies Zwart et al., 2007a; McMillan et al., 2007). Our results can therefore be considered as upper limits, since smaller values for α_c will weaken the imprint of mass segregation on the integrated properties. We focus our studies on King models with $W_0 = 5, 7, 9$. We find that the simulated properties depend weakly on the value of W_0 . Fitting Eq. 2.2 to N -body simulations (Portegies Zwart et al., 2007a), we find that $\phi \simeq 0.3$.

¹<http://www.manybody.org/starlab>

Nevertheless, our numerical experiments show weak dependence of the integrated properties on this parameter. Thus, we generally present our results for $\phi = 0.5$ unless mentioned otherwise.

Even though there are other methods which include mass segregation in star cluster models (Šubr et al., 2008; Marks et al., 2008), we prefer this broken power-law approximation because it was found in dynamical simulations. In addition, we also provide physical argumentation based on stellar evolution why our results are not expected to be sensitive to stellar metallicity and the details of the model of mass segregation.

2.3 Results

Our aim is to understand the effect of mass segregation on the observed size of clusters, particularly on r_c and the surface brightness profiles in different filters, as a function of age. In addition, we study the radial variation of colour, since it is expected that the central part of the cluster is redder than the outer parts, due to the overabundance of massive (red) post main-sequence stars there (Fleck et al., 2006). We note that we allow the stars to evolve while fixing the density profile, which is of course not realistic from a dynamical point of view. In reality, the measurable properties of mass segregated clusters will result from a complex interplay between mass loss by stellar evolution and dynamical relaxation processes. Such models only allow the choice of one combination of dynamical and physical age making the exploration of the full parameters space too time-consuming for the scope of this study. We refer the reader to the studies of Hurley (2007) and Mackey et al. (2007) as examples of full N -body studies that take into account stellar evolution and the effects of projection.

2.3.1 Core radii

Mass segregated star clusters have an excess of massive stars in their central regions. As a result, they are expected to appear smaller in the NIR than in UV (Sternberg, 1998), since the light at these wavelengths is dominated by massive stars. If this is correct, it may provide a robust method for determining mass segregation in slightly resolved (extra-galactic) star clusters at distances up to several Mpc.

In Fig. 2.1 we show for different ages the surface brightness profiles for mass segregated clusters with different density profiles in the U , V and I filters resulting from our model (Sect. 2.2). We use the same $\rho(r)$ at all ages in order to eliminate effects related to the dynamical evolution of the cluster.

At an age of 10 Myr the difference in r_c between the U and I filter is just 6%, with the smallest radius in the I -band. The difference between the true and observed core radius is roughly a factor of two, with the measured

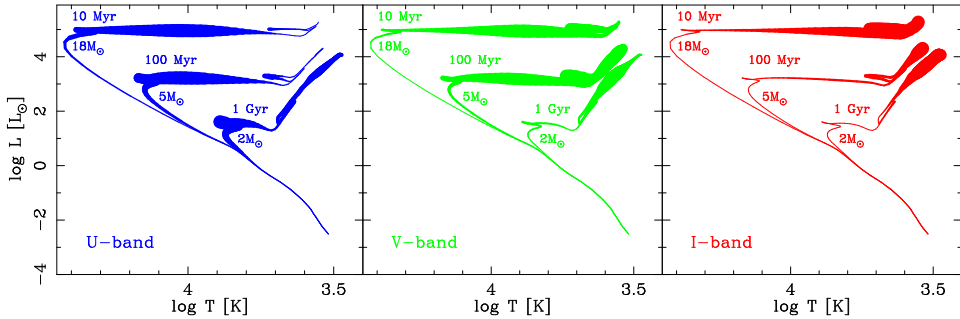


Figure 2.2: Hertzsprung-Russell diagram of stellar isochrones in different filters. The thickness of the line represents the contribution to the cumulative luminosity function, that is $L_\lambda(m)p(m)$ in which $p(m)$ is the initial mass function.

radius being smaller. This is because the massive stars dominate the light in all filters and are overabundant in the centre. In the course of time, massive stars leave the main-sequence and become dark objects, such as black holes or neutron stars, which results in an apparent increase of the core radius. The observed core radii become roughly 80% of the true core radii at this age and the difference between core radii in the different filters has nearly disappeared. Finally, at 1 Gyr the light is dominated by red-giant and AGB stars. The turn-off point is close to $2 M_\odot$ and the light-to-mass ratio in the core is close to unity. We find that the observational core radius is 10% smaller than the true core radius, thus providing a good estimate of the true r_c . However, it is unclear whether at 1 Gyr the mass function can still be represented by a broken power-law (Eq. 2.1). In fact, the recent results suggest that in globular clusters, it is the low-mass part of mass function which becomes r dependent (De Marchi et al., 2000; Baumgardt & Makino, 2003). We note that in our model we have assumed that the mass of all remnants is retained, that is, we do not take into account kick velocities, and the mass of the remnant we estimate from its zero age main sequence mass (Eggleton et al., 1989; Portegies Zwart & Verbunt, 1996)

The *apparent* increase of r_c with age implies that light is not a good tracer of mass for young mass segregated clusters. Mackey & Gilmore (2003) observed a clear trend of increasing core radius with age, which can be partially explained by the effect of mass segregation making the younger clusters appear more compact. However, dynamical effects, such as heating by black hole binaries (Merritt et al., 2004a; Mackey et al., 2007) are still required to fully explain the observed trend of the increasing r_c with age for the LMC clusters.

In the lower panel of Fig. 2.3, we show the time evolution of the difference between the true r_c and the observed r_c in the U , V and I filters, as well as the r_c computed from the bolometric surface brightness profile. As we have

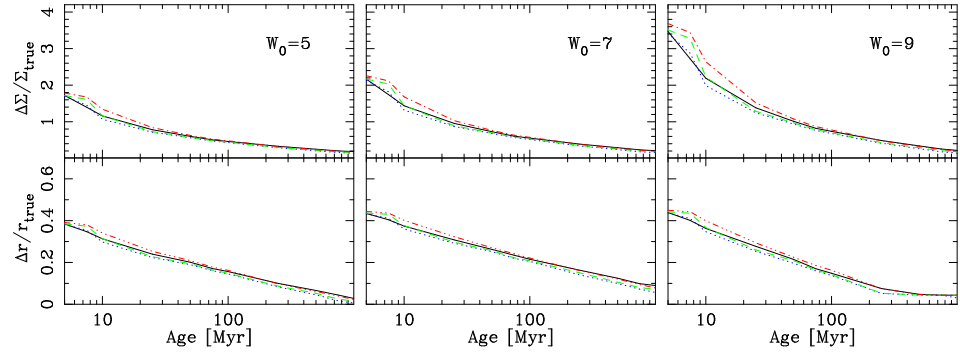


Figure 2.3: Upper panel: The overestimate of the observed central surface density, $\Delta\Sigma = \Sigma_{\text{obs}} - \Sigma_{\text{true}}$, compared to the true central surface density in mass segregated star clusters as a function of age. The solid black line displays the overestimate assuming bolometric light-to-mass ratio (dotted blue line is for light-to-mass ratio in U filter, dashed green line is for V filter, and dash-dotted line is for I filter). Lower panel: The underestimate of the observed core radius, $\Delta r = r_{\text{true}} - r_{\text{obs}}$, compared to the true core radii as function of age. The notation is the same as in the upper panel. The density profiles are King models with $W_0 = 5, 7$ and 9 for left, middle and right panels.

shown before, the difference between the true and the observed r_c decreases in the course of time from roughly 50% at 10 Myr to about 10% at 1 Gyr. This result is quite robust showing only a weak dependence on the choice of the parameters W_0 and ϕ .

The reason that the core radii are similar at all wavelengths can be understood from some simple arguments. The light in all filters is dominated by stars with masses slightly above the turn-off mass (Fig. 2.2). The red filters are dominated by giant stars at all ages. The optical and blue filters are also dominated by stars that are close to the turn-off point and not by the stars on the main-sequence. This is because the increase of the light-to-mass ratio with mass is much stronger than the decrease of the number of stars, and this holds for any realistic MF. That is, stars of similar mass dominate the light in all the filters at all ages. However, since stars of similar mass have similar spatial distribution in a mass segregated star cluster, the differences in the observed core radii are small. In the case of mass segregation, MF is a function of the distance to the cluster centre, r , such that the mean stellar mass decreases with r . Since most of the light comes from stars of similar mass, independent of the shape of the MF, the observed core radii are weakly dependent on how mass segregation is implemented.

The light-to-mass ratio in the centre of a segregated cluster can be several times larger than that of a simple stellar population (SSP) of the same age. Usually, the central *mass* density of a star cluster is estimated by using the light-to-mass ratio of an SSP model corresponding to the age of the

cluster to convert the surface brightness profile to a surface density profile. Since in segregated clusters the light-to-mass ratio in the centre is higher, the central density will be overestimated. If the observed central surface brightness is μ , one can compute the “observed” central surface density, $\Sigma_{\text{obs}} = (M/L)_{\text{ssp}}\mu$. The true surface density in the centre, Σ_{true} , we obtain from the input density profile. The relative difference between these two quantities is displayed in Fig. 2.3. Deviations from one are most prominent in the first 100 Myr, where the maximum difference is about a factor of two, and this is not a sensitive function with respect to ϕ . However, in more concentrated clusters, $W_0 = 9$, the density overestimation is larger by an additional factor of two (Fig. 2.3)

Our findings could explain the observed trend of decreasing central surface density with age in a sample of LMC and SMC clusters (Noyola & Gebhardt, 2007). If star clusters are born with a high central concentration, their central 3D density will be overestimated by nearly an order of magnitude.

2.3.2 Colour gradients

An additional tracer of mass segregation is the colour of a star cluster as a function of the distance to the cluster centre. Using a gas dynamics code, Fleck et al. (2006) studied mass segregation in young star clusters and found that the $V - K$ difference between the inner and outer part of the cluster is roughly 0.1 magnitude in the first few 10 Myr, with the inner parts being redder. This difference, though small, might be observable.

In Fig. 2.4 we display the colour as a function of r at different ages resulting from our models. The colour gradients has a notable dependence on ϕ and, therefore, we covered three different values of ϕ : 0.3, 0.5, and 0.7. Note that these three cases are all for the maximum degree of mass segregation, that is set by α_c . The value of ϕ controls the change of the MF with r and the colour variations are sensitive to the value of ϕ . In all cases, the largest colour gradient is observed only for the clusters with ages younger than a few times 10 Myrs. The largest colour gradient of $V - I$ is roughly 0.2 magnitude, whereas the gradient of $U - B$ is barely observable. The clusters with high concentration exhibit higher colour gradient than the cluster with low concentration. In the course of time, however, the colour gradients become less prominent. We, therefore, expect that mass segregation might be detectable in young (< 100 Myr) star clusters through radial colour variations in $V - I$ or $V - K$.

2.4 Discussions and Conclusions

We have simulated observational properties of mass segregated star clusters with the aim to quantify the imprint of mass segregation on integrated

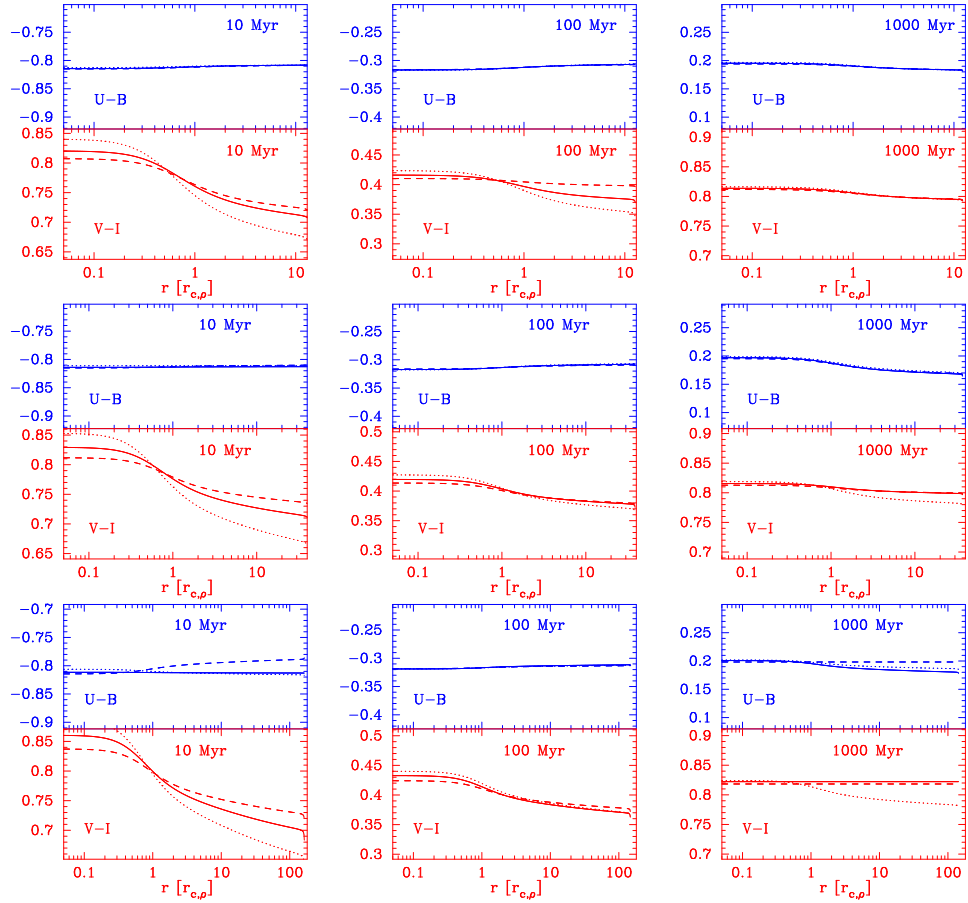


Figure 2.4: Colour of the cluster as a function of projected distance to the cluster centre. The upper three panel shows $U - B$ colour, whereas the lower panel displays $V - I$ colour. The solid line represent displays colours of the cluster if $\phi = 0.5$, dashed line for $\phi = 0.3$ and dotted line for $\phi = 0.7$. The top panels use the King density profile with $W_0 = 5$, while the middle and bottom panels use King profiles with $W_0 = 7$ and 9 respectively.

cluster properties. We choose to model the segregated mass functions analytically based on results from observations and N -body simulations. In order to calculate upper limits of the imprint of mass segregation, we only considered clusters with the maximum possible degree of segregation which can be achieved in our model. While this may not necessarily be reached through dynamical evolution, one may think of this setup as the result of a combination of primordial segregation combined with dynamical evolution.

In young (~ 10 Myr) star clusters, we find only small differences ($\lesssim 5\%$) between the core radius (r_c) found in different filters, and the differences becomes smaller for older clusters. The explanation for these small differences

is that the most massive stars dominate the light in all filters at all ages. It, therefore, appears that the comparison of the measure r_c in different filters is not a particularly suitable tool to look for mass segregation in star clusters and, therefore, we do not expect that one could study whether the young star cluster is in core-collapse phase by using the light alone (Kim et al., 2006; Portegies Zwart et al., 2007a).

The observed r_c is underestimated for young segregated star clusters. The difference with the real r_c decreases with age and is only 10% at 1 Gyr compared to nearly a factor of two at 10 Myr and this does not depend on the cluster concentration. The same factor was found for the half-light radius in gasous models of mass segregated clusters by Boily et al. (2005).

The underestimation of r_c results in an overestimation of the observed central density. This is because the light-to-mass ratio in the centre of a segregated cluster can be an order of magnitude higher than that of a simple stellar population without segregation and, therefore, central 3D mass density might be overestimated by nearly an order of magnitude. However, due to the projection the measured central surface density is overestimated by a factor of three, and this result slightly depends on the choice of W_0 . In particular, for clusters with high concentration the central density might be overestimated by nearly an order of magnitude. These results are consistent with the finding of Boily et al. (2005).

The observed central surface and core radius approached its true value around 1 Gyr. We therefore conclude that light is not a good tracer of mass in young (< 100 Myr) star clusters that are segregated and this effect should be taken into account when trends of r_c or central surface density with age are discussed (Scheepmaker et al., 2007; Noyola & Gebhardt, 2007; Bastian et al., 2008). For clusters with ages above 100 Myr these differences are smaller than 20%.

It is possible to observe mass segregation by looking at colour differences between the inner and outer parts of star clusters. We find that our simulated clusters have $V - I$ differences of roughly 0.1-0.2 magnitude between the centre and the outer part of the cluster. This effect has been observed by Larsen et al. (2008) in the ~ 20 Myr old massive cluster NGC 1569-B. The colour difference decreases at older ages.

We would like to stress that our analytical results for the surface brightness profiles represent an observational best case scenario. From the observational data, the accuracy of the r_c determination will be limited by photon noise, and perhaps more importantly, by stochastic effects in the stellar IMF. Several studies have quantified the effect of stochastic fluctuations (see for example Lançon & Mouhcine 2000; Bruzual 2002; Cerviño & Luridiana 2004). Lançon & Mouhcine (2000) determine the age dependent minimum mass a cluster should have, such that the relative fluctuations around the mean flux, σ_L/L , is less than 10%, corresponding to roughly 0.1

mag photometric uncertainty². When flux is determined in the V -band, this minimum mass at ages of [10, 50, 200, 1000] Myr is $[10^5, 2 \cdot 10^4, 10^4, 6 \cdot 10^3]$ M_\odot .

We predict that the most prominent feature of mass segregation in the integrated properties is a 0.1 mag difference in $V - I$ colour (Fig. 2.4) between the inner part and the outer part. In order to be able to report a detection of this difference, one needs an uncertainty of $\sigma_{V-I} \ll 0.1$ mag and we adopt $\sigma_L/L \simeq 0.01$.

Lançon & Mouhcine (2000) show that σ_L/L scales with $(\sqrt{N}L)^{-1} \propto N^{-3/2}$, since $L \propto N$. This implies that the minimum masses quoted above have to be a factor $(0.1/0.01)^{2/3} \simeq 4.6$ higher to be able to distinguish a radial colour variations due to mass segregation from stochastic fluctuations due to IMF sampling. For the 10 Myr case this implies a minimum mass of $\sim 5 \times 10^5 M_\odot$. This means it will be difficult to detect mass segregation in young massive Galactic clusters, such as the Arches clusters or Westerlund 1. Even the cluster R136 in the 30 Doradus region in the Large Magellanic Cloud is probably of too low mass to detect mass segregation. R136 is probably a special case anyway, since it does not have red evolved stars, which all of our models do have. Young clusters more massive than $\sim 5 \times 10^5 M_\odot$ are known, for example in the Antennae galaxies (Whitmore & Schweizer, 1995) and M51 (Larsen, 2000; Bastian et al., 2005), but these are too distant ($\gtrsim 10$ Mpc) to be able to determine a colour gradient in the light profile. There are probably only a handful of candidate clusters that are resolved enough such that a colour gradient can be observed, for example some of the young massive cluster in M82 (O'Connell et al., 1995), the massive “young globular cluster” in NGC 6946 (Hodge, 1967; Larsen et al., 2002) and a few clusters in M83 (Larsen & Richtler, 2004).

An alternative method to detect differences in the IMF between the inner and outer parts would be to determine the spectral properties. If this can be done without changing instrument set-up, then no problems with changing PSFs or weather conditions should affect the observations. It would, therefore, be interesting to investigate which spectral range would be most sensitive to changes in the slope of the IMF.

Acknowledgements

We thank Nate Bastian for ideas and suggestions, Simon Portegies Zwart, Henny Lammers, Søren Larsen and Andres Jordán for helpful discussion. EG is supported by NWO under the grant #635.000.303.

²Photometric uncertainty is calculated from the flux uncertainty in the following way, $\sigma_V = -2.5 \log(1 + \sigma_L/L)$ mag.

Chapter 3

The present day mass function in the central region of the Arches cluster

Based on:

S. Portegies Zwart, E. Gaburov, H.-C. Chen and M. A. Gürkan
Monthly Notices of the Royal Astronomical Society, 378L, 29, 2007

ABSTRACT

We study the evolution of the mass function in young and dense star clusters by means of direct N -body simulations. Our main aim is to explain the recent observations of the relatively flat mass function observed near the centre of the Arches star cluster. In this region, the power law index of the mass function for stars more massive than about $5\text{--}6 M_{\odot}$ is larger than the Salpeter value by about unity; whereas further out, and for the lower mass stars, the mass function resembles the Salpeter distribution. We show that the peculiarities in the Arches mass function can be explained satisfactorily without primordial mass segregation. We draw two conclusions from our simulations: 1) The Arches initial mass function is consistent with a Salpeter slope down to $\sim 1 M_{\odot}$, 2) The cluster is about half way towards core collapse. The cores of other star clusters with characteristics similar to those of the Arches are expected to show similar flattening in the mass functions for the high mass ($\gtrsim 5 M_{\odot}$) stars.

3.1 Introduction

The mass function of a star cluster changes because of both stellar evolution and stellar dynamics. Stellar evolution causes the turn-off mass to decrease as the most massive stars evolve away from the main sequence, ascend the giant branch to ultimately shed their envelopes to turn into compact objects. Stellar evolution therefore has a characteristic effect on the mass function by truncating it at the high mass end.

The dynamical evolution of a cluster has a more complicated effect on changes in the mass function. The dominant effect here is dynamical friction, which causes the most massive stars to sink to the cluster centre on a time scale that is inversely proportional to the stellar mass, i.e. the most massive stars tend to sink more quickly than relatively lighter stars. At the same time, stars less massive than the average mass tend to leave the inner regions. As a result of this *mass segregation*, the local stellar population becomes a function of the distance to the cluster centre.

Mass segregation, though mostly noticeable in the cluster's central regions, is a global phenomenon. A star cluster that is born with the same mass function across its radial coordinate will gradually grow a top-heavy mass function in its centre and a top-depleted mass function in its outskirts. Near the half mass radius, the mass function remains closest to the initial mass function (Vesperini & Heggie, 1997).

In this chapter, we concentrate on the evolution of the stellar mass function in the inner part of young and dense star clusters, using N -body simulations. Our interest in this topic was initiated by the recent accurate measurements published by Stolte et al. (2005); Kim et al. (2006) in which the mass function in the inner $\sim 10''$ from the centre of the Arches star cluster was studied. These observations, especially the latter, revealed that the mass function of near the centre of Arches cluster is a broken power law, with the turning point $m_p \sim 5-6M_\odot$. We were able to reproduce this feature without invoking any special mechanism. Our simulations allow us to draw conclusions on the history of the dynamical evolution of the Arches cluster.

3.2 Dynamical evolution of the mass function

3.2.1 Parameters for the simulations

As a cluster evolves, stars more massive than the mean mass $\langle m \rangle$ tend to sink to the cluster centre whereas lighter stars move outwards. For the most massive stars, the time scale for dynamical friction is proportional to two-body relaxation time, t_r :

$$t_{\text{df}} \propto \frac{\langle m \rangle}{m_*} t_r, \quad (3.1)$$

were m_* is the mass of the massive star, which segregates inwards. The value of the relaxation time at the cluster's half-mass radius, r_h is given by (Spitzer, 1987, eq. 2.63)

$$t_r = \frac{0.138N}{\ln \Lambda} \left(\frac{r_h^3}{GM} \right)^{1/2}. \quad (3.2)$$

Here G is Newton's constant of gravity, M and N are the total mass and the number of stars in the cluster and $\ln \Lambda$ is the Coulomb logarithm, for which we adopt $\ln \Lambda = \ln(0.01N)$ (Giersz & Heggie, 1996). For the central relaxation time, we use

$$t_{rc} = \frac{\sigma_{3D}^3}{4.88\pi G^2 \ln \Lambda n \langle m_c \rangle^2}, \quad (3.3)$$

where σ_{3D} , n and $\langle m_c \rangle$ are the three-dimensional velocity dispersion, number density and average stellar mass at the cluster centre (Spitzer, 1987, eq. 3.37).

We follow the dynamical evolution of our models by means of direct N -body simulations, which we carry out with the **starlab** software environment (Portegies Zwart et al., 2001). The calculations are performed on the GRAPE-6 special purpose computer (Makino et al., 1997; Makino, 2001).

Our numerical experiments are performed with $N = 12288$ and 24576 stars. For each N , we perform simulations starting with a full range of density profiles for which we chose King (1966) models with the dimensionless parameter W_0 ranging from 3 to 12. The mass function in our simulations is described by a power-law, $dN/dm = m^x$, where we adopt the Salpeter value for the index ($x = -2.35$), with masses ranging from $1 M_\odot$ to $100 M_\odot$. In this way, the total mass of simulated clusters is $M \simeq 5 \cdot 10^4$, which is consistent with the mass of the Arches cluster. To validate our results, we carried out additional simulations with $N = 49152$ as well as with a Salpeter mass function with $0.1 M_\odot$ as the lower limit. It will turn out that the presence of a tidal field has little effect on the results, but reducing the lower limit of the initial mass function to $0.1 M_\odot$ has a profound effect on the results, as we discuss below. For clarity we mainly focus on the models with 12288 and 24576 stars. With these parameters, the relaxation time at the virial radius for the 12k models is about 360 N -body time units, whereas for the 24k models this is 625 N -body time units (see Heggie & Mathieu (1986)¹).

The close proximity of the Arches cluster to the Galactic centre (Cotera et al., 1992, 1996) would seemingly require the simulations to include tidal effects. And for understanding the dynamics in the cluster outskirts or the evaporation time scale the tidal field will prove crucial. For studying

¹For the definition of an N -body unit see http://en.wikipedia.org/wiki/Natural_units.

the evolution of the central region on the short time scale reported here, however, the tidal field has negligible effect. We support this statement by carrying out additional simulations which include the tidal field, and those show no discernible effect. We therefore focus on the results of simulations without a tidal field. This has the attractive side effect that it allows us to scale our results with respect to N . We also ignore the effects of stellar evolution. This approximation is justified since on the short lifetime of the cluster (2 ± 1 Myr) even the most massive stars remain on the main sequence, though some effect of the stellar mass loss at the top end of the mass function can be expected. For example, a $60 M_{\odot}$ zero-age main sequence star with solar metalicity loses about $3 M_{\odot}$ in its first ~ 2.4 Myr (Lejeune & Schaerer, 2001), which has a negligible effect on the slope of the mass function.

3.2.2 Dynamical evolution towards core collapse

In our simulations we identify the moment of core collapse as soon as a persistent binary forms with a binding energy of at least $100 kT$ (where the energy scale kT is defined by the condition that the total stellar kinetic energy of the system, excluding internal binary motion, is $\frac{3}{2} N kT$). For a cluster with a mass function that is consistent with the observed mass function in young star clusters, core collapse occurs at a more or less constant fraction of the initial central relaxation time $t_{cc} \sim 0.2 \pm 0.1 t_{rc}$ (Portegies Zwart & McMillan, 2002; Gürkan et al., 2004). In Fig. 3.1 we plot the moment of core collapse as a function of the initial concentration of the cluster. The slight dependence of t_{cc}/t_{rc} on W_0 , as well as the offset between our results with those of Gürkan et al. (2004) is presumably mainly caused by their broader range of stellar masses ($0.2 < m/M_{\odot} < 120$) in the initial mass function, whereas here we adopt an initial mass function with $1 < m/M_{\odot} < 100$. An additional effect is expected from the difference in the number of stars. The simulations of Gürkan et al. (2004) were carried out with 10^6 particles. The systematic difference between our results from simulations with 12k and 24k stars shows that this also affects the results systematically. At this moment, however, we cannot quantify this effect.

Dynamical friction causes the massive stars to segregate to the cluster centre making the mass function flatter at the higher end, in this region, until the formation of a hard binary. In Figure 3.2 we illustrate the evolution of the mass function between r_{core} and $2r_{core}$. We show the mass function at birth (top curve, the Salpeter mass function), halfway to core collapse and at core collapse (bottom curve). We denote the point around which the slope of the mass function changes by m_p , and the power-law indices in higher and lower ends by $x_{m < m_p}$ and $x_{m > m_p}$, respectively. The apparent decrease in the number of stars in the mass function presented in Figure 3.2 is the result of the cluster becoming more concentrated which causes the adopted annulus ($r_{core} < r < 2r_{core}$) to become narrower.

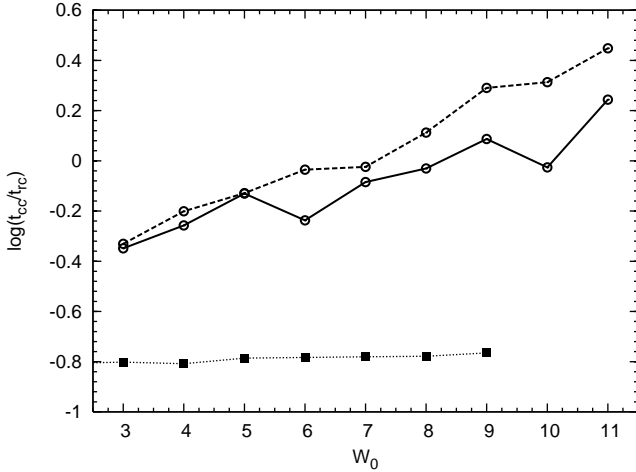


Figure 3.1: The moment of core collapse (t_{cc}) in units of the core-relaxation time (t_{rc}) as a function of concentration parameter, W_0 . The dashed curve gives the results of our simulations with 12k stars and the solid curve with 24k. Since we performed only one simulation per set of initial conditions no error bars are presented. The bottom (dotted) line denote the results of Gürkan et al. (2004).

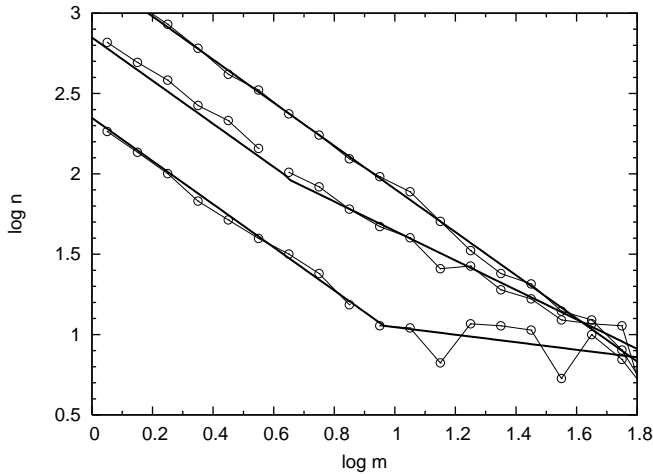


Figure 3.2: The mass function of one of the simulations ($N = 24k$, $W_0 = 5$) for an annulus $1 < r/r_{\text{core}} < 2$, around the cluster centre. From top to bottom, the curves are at times $t = 0$, $t \simeq 0.61t_{cc}$, and $t \simeq 1.05t_{cc}$. The solid lines are least squares fits to the mass function with a broken power-law.

The effect of flattening of the mass function is less pronounced further away from the cluster centre. This is illustrated in Figure 3.3, where we present the evolution of $x_{m > m_p}$ for the 24k simulations with $W_0 = 5$ and for $r = 0$ to r_{core} (top curve), for $r = r_{\text{core}}$ to $2r_{\text{core}}$ and for $r = 2r_{\text{core}}$ to

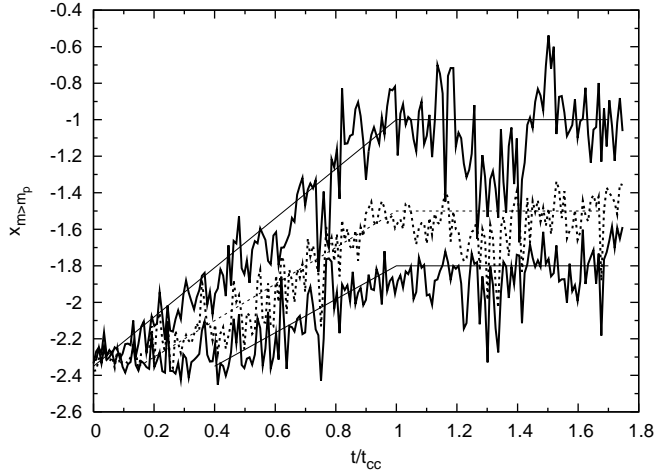


Figure 3.3: The evolution of $x_{m>m_p}$ for various radial bins in the 24k simulation with a $W_0 = 5$ King model. The time is given in units of core collapse time t_{cc} . The radial bins are $0 < r/r_{core} < 1$ (upper solid curve), $1 < r/r_{core} < 2$ (dotted curve), and $2 < r/r_{core} < 3$ (lower solid curve). To guide the eye, we plotted straight lines through the simulation data.

$3r_{\text{core}}$ (bottom curve). The values of m_p , $x_{m<m_p}$ and $x_{m>m_p}$ are obtained by a three-point least squares fit to the mass function in a predetermined annulus of the simulated data. Note that we relaxed the fitting procedure in the sense that the mass function is not required to be continuous. The point of stalling of the evolution of the mass function can be identified by the moment of core collapse, regardless of the initial concentration or the number of stars in the simulation. Therefore, we normalize the time axis in Figure 3.3 to that instant.

3.2.3 Post-collapse mass function

After the formation of a hard binary, the mass function achieves a quasi steady state. The slope of the high-mass end of the mass function varies throughout the cluster. In Figure 3.4 we show how the mass function for stars with $m > m_p$ after the moment of core collapse is a function of the distance to the cluster centre, being flatter closer in and resembling the initial mass function further out. Overplotted are the observed values of the mass function exponent (see Tab. 3.1, see § 3.3). The results of our simulations without a tidal field are statistically identical to those with a tidal field. The simulations with a minimum mass to the initial mass function of $m_{\min} = 0.1 M_\odot$ is plotted as the thin dashed curve in Fig. 3.4. It may be noted that the results of simulations with $0.1 M_\odot$ as the lower limit of the mass function are not consistent with the observed values of $x_{m>m_p}$ and m_p .

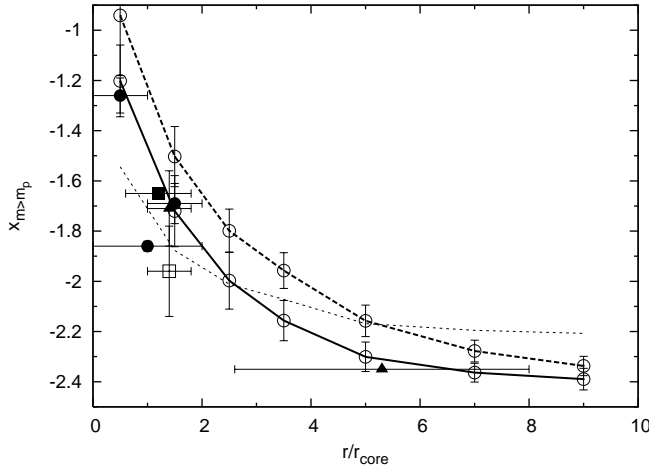


Figure 3.4: The value of $x_{m>m_p}$ as a function of distance from the cluster centre after core collapse. The solid curve gives the average value of $x_{m>m_p}$ over the various simulations with 24k stars for $W_0 = 3, 4, \dots$ up to $W_0 = 12$, the thick dashed line gives the data for the simulations with $N = 12k$. The squares, bullets and triangles with error bars give the observed values taken from Figer et al. (1999), Stolte et al. (2005) and Kim et al. (2006), respectively (see Tab. 3.1). The thin dashed line gives the value of $x_{m>m_p}$ for simulations with 24k particles with $W_0 = 9$ and a lower limit to the initial mass function of $0.1 M_\odot$.

In Figure 3.5, we show the value of m_p as a function of distance from the cluster centre for various simulations, past the moment of core collapse. It turns out that more concentrated initial models tend to result in a slightly smaller value of m_p whereas simulations with a smaller number of stars give rise to a higher value of m_p . The behaviour of $x_{m>m_p}$ is rather insensitive to the initial concentration of the cluster.

3.3 Mass function of the Arches cluster

At a projected distance of about 25 pc from Sgr A*, the Arches cluster ($\alpha = 17^h45^m50^s$, $\delta = -27^\circ49'28''$ in J2000), discovered by Cotera et al. (1992, 1996), is peculiar. The total cluster mass is about $2 \cdot 10^4 M_\odot$. The core radius of the cluster (defined as the radial distance from the cluster centre where the luminosity profile drops by a factor two) is $r_{\text{core}} = 5''.0$ (Stolte et al., 2005), and corresponds to about 0.2 pc if we assume that the distance to the Galactic centre is 8 kpc. The age of the cluster is 2 ± 1 Myr (Figer et al., 1999).

Recently, Kim et al. (2006) observed the Arches cluster using Keck/NIRC2 laser guide star adaptive optics. Their observations covered the inner parts of the cluster and some control fields at a distance of about 2.4 pc (60'') from

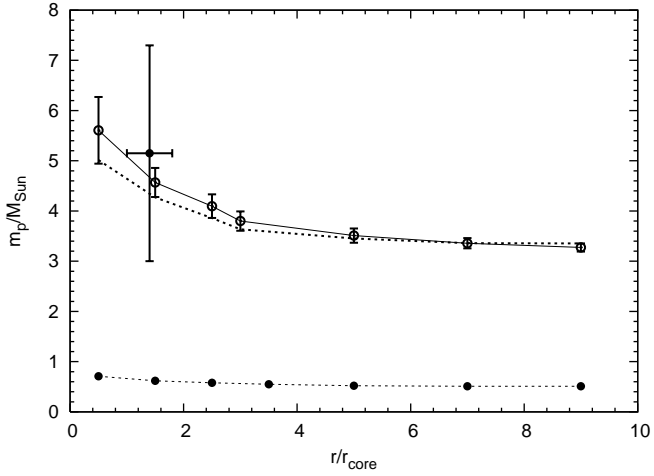


Figure 3.5: The value of m_p after the point of core collapse, as a function of distance to the cluster centre for various of simulations. The open circles connected with the thin solid line give the results for the simulations with 24k stars and with $W_0 = 5$ averaged between the moment of core collapse and twice the core collapse time. The error bars indicate the variation of the value of m_p over this time period. More concentrated initial models tend to have a slightly lower value of m_p , which we illustrate by plotting the $W_0 = 9$ simulation as the thick dotted line. The thin dashed line at the bottom gives the value of m_p for simulations with 24k particles with $W_0 = 9$ and a lower limit to the initial mass function of $0.1 M_\odot$.

the cluster centre. They subsequently constructed the luminosity and mass functions down to about $1.3 M_\odot$, in an annulus of 5" (about $1.0 r_{\text{core}}$) to 9" (about $1.8 r_{\text{core}}$) from the cluster centre. In Table 3.1 we give the various measurements of the mass function and the distance from the cluster centre in terms of the observed core radius.

The data show that the slope in the mass function for stars more massive than $\sim 5 M_\odot$ flattens towards the cluster centre (see fig. 3.4). For lower mass stars, as well as for further out than $\sim 4 r_{\text{core}}$ it is closer to the Salpeter mass function. The observed mass function in the Arches is not a simple power-law (Stolte et al., 2005; Kim et al., 2006). We argue that in the inner parts of the cluster, $r \lesssim 4r_{\text{core}}$, the mass function is best described by two power laws with the break around $m_p = 5-6 M_\odot$. The mass function below this break (m_p) resembles the initial mass function ($x_{m < m_p} \equiv x_{\text{IMF}}$), and above m_p it becomes flatter ($x_{m > m_p} > x_{\text{IMF}}$). Further out than $r \simeq 4 r_{\text{core}}$ the break disappears and the mass function becomes gradually better represented with the initial mass function.

r_{\min} (r_{core})	r_{\max} (r_{core})	m_{\min} (M_{\odot})	m_{\max} (M_{\odot})	ref	x
0	1	12	60	1	-1.26 ± 0.07
1	2	6	16	1	-1.69 ± 0.08
1	2	16	60	1	-2.21 ± 0.09
0	2	6	60	1	-1.86 ± 0.02
1	1.8	6.3	50	2	-1.71 ± 0.15
1	1.8	1.3	50	2	-1.91 ± 0.08
0.6	1.8	6.3	125	3	~ -1.65
4	8	2.8	32	3	$\mathcal{O}(-2.35)$

Table 3.1: Parameters for the observed mass function of the Arches cluster. The first two columns give the range over which the mass function is measured, in units of the cluster’s core radius ($r_{\text{core}} \simeq 0.20 \text{ pc}$). The third and fourth columns give the range in masses for which the exponent of the mass function (last column) is fitted. Column 5 gives the reference for the mass function exponents 1: Stolte et al. (2005), 2: Kim et al. (2006), 3: Figer et al. (1999), and the last column the measured value of x between m_{\min} and m_{\max} .

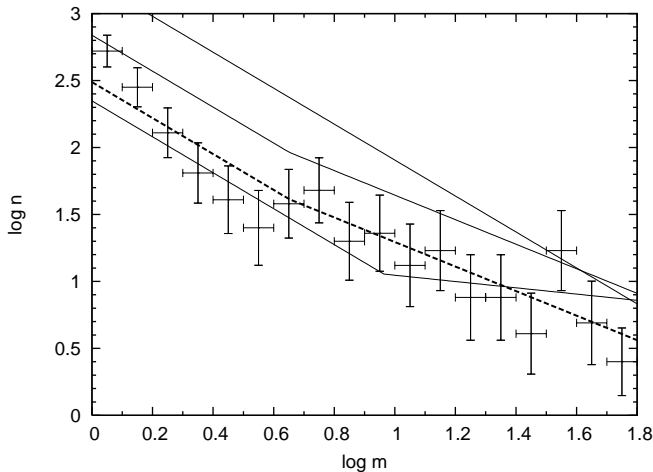


Figure 3.6: The present day mass function of the Arches star cluster between $1 r_{\text{core}}$ and $1.8 r_{\text{core}}$. The error bars are taken directly from Fig. 5 of Kim et al. (2006). The three thin lines are from Fig. 3.2 at zero age (top line), at $t \simeq 0.61t_{\text{cc}}$ (middle line) and at $t \simeq 1.05t_{\text{cc}}$ (bottom line). The thick dashed line is identical to the thin $t \simeq 0.61t_{\text{cc}}$ but then renormalized with -0.35 dex. This line produces a satisfactory fit to the observed mass function.

3.4 Discussion and conclusions

We performed detailed simulations of the evolution of young and dense star clusters using direct N -body simulations, in order to constrain the observed

mass function within about one parsec from the centre of the Arches cluster. The initial conditions of our simulations range over the full spectrum of King model density profiles.

The mass function in the central region of the Arches cluster is peculiar as it appears to be split in two power-laws, one for the stars less massive than $5\text{--}6 M_{\odot}$ and a much shallower slope for the more massive stars. The two power-laws fit the observed data between $5''$ and $9''$ is marginally better ($\chi^2 \simeq 0.5$) than a single power-law ($\chi^2 \simeq 0.93$).

The simulations we perform to mimic the Arches cluster are able to reproduce this observed broken power-law mass function at the observed projected distance from the cluster centre ($r = 0\text{--}4 r_{\text{core}}$). The best comparison between observations and simulations is obtained if the cluster is about half way core collapse ($t = 0.4\text{--}0.6 t_{\text{cc}}$).

Our simulations, however, are performed without stellar evolution and without including the effects of an external tidal potential. As a result, they are scale-free, and no specific choices for the scalings to mass, size and therefore to time are obliged. However, the scale-free aspect of our simulations hinders the direct comparison to some extent as the size scale (in parsec) and time scale (in Myr) are important for an unbiased comparison with the observed Arches cluster.

In the comparison with the observations we adopt the same definition of the core radius by projecting the cluster and assigning luminosities of all stars in our simulations using zero-age main-sequence luminosities². We ignore here the fact that very massive stars may become brighter in the 2 ± 1 Myr lifetime of the cluster, but this only affects the most massive stars, whereas the measurements are dominated by stars in the mid-range of masses.

The Arches cluster does not show any evidence for primordial mass segregation as our simulations (which were initialized without primordial mass segregation) are able to satisfactorily reproduce the observed mass function over the entire range of observed masses and distances from the cluster centre. Note also that the presence of primordial gas which failed to form stars does not seem to have affected the early cluster evolution, as the observed cluster structure at an age of 2 ± 1 Myr is satisfactorily explained with the simulations, which do not include gas dynamics. The initial mass function of the Arches cluster is then consistent with a Salpeter slope between $1 M_{\odot}$ and $100 M_{\odot}$ without the need for a radial dependence. There seems to be no need for a large population of stars less massive than $\sim 1 M_{\odot}$.

In Fig. 3.4 we show the evolution of $x_{m > m_p}$ for the annuli and distances

²For comparison, we adopt the observers' definition of core radius: the point where the surface brightness drops to half its central value. This is similar to but different from definitions used in theoretical works of (Spitzer, 1987, eq. 1-34) and (Aarseth, 2003, eq. 15-4). In starlab we adopt the method as discussed by Heggie et al. (2006). The latter definition of the core radius systematically is about twice the observers' definition.

from the cluster centre reported from our compilation from the literature in Tab. 3.1. The best match between the simulations and the observations is acquired for simulations between $t = 0.4t_{\text{cc}}$ and $0.6t_{\text{cc}}$, i.e: we predict that the cluster is about half way towards core collapse. We therefore conclude that the Arches cluster has not yet experienced core collapse but is currently in a pre collapse stage.

In Tab. 3.1 we have quantified the slope to the low mass end of the mass function in 5" to 9" annulus of the Arches cluster as consistent with Salpeter, whereas the naive measurement in Fig. 5 of Kim et al. (2006) would results in $x_{m < m_p} = -3.67 \pm 0.14$ (with $m_p = 5 M_\odot$), which is unusually steep. If this slope would represent the intrinsic Arches initial mass function and we adopt a minimum mass of $1 M_\odot$ the observed ~ 2600 stars more massive than $\sim 5 M_\odot$ in the Arches cluster would result in a total number of more than 2×10^5 stars, which is unrealistically high. From an observational point of view there are good arguments that the low mass end of the mass function is over-estimated, as it is plagued by selection effects. One of these effects is the artificial correction of missing stars in a crowded field and the selection of the three control fields to compensate for the background population. In the Keck observations these control fields are within about 2.4 pc from the cluster centre, which corresponds to $\sim 12 r_{\text{core}}$. For a King model with $W_0 \gtrsim 5.2$ the control fields would then be located near the cluster tidal radius. And since the cluster is about half way towards core collapse it is conceivable that the density profile is described with a King model with $W_0 \gtrsim 7$, in which case the control field are part of the cluster halo.

Due to mass segregation the cluster outskirts will be depleted of high mass stars and low mass stars will be overrepresented (the opposite effect as we discussed for the core population). Correcting the mass function in the cluster core with a population taken from near the cluster halo will therefore result in an enormous over correction towards the low mass stars, and consequentially result in a steepening of the 'corrected' mass function.

One of the control fields (field B of Kim et al, 2006) is taken near the location where one expects the tidal tail of the cluster in the potential of the Galaxy to pass though. The tidal tail is, since it consists of the halo population, also likely to be dominated by low mass stars.

Each of the effects discussed tend to steepen the lower-mass end of the mass function, though it is not trivial to quantize the effect without a much more detailed study. We however, argue that the initial mass function of the Arches cluster was probably consistent with Salpeter over the observed mass range. The observed break in the mass function around $5-6 M_\odot$ and the consequential flattening of the mass function for higher masses is then the result of the dynamical evolution of the cluster.

The initial model which is most comparable to the observed Arches cluster has a Salpeter initial mass function between $1 M_\odot$ and $100 M_\odot$ and with a reasonably concentrated initial density profile ($W_0 \gtrsim 4$ and $W_0 \lesssim 8$).

The break in the mass function in the inner parts of the cluster (for $r \lesssim 4r_{\text{core}}$) appears at $m_p \simeq 2\langle m \rangle$, which for our simulations is at about $5 M_\odot$. The break in the observed mass function in the Arches cluster appears around the same mass of $m_p \simeq 5\text{--}6 M_\odot$. We performed additional simulations with $W_0 = 9$ using a Salpeter mass function down to $0.1 M_\odot$, and in this case the break in the core mass function also developed around $m_p \simeq 2\langle m \rangle$, which for the adopted mass function is about $1.0 M_\odot$ (Figure 3.5). Based on these findings we argue that the initial mass function in the Arches cluster has a lower limit of about $1.0 M_\odot$, as in our simulations that reproduce the observations best.

We predict that other clusters with similar parameters as the Arches cluster, like Westerlund 1 (Piatti et al., 1998), NGC 3603 (Moffat et al., 2004), R 136 (Meaburn et al., 1982) and Quintuplet (Cotera et al., 1992) will show similar characteristics as Arches. The mass functions in their cores will also be rather flat for stars more massive than $5\text{--}6 M_\odot$. And the mass functions further away from the cluster centre will gradually be more like the initial mass function.

Acknowledgments

We are grateful to Peter Anders, Mark Gieles, Alessia Gualandris, Douglas Heggie and Henny Lamers for many discussions. This work was supported by NWO (grants #635.000.303 and #643.200.503), NOVA, the LKBF, the ISSI in Bern, Switzerland and the Taiwanese government (grants NSC095-2917-I-008-006 and NSC95-2112-M-008-006). MAG is supported by a Marie Curie Intra-European Fellowship under the sixth framework programme. The calculations for this work were done on the MoDeStA computer in Amsterdam, which is hosted by the SARA supercomputer centre.

Chapter 4

Dynamics of the first collision in young star clusters

Based on:

E. Gaburov, A. Gualandris and S. Portegies Zwart

Monthly Notices of the Royal Astronomical Society, 384, 376, 2008

ABSTRACT

We study the circumstances under which the first collision occurs in young and dense star clusters. The initial conditions for our direct N -body simulations are chosen such that the clusters experience core collapse within a few million years, before the most massive stars have left the main-sequence. It turns out that the first collision is typically driven by the most massive stars in the cluster. Upon arrival in the cluster core, by dynamical friction, massive stars tend to form binaries. The enhanced cross section of the binary compared to a single star causes other stars to engage the binary. A collision between one of the binary components and the incoming third star is then mediated by the encounters between the binary and other cluster members. Due to the geometry of the binary-single star engagement the relative velocity at the moment of impact is substantially different than in a two-body encounter. This may have profound consequences for the further evolution of the collision product.

4.1 Introduction

In recent years, it became clear that stellar collisions are common events in young dense star clusters, and that such events are natural ways to form stellar exotica. In extreme cases, it is even possible that a large number of stars merge to form a very massive object. This object can potentially be a progenitor of an intermediate mass black hole.

Portegies Zwart et al. (1999) carried out the first N -body simulations of runaway stellar collisions. In these simulations, a very massive object forms in a young dense star cluster in just a few million years. It was found that the collision rate is roughly an order of magnitude greater than one would naively expect from collision cross-section arguments. The cause of the discrepancy is mass segregation, which enhances the central region with massive stars. Once in the core, these stars dominate the collision rate because of their large masses and radii. Since a collision occurs preferentially between two massive stars, the collision product becomes one of the most massive objects in the central region. If conditions are right, the product can experience multiple collisions, each time increasing its mass. This process can lead to the formation of a very massive object. The evolution of very massive stars and of collision products is not yet well understood, but one may speculate that these massive objects evolve into intermediate mass black holes.

Numerical simulations carried out by Portegies Zwart et al. (2004) show that the onset of a runaway merger depends on both the dynamical friction timescale and the central concentration of the star cluster. In particular, a necessary condition for the runaway collision to proceed is the dynamical friction timescale to be smaller than the lifetime of massive stars, which is about a few million years. If this condition is not satisfied, the mass loss due to supernovae causes the cluster to expand, and this prevents the cluster from developing the high densities required for subsequent collisions.

In their work, Gürkan et al. (2004) carried out systematic studies of mass segregation and core collapse in dense star clusters. They found that moderately concentrated star clusters with a realistic initial mass function can reach the runaway phase before massive stars produce supernovae. The runaway phase was also studied by Freitag et al. (2006), who found that the mass function of colliding stars is bimodal. The first peak lies in the lower limit of the initial mass function, $0.1 - 1M_{\odot}$, whereas the second peak is close to the high-mass end of the initial mass function, $40-120M_{\odot}$. They also found that collisions occur every few ten thousand years, which is roughly the time required for a collision product to reach the main-sequence.

Stellar collisions also play an important role in the formation of stellar exotica in young star clusters, such as blue stragglers. If cluster properties are such that the runaway phase is not possible, stellar collisions might still occur in the cluster producing massive bright stars. Such stars might easily

be misclassified during observations. A possible example of these stars is provided by the Pistol star in the Quintuplet cluster (Figer et al., 1998a), which is thought to have an initial mass in excess of two hundred solar masses. The lifetime of such a star is roughly three million years. However, the cluster population is about six million years old, significantly older than the Pistol star. It is therefore possible that the Pistol star is in fact an ejected collision product instead of a primordial very massive star.

In this work, we study the dynamics of the first stellar collision in young star clusters. The aim is to find a set of appropriate initial conditions for subsequent hydrodynamic simulations of collision products. In particular, we focus on the conditions under which the first collision takes place in a cluster, like the time and place of the first collision, the number of stars and binaries involved, the masses of the participating stars, the orbital parameters of the binaries, the typical impact parameter and relative velocity in the collision. The knowledge of the dynamical properties of stellar collisions will allow us to perform hydrodynamic simulations of mergers. The study of the evolution of merger products determines the observational properties of these objects, thus providing valuable information for their identification. Once the main characteristics of the evolution of collision remnants will be understood, we will proceed with the study of the dynamics of repeated stellar collisions in star clusters, with the aim to answer the question of whether a runaway process can result in the formation of a very massive object, which in turn may evolve into an intermediate mass black hole.

This chapter is organised as follows. In Sect. 4.2 we present initial conditions for our simulations. The detailed studies and the geometry of the first collision is presented in Sect. 4.3 and Sect. 4.4. A discussion of results is presented in Sect. 4.5.

4.2 Setup and initial conditions

In order to study the onset of the first collision, we focus on young star clusters with different initial virial radii (R_{vir}) which we vary over more than one order of magnitude, while maintaining the total mass of the cluster constant. The choice of keeping R_{vir} as a free parameter is motivated by the aim to study the dependence of the moment of the first collision on the cluster size. Clusters with similar initial conditions but different sizes exhibit homologous evolution as far as non-dynamical processes, like stellar and binary evolution, are not of significant importance. However, in the case of stellar collisions individual stellar radii play a crucial role. In this case, the evolution of the star cluster in principle is not homologous; in other words, the two stars which collide in one case will not necessarily collide if the cluster size is changed. The reason is that by scaling the cluster in size, the stellar radii relative to the cluster size also changes. By varying R_{vir} we

Model	R_{vir} [pc]	N_{run}	r_{core} [pc]	ρ_{core} [M_{\odot}/pc^3]	t_{cross} [kyr]	t_{rlx} [Myr]
W9R05	0.05	100	$3.2 \cdot 10^{-3}$	$5.5 \cdot 10^9$	1.5	0.47
W9R10	0.10	100	$6.4 \cdot 10^{-3}$	$6.8 \cdot 10^8$	4.3	1.4
W9R25	0.23	100	0.015	$5.6 \cdot 10^7$	15	4.7
W9R50	0.50	99	0.032	$5.5 \cdot 10^6$	48	15
W9R75	0.75	110	0.048	$1.6 \cdot 10^6$	88	28

Table 4.1: Parameters of the five sets of simulations. In each case the total mass of the cluster is $M \simeq 1.2 \times 10^4 M_{\odot}$ and the total number of stars is 24576. Runs differ only in the choice of the half-mass radius. In the first three columns we report the name of the set of simulations, the virial radius (in parsec) and the number of simulations performed with these parameters. In the subsequent columns we give the initial core radius (in parsec), the initial core density (in solar masses per cubic parsec), the half-mass crossing time (in units of 1000 years) and the relaxation time (in Myr).

will be able to determine its influence on the collisions in star clusters.

All our calculations are performed using the `kira` integrator from the `starlab` gravitational N -body environment (Portegies Zwart et al. (2001))¹. Stellar evolution in the simulations is included via the `SeBa` package Portegies Zwart & Verbunt (1996). Binaries, though initially not present, form dynamically in the course of the simulations and are evolved using `SeBa`. All N -body simulations were carried out on the MoDeStA² cluster of GRAPE-6 (Makino et al., 2003, 1997) in Amsterdam.

We present the initial conditions for the different sets of simulations in Tab. 4.1. Each simulation is carried out with $N=24576$ single stars distributed in a King (1966) model with a scaled central potential $W_0 = 9$ (Binney & Tremaine, 1987). We did not include primordial binaries because we aim to study large parameter space in this work.

Such a choice of W_0 is motivated by our interest in studying young star clusters such as R136, MGG11 and Arches (Massey & Hunter, 1998; Figer et al., 2002; McCrady et al., 2005), and young star clusters are thought to be born with high concentration (Merritt et al., 2004b). In addition, high concentration is a necessary condition for clusters which can experience runaway stellar mergers (Portegies Zwart et al., 2004). As we are interested in the internal dynamics, the effect of the tidal fields is expected to be negligible (Portegies Zwart et al., 2007b); therefore, our simulations are carried out without tidal fields. After generating stellar positions and velocities, we assign masses to each of the stars from an initial mass function (Kroupa et al. (1993); Kroupa (2001)) between $0.1 M_{\odot}$ and $100 M_{\odot}$, which we refer to as IMF. We subsequently scale the velocities of all stars to bring the cluster into virial equilibrium. Such initial conditions produce star clusters with a

¹<http://www.manybody.org/starlab>

²<http://modesta.science.uva.nl>

total mass of roughly $10^4 M_\odot$, which approximates well the Arches cluster (Figer et al., 1999, 2002).

For each set of initial conditions with $W_0 = 9$, we generate about a hundred realisations, each of which we run until the first collision occurs. We identify a collision in our simulations when two stars pass each other within a distance smaller than the sum of their radii; tidal captures are ignored. The binary evolution package allows for semi-detached and contact binaries to transfer mass. In our analysis, we discriminate between two types of collisions: those that result from unstable mass transfer in a close binary system and those that result from a dynamical interaction. The latter case we identify as a collision, whereas the former case is referred to as coalescence. In this work we focus on physical collisions between stars.

Our code employs “standard N-body units”³ (Heggie & Mathieu (1986)), according to which the gravitational constant, the total mass and the radius of the system are taken to be unity. The resulting unit of time is the N -body time-unit and is related to the physical crossing time of the system through the relation $T_{\text{cross}} = 2\sqrt{2} t_{\text{Nb}}$.

4.3 The circumstances of the first collision

In order to develop a better understanding of stellar collisions and of the further evolution of the collision product, it is important to know the conditions under which a collision takes place, such as the mass, structure and composition of the participating stars, and the geometry under which the collision occurs.

4.3.1 The location of the first collision

Since the stellar density is highest in the cluster core, we expect that majority of collisions to take place in the central region. In the top panel of Fig. 4.1, we show the distribution of the number of collisions as a function of the distance to the cluster centre. All simulations presented in Tab. 4.1 are included in the sample. Out of a total of 282 collision in 509 simulations, only 33 occur outside the instantaneous core of the cluster.

Though a small fraction (12 %), it is interesting that a sizeable number of collisions occurs outside the core of a cluster. This can be naturally explained as follows. In a cluster with a density profile $\rho(r)$, the expected number of collisions in a spherical shell located at radius r is $N \propto r^2 \rho(r)^2$, and therefore one may expect a small, but finite, number of collisions to occur just outside the core. To test this, we fitted this expression to the number of collisions. As a density profile, we used a variety of King models with different values of W_0 . We found that King models with $W_0 \gtrsim 9$ fit

³http://en.wikipedia.org/wiki/Natural_units#N-body_units.

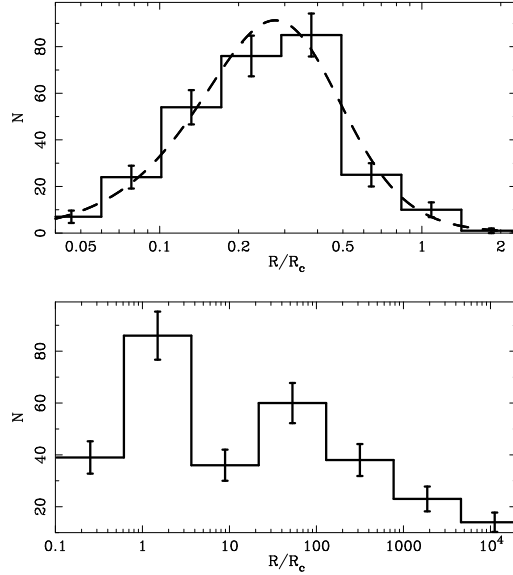


Figure 4.1: Histogram of the number of collisions in all simulations as a function of the distance to the cluster centre in units of the instantaneous core radius. In the upper panel, the dashed line displays the fitted model of the number of collision. In the lower panel we present the distribution of coalescence as a function of distance to the centre of a cluster.

well ($\chi^2 \approx 1$) since their density profiles in the close neighbourhood of the core are essentially the same.

In the lower panel we present the distribution of number of coalescence as a function of the distance to the cluster centre. We see that the coalescence can occur quite far from the core of the cluster; such coalescence are ejected binary stars in which the massive companion leaves the main-sequence. The number of coalescence events far away from the core decreases as a function of distance to the cluster centre.

4.3.2 The time of the first collision

In Fig. 4.2, we show the time distributions for the formation of the first hard binary and for the first collision. The first collision occurs preferentially after the formation of the first hard binary, but the distribution is broad and extends all the way to $\sim 200N$ -body time units. We notice that the coalescence dominate at $t \gtrsim 20$ N -body units, whereas collisions are dominant earlier.

The evolution of the mass function in the cluster centre is mainly driven by dynamical friction, which preferentially brings massive stars to the core. As a result, the mass function in the core becomes flatter with time, and after core collapse the mass function stops evolving except for the effects of

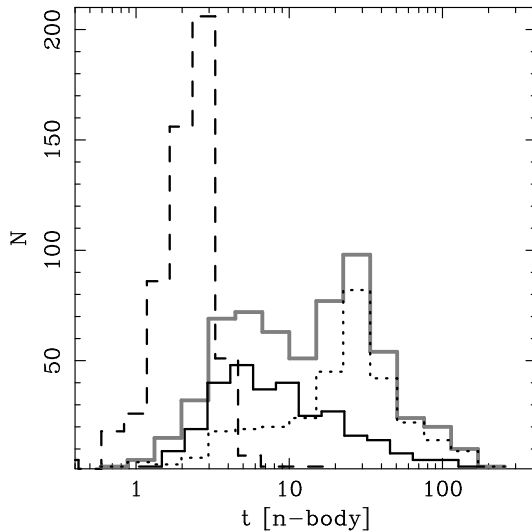


Figure 4.2: Histogram of the number of first $|E| > 100 kT$ binaries (dashed line), first collisions (solid line) or first coalescence (dotted line) as a function of time (expressed in N -body units). The total number of mergers (collisions + coalescence) in a time-bin is shown with a thick gray solid line.

stellar evolution, such as decrease of the number of massive stars in a star cluster (Portegies Zwart et al., 2007b).

In Fig. 4.3 we present mass functions in the core at the moment of the first collision averaged over all simulations in which a collision happens. The mass functions for different models are consistent with a single distribution better than at a 25% level. However, for models W9R50 and W9R75 the consistency is less than at 5% level, which is due to the effects of stellar evolution. As the ratio of a stellar evolution timescale to a dynamical timescale is inversely proportional size of a star cluster, the effects of stellar evolution become increasingly important as the size of the cluster increases. While stellar evolution does not have a notable influence on models W9R05, W9R10 and W9R25, it clearly leaves an imprint in models W9R50 and W9R75 (see also Appendix 4.A).

The mass function in the core after the first collision can be approximated by the following expression:

$$\mathcal{N}_c(m) \propto \begin{cases} \mathcal{N}_{\text{IMF}}(m), & \text{if } m < m_1 = 2\langle m_{\text{IMF}} \rangle, \\ m\mathcal{N}_{\text{IMF}}(m), & \text{otherwise.} \end{cases} \quad (4.1)$$

Here $\mathcal{N}_{\text{IMF}}(m)$ is the initial mass function and $\langle m_{\text{IMF}} \rangle$ is the average mass of the initial mass function. This expression is presented as the thick solid line in Fig. 4.3. Equation 4.1 implies that for stars more massive than $\sim 2\langle m_{\text{IMF}} \rangle$ the slope of the mass function flattens. This is not unexpected since the dynamical friction time-scale is inversely proportional to m . We

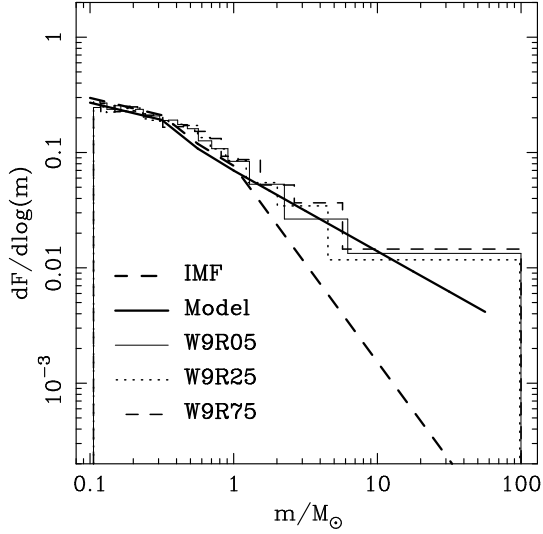


Figure 4.3: Mass function in the core at the moment of the first collision averaged over all runs for each model. The thick dashed line represents the IMF whereas the thick solid line represents Eq. 4.1 which satisfactorily represents the simulated mass function in the core.

conclude that dynamical friction is a crucial ingredient in understanding the first collision.

In Fig. 4.4 we compare the time of the first collision, t_{coll} , with the time-scale on which a star with mass m sinks to the cluster centre from its initial orbit, t_{decay} .

We compute t_{decay} for the most massive star that participates in the first collision by integrating its equations of motion from the initial orbit until the star decays to the cluster centre. We include the effect of dynamical friction using $\log(\Lambda) = \max(0, \log(0.4M_{\text{cl}}(r)/m))$, where $M_{\text{cl}}(r)$ is the cluster mass enclosed within a sphere of radius r (Binney & Tremaine, 1987). As for the background potential, we adopt a King $W_0 = 9$ density profile which represents our initial simulation model.

The correlation between t_{coll} , which is taken directly from the simulations, and t_{decay} , which is calculated as described above, is presented in Fig. 4.4. In the left panel the results are given in units of the core collapse time as measured in the simulation under consideration, whereas in the right panel time is given in physical units.

In the left panel of Fig. 4.4 we identify three different regimes. The majority of collisions are distributed along $t_{\text{coll}} = t_{\text{decay}}$ (area 1 in Fig. 4.4). This indicates, as we suggested earlier, that dynamical friction is dominant in determining the moment of the first collision. A collision occurs quickly upon the arrival of the star in the core.

The dispersion along t_{decay} in area 1 of Fig. 4.4 is in part a consequence

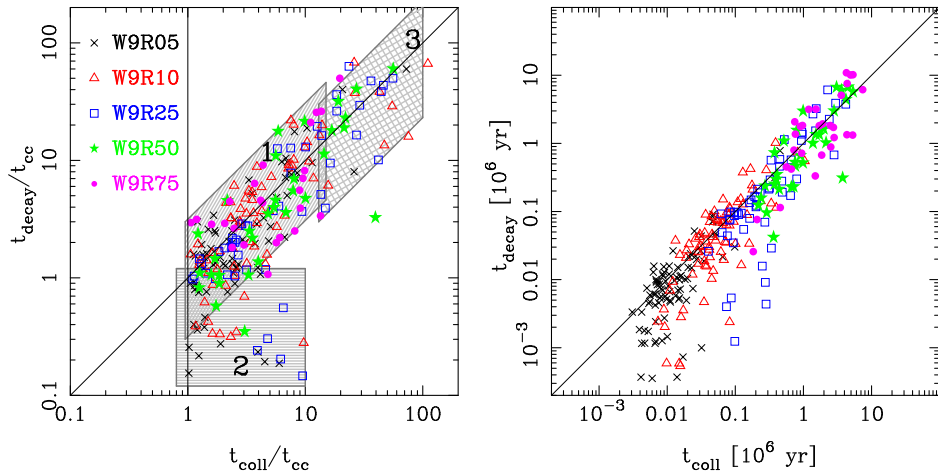


Figure 4.4: Correlation between t_{coll} and t_{decay} . In the left panel t_{coll} and t_{decay} are given in N -body units while in the right panel they are in physical units. The results from different models are indicated with different symbols and colours. The diagonal in both panels gives the line for which $t_{\text{coll}} = t_{\text{decay}}$. The gray shaded areas in the left panel, numbered 1, 2 and 3, indicate three different regimes, as described in the text.

of our assumption that the background potential is static throughout our calculations of t_{decay} . The density profile of the clusters, however, is calculated self consistently in our N -body simulations, and it changes with time. In addition, even when the star arrives in the core, it still takes some time before it engages in a collision. The latter effect is visible in area 2 of Fig. 4.4.

In area 2 of Fig. 4.4, we present the stars that experience a collision later than one would naively expect from their calculated decay time. These stars are born in or near the cluster centre but a collision is delayed up to the moment of core collapse. After that, the stars still have to participate in a strong encounter which leads to a collision. Thus, the moment of the collision is determined by t_{cc} and the time required to find a suitable collision candidate, and this may take up to about $10t_{\text{cc}}$.

It is somewhat surprising that there is a third region along the line $t_{\text{coll}} = t_{\text{decay}}$, which is illustrated in the area 3 of Fig. 4.4, and which extends all the way to $t_{\text{coll}} \simeq 100t_{\text{cc}}$. As a rule of thumb, it takes roughly 50 N -body units for a $50M_{\odot}$ star to decay from the half-mass radius to the core. From area 2, it can be seen that a star in the core may require up to $10t_{\text{cc}}$, which roughly corresponds to 30 N -body time units (see Fig. 4.2), to engage in a collision. Since we expect our simulations to host at least one $50M_{\odot}$ star which is initially located within the half-mass radius, it is rather unlikely to have collisions in our simulations after $t \simeq 15t_{\text{cc}}$; still, some collisions do

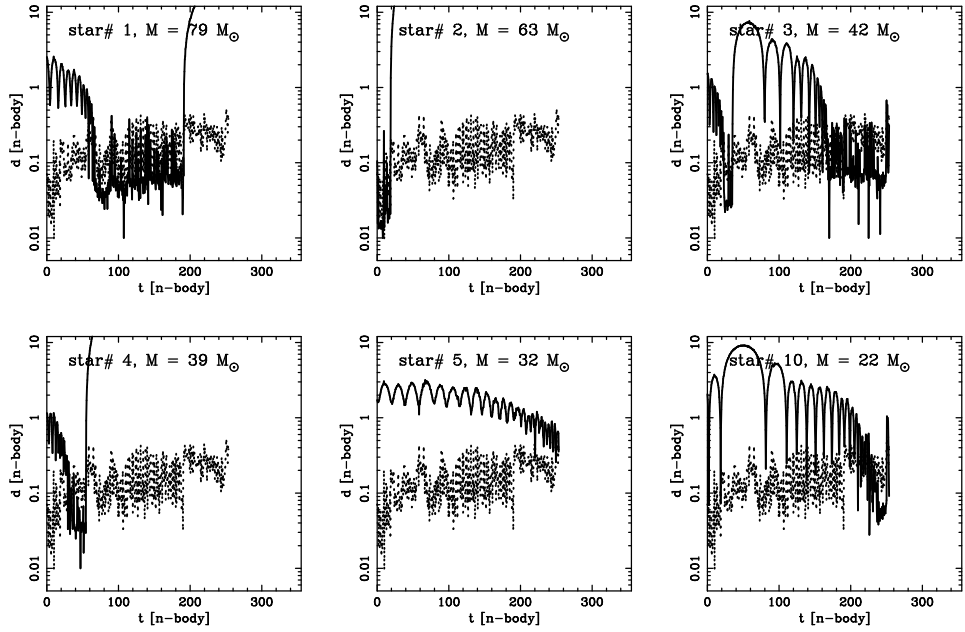


Figure 4.5: Distance to the cluster centre for six of the most massive stars in one of the simulations from model W9R05. The dotted curve in each panel gives the evolution of the core radius of the model (which is identical in each panel). The solid curve gives the evolution of the distance to the cluster centre for the star identified in the top left corner of the panel.

happen as late as $100 t_{\text{cc}}$.

These late collisions, which are illustrated in area 3 of Fig. 4.4, are attributed to massive stars that reach the core but instead of experiencing a collision are ejected from the cluster in a strong encounter with a binary. This effectively delays the moment of the first collision since the potential target star is removed from the cluster. If this happens, the first collision is postponed until the moment when another massive star reaches the cluster core and subsequently collides. In Appendix 4.B we show that such self-ejections are possible in clusters with mass

$$M_{\text{cl}} \gtrsim 2 \cdot 10^4 \left(\frac{m_{\star}}{50 M_{\odot}} \right)^3 \left(\frac{m_s}{10 M_{\odot}} \right)^{-2} M_{\odot}. \quad (4.2)$$

Here, m_{\star} is the mass of an ejected star, and m_s is the mass of the star triggering the ejection event.

The process described in the previous paragraph is illustrated in Fig. 4.5 where we present the evolution of the distance to the cluster centre for several of the most massive stars in one of the simulations of W9R05 (see Tab. 4.1). In addition, we plot the evolution of the core radius in each panel.

The most massive cluster member, star #1 of $79 M_{\odot}$, which is presented

in the top left panel of Fig. 4.5, sinks from about the half-mass radius to the cluster core in roughly $50 N$ -body time units ($\simeq 15 t_{\text{cc}}$ in this particular run). It becomes a binary member at $t \simeq 88.5$ and the binary increases its binding energy to $\sim 100 \text{ kT}$ at $t \simeq 165 N$ -body time units. Star #1 stays in the core until it is ejected at about $200 N$ -body time units, never to return again. Even though star #1 is the most massive star in the system, it is part of a binary system and it resides in the cluster centre for more than $100N$ -body time units, it does not participate in a collision but is ejected from the core.

The same process causes several of the other massive stars to be ejected, such as stars #2 and #4 in Fig. 4.5, whereas some of the other massive stars, such as stars #3 and #5, are not ejected. These repeated ejections of high-mass stars delay the collision until nearly $250 N$ -body time units, which roughly corresponds to $80 t_{\text{cc}}$. Eventually, it is $22 M_{\odot}$ star #10 which reaches the core and experiences a collision with a $4 M_{\odot}$ star.

4.3.3 Mass distributions

The binary which forms during core collapse is likely to be the candidate for a collision. However, this does not mean that the two stars in the binary coalesce, instead this enhances the probability for a collision with a third star.

In Tab. 4.2 we present the number of collisions that occurred in each of the models with respect to the choreography of the triple interaction. The notation is as follows: the two binary members are called M_p and M_s for the most massive (primary) and least massive (secondary) star respectively, while the third star is called the bullet and is indicated with M_b ; the two colliding stars are presented in braces while the entire triple interaction is in parenthesis.

The collisions in the densest star clusters (model W9R05 and W9R10) are dominated by collisions between the primary and the bullet star. The fraction of these collisions remains roughly constant compared to the total number of collisions. The shallowest clusters (model W9R50 and W9R75), on the other hand, are governed by binary evolution, which does not come as a surprise since stellar evolution plays an increasingly important role as the size of the cluster increases. In some cases, however, the primary is not participating in the collision, but instead it is the secondary star that collides with the bullet.

In the left panel of Fig. 4.6, we present the distribution of primary masses. These distributions are statistically indistinguishable for the three densest clusters (models W9R05, W9R10 and W9R25), whereas for the shallowest clusters (models W9R50 and W9R75) they deviate in that the mean mass for the primary stars decreases. This is the result of stellar evolution, which becomes gradually more important for shallower clusters. The mass

Model	$(\{M_p, M_b\}, M_c)$	$(\{M_s, M_b\}, M_p)$	$(\{M_p, M_s\}, M_b)$	N_c	N_m
W9R05	67	15	5	87	13
W9R10	59	11	9	79	21
W9R25	37	12	5	54	46
W9R50	16	12	5	33	66
W9R75	19	5	5	29	81

Table 4.2: The choreography of triple interactions leading to a collision in the different calculations. In the first column, we present the model name followed by the number of collisions in each of the configurations. These are: a collision between the primary and the bullet (column two), a collision between the secondary and the bullet (column three) and a collision between the primary and the secondary star (column four). The fifth column shows the total number of collisions that are outcomes of a dynamical interaction, whereas the last column shows the number of binary mergers which result from an unstable phase of mass transfer in a dynamically formed binary. The latter category is not further discussed in this work.

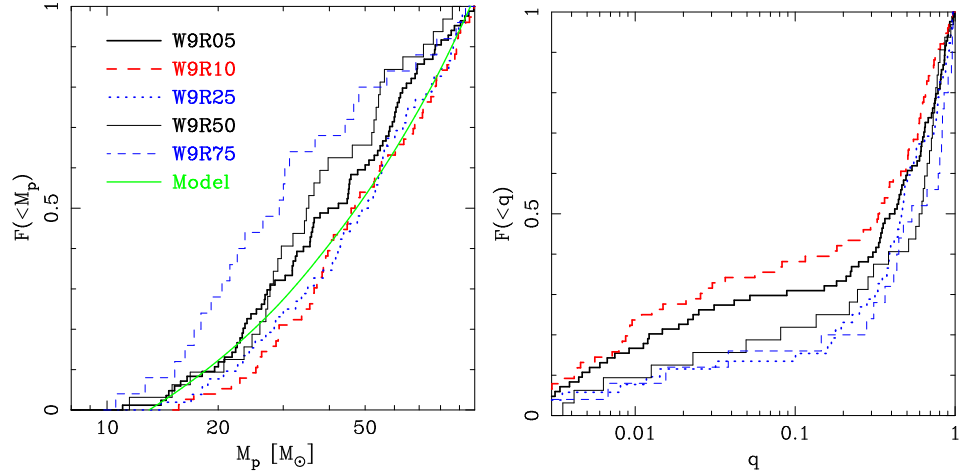


Figure 4.6: Distribution of primary masses (left) and mass ratios (right) for binaries participating in the collision. According to Kolmogorov-Smirnov test there is 15%, 28%, 90%, 5% and 0.2% chance for models W9R05, W9R10, W9R25, W9R50 and W9R75 respectively that the deviations in the distributions from the theoretical curve are random in nature. The green solid line is a cumulative mass function in the core (Appendix 4.A), but with the lower mass limit taken to be $15 M_\odot$.

functions of the primary in models W9R05, W9R10 and W9R25 are consistent with the mass function in the core at the moment of the first collision (Appendix 4.A), if only stars above $15 M_\odot$ are taken into account.

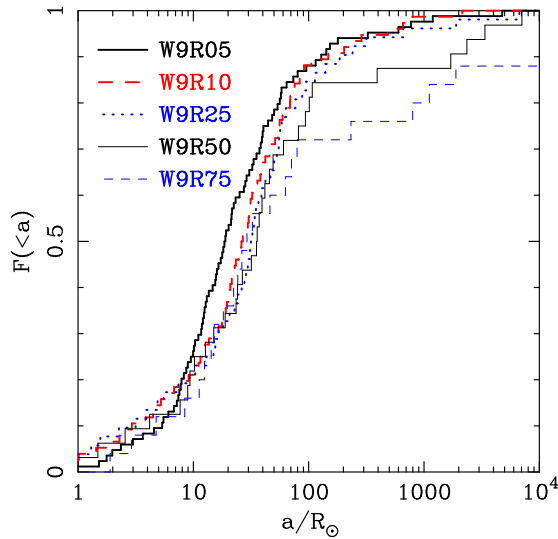


Figure 4.7: Distribution of semi-major axes for binaries undergoing a collision. Binaries with separation smaller than the sum of their stellar radii $a \lesssim 10 R_\odot$ are contact binaries which form in the course of the simulation.

In the right panel of Fig. 4.6, we present the distribution of the mass ratio of the secondary to the primary star. Here, we see that the mass ratio for shallower clusters is systematically higher than for denser clusters. This trend we explain by the fact that the binaries in shallower clusters experience more interactions before they participate in a collisions, allowing for exchanges of a more massive star into the binary. This is supported by Fig. 4.7 where we plot the distribution of orbital separations of the binaries that participate in a collision event. These distributions are statistically indistinguishable when displayed in physical units. This however implies that the binaries in the larger clusters are harder as their semi-major axis is smaller when measured in N -body units.

In Fig. 4.8 we present the distribution of the masses of bullet stars colliding with the primary. The mean mass of bullet stars increases with the size of the cluster. Together with the simulation data, we present the theoretical line which gives the results of a qualitative model for the mass of the bullet star. The low-mass end of this curve follows the mass function in the cluster core at the moment of the collision, whereas for the steeper high-mass part (above $\sim 2\langle m \rangle_{\text{core}}$), we weight the probability distribution with the gravitational focusing of the bullet:

$$\mathcal{N}_b(m_b) \propto \begin{cases} \mathcal{N}_c(m_b), & \text{if } m_b < 2\langle m \rangle_{\text{core}}, \\ m_b \mathcal{N}_c(m_b), & \text{otherwise.} \end{cases} \quad (4.3)$$

We make the distinction between the enhanced cross section (high-mass end) and the geometric cross section (low-mass tail), since we expect that

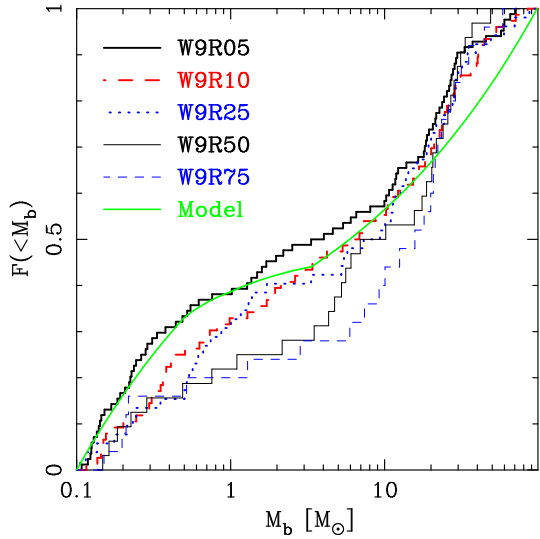


Figure 4.8: Mass function of single stars that collide with binaries. The solid line shows a cumulative distribution function computed from a bullet mass function presented in Eq. 4.3

for low-mass bullet stars the collision rate is dominated by the cross section of the encountering binary, rather than the bullet itself.

4.4 The collision geometry

In the previous sections, we demonstrated that all collisions in a cluster's centre occur between a binary component and a single star. This has far reaching consequences for the energetics and angular momentum of the collision. While in a two-body collision the outcome of the event depends only on the impact parameter and the relative velocity at large separation, in our simulations the situation is considerably more complicated as one of the encountering objects is always a binary member. In this case the relative velocity at the moment of the impact can be either significantly higher or lower than in the idealised two-body case. Therefore, the consequences for the evolution of the collision product may be profound.

Fig. 4.9 illustrates the two extreme cases that can occur when a bullet star collides with a star in a binary. In the left panel we show two colliding stars that are approaching each other at the moment of the first contact, whereas in the right panel we show two colliding stars that are moving in the same direction at the moment of impact, so that the binary companion is effectively receding from the bullet star.

The consequence for the impact velocity in terms of the escape speed of the merged object is illustrated in Fig. 4.10. Here, we see that about

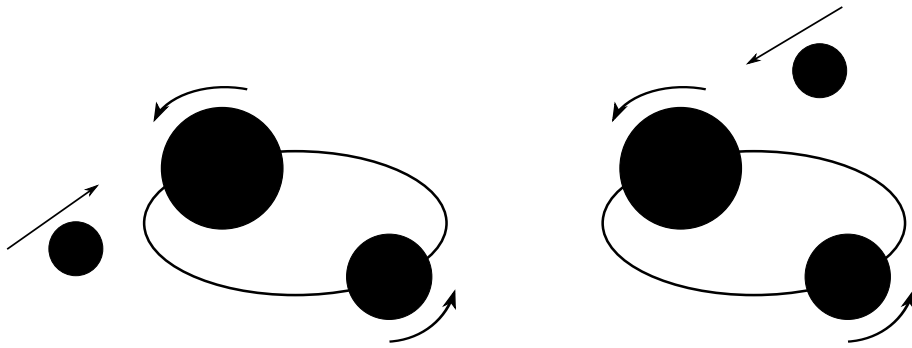


Figure 4.9: Schematic representation of the collision between a binary member and a single star. The left figure shows the case when the two colliding stars move towards each other. In this instance, the impact velocity can exceed the escape velocity from the two body systems formed by the colliding stars. The right figure shows the case when the two interacting stars move in the same direction. In this case, if a collision occurs, the impact velocity can be smaller than the escape velocity.

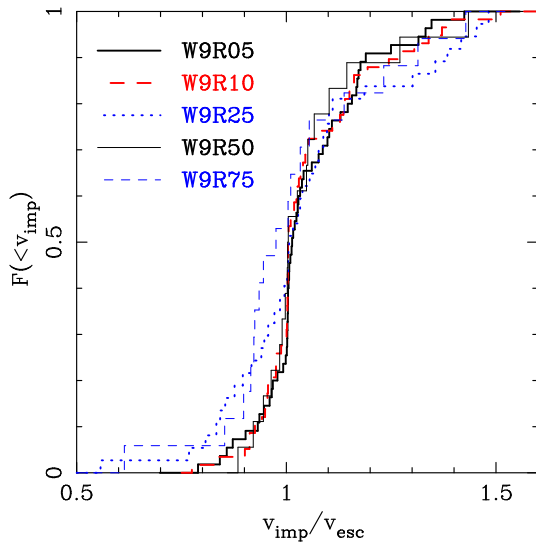


Figure 4.10: Cumulative distribution of impact velocities in units of the escape velocity of the two-body system formed by the colliding stars. The thick solid line corresponds to a W9R05 model, the thick dashed line to a W9R10, the thick dotted line to a W9R25, the thin solid line to a W9R50 and the thin dotted line to a W9R75 model.

half of the collisions occur with a velocity smaller than the one expected for a two-body encounter. In some extreme cases, however, the velocity at impact can be $\simeq 50\%$ higher than in the two-body case. The tail of

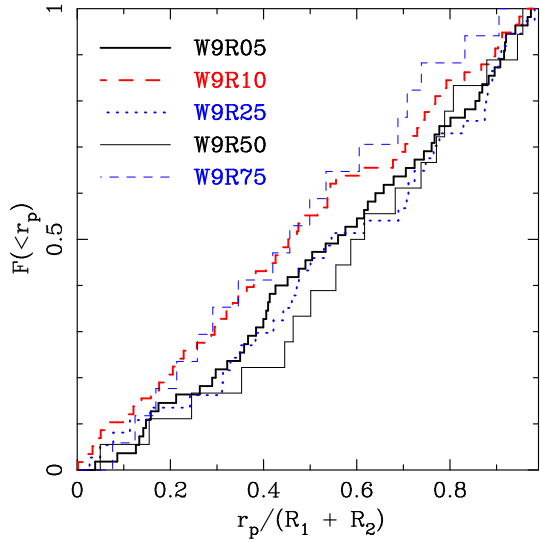


Figure 4.11: Cumulative distribution of pericentres. The pericentres are computed assuming that two stars approach each other on a hyperbolic trajectory such that their relative velocity at contact is equal to the one observed in the simulations.

lower impact velocities is completely absent in isolated two-body unbound encounters; this latter case is somewhat comparable to the merger of two binary components.

In Fig. 4.11, we present the distance between the two stellar centres at the moment of impact. For all models, the distribution of impact distance is flat and as a result the cumulative distribution is a straight diagonal line. This is a direct consequence of gravitational focusing, which dominates even in these three-body encounters. The chance to have a relatively small impact distance is comparable to the chance of having a very large impact distance, which is against our naive intuition that the probability of a collision $\propto R_\star^2$.

4.5 Discussion and conclusions

We have studied the dynamics of the first stellar collision occurring in the evolution of young star clusters by means of high-accuracy direct N -body simulations. We have carried out about 500 simulations of star clusters represented by King models of different central concentration and different size.

During the early evolution of young dense clusters, massive stars sink to the core due to dynamical friction. As a result, the core becomes enhanced with massive stars, which can be seen in the flattening of the core mass function for $m \gtrsim 2\langle m \rangle$. Due to the steeper dependence of the binary formation cross-section on stellar mass than the collision cross-section, binary

formation becomes a more likely process than a collision. Young clusters are, in this respect, different from globular clusters, where binary formation by three-body encounters is unimportant (Hut & Verbunt, 1983).

Collisions occur after the formation of hard binaries in the core of the cluster. As expected, nearly all collisions occur in the core of the star cluster. The time of the first collision is roughly equal to the time required for the most massive colliding star to reach the core. While most of the collisions occur within a timescale of 50 N -body time units ($15t_{cc}$), we find that some of them are delayed to as much as a few hundred N -body time units. This is due to the fact that some of the massive stars that have reached the core are ejected from the cluster during dynamical encounters. This process postpones the first collision event to later times.

As for the geometry of the collision, we have found that most of the collisions occur between the primary star of a participating binary and a single star. The fraction of these collisions remains constant as the size of the cluster changes, except for the models W9R50 and W9R75 which are affected by stellar evolution. The masses of the primary star are distributed according to the core mass function but only for stars with $M_p \gtrsim 10 M_\odot$. The bullet stars, on the other hand, are single core stars.

One of the consequences of this geometry is that the impact velocity covers a wide range of values: from roughly 50% to 150% of the escape velocity from the two-body system formed by the two colliding stars. On the one hand, the low velocity tail of the impact velocity would be impossible if collisions were to occur between two unbound stars; however, this situation is to some degree similar to the merger of a binary. On the other hand, the high velocity tail can only occur if the dispersion velocity in the system is comparable to the escape velocity from the stellar surface. Such high velocity collisions may result in a significant mass loss or even destruction of a star (Freitag & Benz, 2005). As for the impact parameter, we have found that all collisions are dominated by gravitational focusing. The distribution of pericentre separations implies that nearly head-on collisions are as frequent as off-axis collisions.

As the collisions occur in a binary-single stellar system, there is a possibility that all stars may merge. If a single star merges with one of the binary members, the resulting collision product can expand by a large factor due to excess of thermal energy. In this case, the binary may become unstable and merge, and this therefore results in a triple merger. On the other hand, if the first encounter which involves a single star and a binary companion is not a head-on but rather grazing one, the possibly large impact velocity may prevent the merger all together. Therefore, to understand the fate of such systems one has to resort to hydrodynamic simulation.

4.A Mass function of binaries

In a given stellar population, it is possible to estimate the mass function of binary stars formed by three-body encounters. Let $\mathcal{N}(m)$ be the mass function of single stars in the region where binary formation takes place. Our aim here is to estimate the mass function of binaries formed by three-body encounters, $\mathcal{N}_{bin}(M_p, q)$. We wish to express this as a function of the mass of the primary star, M_p , which is the most massive binary companion, and the mass ratio, $q < 1$, of the secondary, which is the least massive binary companion, to the primary.

The probability to form a binary with a star of mass m_1 and another star of mass m_2 is proportional to the product of probabilities to randomly draw these stars from a mass function, $\mathcal{N}(m_1)\mathcal{N}(m_2)$, and the cross-section for these two stars to form a binary, $\Sigma(m_1, m_2)$. However, to form a binary a third star is required which carries away energy in order for m_1 and m_2 to form a bound system. In the further analysis, we assume that the mass of the third star is small compared to m_1 or m_2 and, therefore, it can be neglected in the cross-section of binary formation by three-body encounters.

Following Heggie & Hut (2003), we write the binary formation cross section in the following form

$$\Sigma(m_1, m_2)_b \propto (m_1 + m_2)/v_{12}^2. \quad (4.4)$$

Here, v_{12} is the relative velocity between two stars. Assuming energy equipartition, we write $v_{12}^2 \propto (m_1 + m_2)/(m_1 m_2)$, and Eq. 4.4 takes the following form

$$\Sigma_b(m_1, m_2) \propto m_1 m_2. \quad (4.5)$$

As we have mentioned above, the mass function of the dynamically formed binaries is

$$dF \propto dm_1 dm_2 \mathcal{N}(m_1) \mathcal{N}(m_2) \Sigma_b(m_1, m_2). \quad (4.6)$$

After the change of variables from (m_1, m_2) to $(M_p, q = M_s/M_p)$, were $M_p = \max(m_1, m_2)$ and $M_s = \min(m_1, m_2)$, this equation takes the following form

$$\frac{dF}{dq dM_p} = \mathcal{N}_{bin}(M_p, q) \propto q M_p^3 \mathcal{N}(M_p) \mathcal{N}(q M_p). \quad (4.7)$$

It is now possible to find the distribution of M_p and of q . The former can be obtained by integrating Eq. 4.7 over all possible mass ratios

$$\mathcal{N}_{bin}(M_p) = \int dq \mathcal{N}_{bin}(M_p, q), \quad (4.8)$$

and the latter is the integral of Eq. 4.7 over all primary masses

$$\mathcal{N}_{bin}(q) = \int dM_p \mathcal{N}_{bin}(M_p, q). \quad (4.9)$$

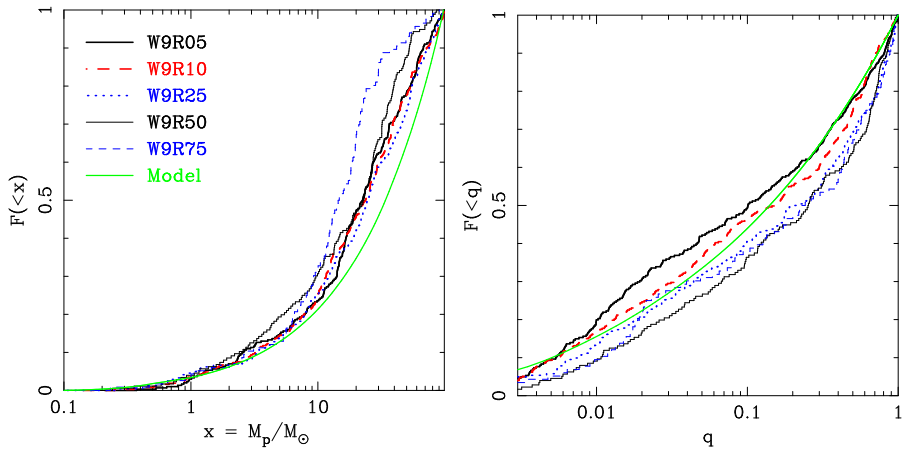


Figure 4.12: Primary mass (left) and mass ratio (right) distribution for dynamically formed binaries. The mass distributions of primary stars for W9R05, W9R10 and W9R25 models are consistent with a single distribution function better than at 30% level. The source of the discrepancy in the high-mass end of the mass function is due to the effects of stellar evolution on the initial mass function.

We compare both Eq. 4.8 and Eq. 4.9 with the simulations. Given the fact that most of the collisions occur in the core of a star cluster (see Sect. 4.3.2), we assume that binaries also form in the core. It was shown by Portegies Zwart et al. (2007b) that the mass function in the core is unchanged after the formation of the first hard binary. Thus, we assume that Eq. 4.1, which is the mass function at the moment of collision, is the mass function in the core of the star cluster at the moment of the formation of the first hard binary, $\mathcal{N}(m)$.

We extract the mass function of binaries which are formed by three-body encounters in the following way. For each simulation, we obtain the masses of the primary and the secondary star. Since some binaries persist for a long period of time, we make sure that the same binary is not used more than once. After that, we build distributions for the masses of the primary star and the mass ratio.

We show the resulting distributions, both from the simulations and from our semi-analytical estimates, in Fig. 4.12. It may be noted that models W9R50 and W9R75 lack massive stars. This is the result of stellar evolution that modifies the high-mass tail of the initial mass function. The effect is less pronounced in the W9R50 model and is unnoticeable in the rest of the models.

4.B Binary self-ejection

In this appendix, we estimate the minimal mass of a star cluster that can yield self-ejecting binaries.

Given a star cluster of mass M and half-mass radius R , its gravitational binding energy is

$$E \simeq \frac{GM^2}{4R}. \quad (4.10)$$

For simplicity, in this analysis we consider a binary which consists of two equal-mass stars of mass m_\star . The binding energy of such a binary of semi-major axis a is

$$E_b \simeq \frac{Gm_\star^2}{2a}. \quad (4.11)$$

In order to prevent a star cluster from collapse, the binary should be able to generate enough heat. In this case, we assume that the binding energy of the binary should be equal to the binding energy of the cluster. Combining Eq. 4.10 and Eq. 4.11, we show that this occurs when the semi-major axis of the binary is

$$a_{\text{eq}} \simeq 2R \left(\frac{m_\star}{M} \right)^2. \quad (4.12)$$

If a single stars with mass M_s star were to interact with such a binary, it would be ejected with a velocity of the order of the orbital velocity of the members of the binary, $v_{\text{orb}}^2 \simeq Gm_\star/a_{\text{eq}}$. In order to conserve linear momentum, the binary itself would recoil with velocity

$$v_{\text{rec}} = \frac{m_s}{2m_\star} v_{\text{orb}}. \quad (4.13)$$

Here, we assume that the mass of the low-mass star is equal to the mean stellar mass in the core, $\langle m_c \rangle$.

We estimate the escape velocity from the cluster in the following way

$$v_{\text{esc}}^2 \simeq \frac{2GM}{R}. \quad (4.14)$$

Combining Eq. 4.13 and Eq. 4.14, we express the condition $v_{\text{rec}} > v_{\text{esc}}$ as a condition on the minimal mass of the cluster which can yield ejected binary stars

$$M \gtrsim 16 \frac{m_\star^3}{m_s^2} \approx 2 \cdot 10^4 \left(\frac{m_\star}{50 M_\odot} \right)^3 \left(\frac{m_s}{10 M_\odot} \right)^{-2} M_\odot. \quad (4.15)$$

Chapter 5

Hydrodynamics of the first collision in young star clusters

Based on:

E. Gaburov, J. C. Lombardi and S. Portegies Zwart

Monthly Notices of the Royal Astronomical Society, to be submitted

ABSTRACT

Encounters between a binary and a single star are common in young star clusters. We model such interactions by means of Smoothed Particle Hydrodynamics (SPH), taking the initial conditions directly from N-body simulations, and compare the outcomes of our calculations against those of the sticky-sphere approximation. We find that, in many cases, the full hydrodynamic treatment yields significantly different results than those of the sticky-sphere approach. In cases in which all three stars merge, the hydrodynamic simulations show that: (1) mass lost as ejecta can be a considerable fraction of the total mass in the system (up to $\sim 25\%$); (2) due to asymmetric mass loss, the collision product can sometimes receive a kick velocity that exceeds 10 km/s, large enough to allow the collision product to escape the cluster; and (3) the energy of the ejected matter is large enough (up to $\sim 3 \times 10^{50}$ erg) to disturb appreciably or remove the inter cluster gas in many cases.

5.1 Introduction

Stars are born in clusters, which upon formation are generally dense and massive. In recent years, it has become clear that clusters remain bound even after losing a considerable fraction of their mass due to primordial outgassing (Baumgardt & Kroupa, 2007). The subsequent dynamical evolution of these clusters leads to a state of core collapse (Portegies Zwart et al., 2007b), almost irrespective of the number of primordial binaries (Portegies Zwart et al., 2004). Primordial binaries do, however, appear to delay the collapse of the core (Fregeau et al., 2003; Heggie et al., 2006).

Even if binaries are not present at the birth of a star cluster, they can form via three-body encounters during the process of core collapse. Indeed, the expansion of the cluster core after deep gravothermal collapse (Sugimoto & Bettwieser, 1983) is mediated by binaries, regardless of the presence or absence of a primordial population. During post-core collapse evolution, a cluster may enter a phase of gravothermal oscillations (Cohn et al., 1989), allowing periods of high interaction rate and providing further opportunity for binaries and single stars to interact closely.

Analytic expressions describing encounters between binaries and a third star, all treated as point masses, have been derived for various portions of parameter space by Heggie (1975), Hut (1983), and Heggie & Hut (1993). In addition, complementary numerical surveys have been performed in the point mass approximation by a number of authors (Harrington, 1970; Hut & Bahcall, 1983; Hills, 1992). During triple encounters, however, individual stars may approach each other so close that the approximation of point-particle dynamics breaks down: the size and internal structure of the stars then play a major role in determining the outcome of the encounter. Consequently, some numerical studies have augmented the point-mass treatment with simplified models that incorporate several hydrodynamic effects (McMillan, 1986; Fregeau et al., 2004). Large scale N -body simulations of star clusters have demonstrated the ubiquity of resonance interactions in dynamically unstable triples (Portegies Zwart et al., 1999), the scenarios that ultimately may lead to the coalescence of all three stars (Fregeau et al., 2004). The accurate modelling of the details under which triples merge, and whether or not two or all three stars in an encounter participate in the merger, have profound consequences for the occurrence of collision runaways (Portegies Zwart & McMillan, 2002; Freitag et al., 2006), and whether or not such runaways can lead to the formation of binaries between intermediate-mass black holes (Gürkan et al., 2006).

The first three-dimensional hydrodynamic calculations of encounters between a binary and a single star were performed by Cleary & Monaghan (1990), who use smoothed particle hydrodynamics (SPH) method in their studies. However, computational constraints at that time limited their work to a very small number of SPH particles (usually 136 per star) and to $n = 1.5$

polytropes, appropriate only for white dwarfs or low-mass main sequence stars. Subsequent hydrodynamic treatments of three-body interactions typically confined themselves to scenarios in which at least one of the stars was a compact object, and therefore could be treated as a point mass (e.g., Davies et al., 1993, 1994). Davies et al. (1998) and Adams et al. (2004) consider three-body encounters between a binary and a red giant star as a mechanism for destroying red giants near the centres of dense stellar systems. Their hydrodynamic simulations follow the fluid of the red giant envelope during the encounter, with the red giant core and both components of the binary being treated as point masses. Because only the red giant envelope is treated hydrodynamically, the only mergers that can result are those which form a binary of the two point masses surrounded by a common envelope donated from the red giant envelope (Lombardi et al., 2006).

Numerous hydrodynamic simulations of colliding stars have studied the structure of the merger product (Benz & Hills, 1987; Davies et al., 1994; Lombardi et al., 1995; Davies et al., 1998; Lombardi et al., 2002a; Freitag & Benz, 2005; Gaburov et al., 2008). In some cases the evolution of these collision products is studied further (Suzuki et al., 2007a), especially within the context of the formation and evolution of blue stragglers (Sills et al., 2001, 2005). Such collision studies, however, have been focused on encounters between two single stars, ignoring for the time being that collisional cross sections and rates can be larger for systems consisting of three or more stars.

The scenario of triple-star mergers among low mass main-sequence stars has been previously considered by Lombardi et al. (2003) using SPH. Their calculations indicate that the collision product always has a significantly enhanced cross-section and that the distribution of most chemical elements within the final product is not sensitive to many details of the initial conditions. They, however, concentrated solely on low mass stars and treated the triple star merger as two separate, consecutive parabolic collisions.

Recently, Gaburov et al. (2008a) performed an extensive and detailed study to investigate the circumstances under which a first collision between stars occurs. Using direct N -body integration with “sticky-spheres” of realistic stellar sizes, they argued that binaries tend to catalyse collisions. In their simulations, the binaries that are formed during core collapse tend to interact with an incoming star, which subsequently merges with one of the binary components. The results of Lombardi et al. (2003) suggest that the hydrodynamics of such interactions are unlikely to keep the binary itself undamaged. Instead, the stellar material that is expelled during a collision engulfs the system in a common envelope, leading to the merger of all three stars.

In this work, we introduce a new implementation of SPH and apply it to accurately follow the hydrodynamics of encounters between hard binaries and intruders. We concentrate on cases involving massive main sequence

stars, such as those found in young star clusters, treating all three stars simultaneously and with realistic orbital parameters determined from dynamical calculations of star clusters. In particular, the initial conditions are selected from the set of N -body simulations carried out by Gaburov et al. (2008a), but with the internal structure of the stars now being determined by a stellar evolution code. A comprehensive survey of triple-star collisions would need to explore an enormous amount of parameter space, but here we focus on a number of representative cases. In total, we selected 40 encounters from the simulations of Gaburov et al. (2008a). Among these are random selections, as well as some that are specifically chosen because of their relevance for the subsequent N -body evolution or because of their uncertain outcome given the relatively simple treatment of mergers in the N -body simulations.

This paper is structured as follows. In §5.2 we introduce our new formulation of SPH, which allows efficient use of non-equal mass particles, as well as our approach for relaxing single stars. In §5.3 we describe how we model close and contact binary star systems, and we demonstrate the stability of these systems at least for a time interval of interest. The set of initial conditions for the three-body collisions are presented in §5.4. Finally, §5.5 presents, while §5.6 discusses, the results of our calculations.

5.2 Methods and Conventions

5.2.1 SPH code

Smoothed Particle Hydrodynamics is the most widely used hydrodynamics scheme in the astrophysics community. It is a Lagrangian particle method, meaning that the fluid is represented by a finite number of fluid elements or “particles.” Associated with each particle i are, for example, its position \mathbf{r}_i , velocity \mathbf{v}_i , and mass m_i . Each particle also carries a purely numerical smoothing length h_i that determines the local spatial resolution and is used in the calculation of fluid properties such as acceleration and density (Monaghan, 1992; Rasio & Lombardi, 1999; Monaghan, 2005). The code which we used in this work was presented in (Lombardi et al., 2006). However, we modified equations of motion to allow the efficient use of non-equal mass particles.

5.2.2 Equations of motion

Our SPH equations of motion are derived from the standard SPH Lagrangian (Springel & Hernquist, 2002; Monaghan, 2002; Price & Monaghan, 2007). However, we modify the usual constraint on the smoothing length: the smoothing length h_i of a particle i is constrained to its density ρ_i via the relation $\rho_i h_i^3 = \text{const}$. This criteria, however, is unsatisfactory when non-

equal mass SPH particles are mixed since particles with mass much smaller than the average mass tend to have an unreasonably small number of neighbours, whereas particle with mass much larger than the average have a large number of neighbours. However, it is desirable to maintain a nearly constant number of neighbours, such that the local resolution is neither degraded by having too many neighbours nor are there too few neighbours to do meaningful interpolation. Therefore, in this work we introduce the following constraint for the smoothing length of a particle i :

$$N_i = \sum_j V(|\mathbf{r}_i - \mathbf{r}_j|, h_i). \quad (5.1)$$

Here, N_i is equal to the desired number of neighbours and $V(r, h) = U(4(h - |r - h|), h)$

$$U(x, h) = 4\pi \int_0^r W(x, h)x^2 dx, \quad (5.2)$$

where $W(x, h)$ is SPH smoothing kernel with a compact support of radius $2h$.

By using variational principle we derived modified SPH equations of motion as described in Monaghan (2002) (see also Springel & Hernquist (2002) and Price & Monaghan (2007)). The resulted hydrodynamic, $\mathbf{a}_{h,i}$, and gravitational, $\mathbf{a}_{g,i}$, accelerations take the following form:

$$\mathbf{a}_{h,i} = - \sum_j m_j \frac{P_j}{\rho_i^2} \left[\nabla_i W_{ij}(h_i) - \frac{\omega_i}{\Omega_i m_j} \nabla_i V_{ij}(h_i) \right] \quad (5.3)$$

$$- \sum_j m_j \frac{P_j}{\rho_j^2} \left[\nabla_i W_{ij}(h_j) - \frac{\omega_j}{\Omega_j m_i} \nabla_i V_{ij}(h_j) \right], \quad (5.4)$$

and

$$\mathbf{a}_{g,i} = -\frac{1}{2} \sum_j m_j [\nabla_i g_{ij}(h_i) + \nabla_i g_{ij}(h_j)] \quad (5.5)$$

$$+ \frac{1}{2} \sum_j m_j \frac{\Psi_i}{\Omega_i m_j} \nabla_i V_{ij}(h_i) \quad (5.6)$$

$$+ \frac{1}{2} \sum_j m_j \frac{\Psi_j}{\Omega_j m_i} \nabla_i V_{ij}(h_j). \quad (5.7)$$

In these equations,

$$\omega_j = \sum_k m_k \frac{\partial W(|\mathbf{r}_j - \mathbf{r}_k|, h_j)}{\partial h_j}, \quad (5.8)$$

$$\Omega_j = \sum_k \frac{\partial V(|\mathbf{r}_j - \mathbf{r}_k|, h_j)}{\partial h_j}, \quad (5.9)$$

$$\Psi_i = \sum_k m_k \frac{\partial g_{ik}(h_i)}{\partial h_i}, \quad (5.10)$$

and $g_{ij}(h) \equiv g(|\mathbf{r}_i - \mathbf{r}_j|, h)$ is a smoothed gravitational potential between two particles which itself depends on W (Price & Monaghan, 2007).

5.2.3 Integration in Time

The evolution equations are integrated using a symplectic integrator with shared symmetrised timesteps, as in Springel (2005). Our shared timestep is determined as

$$\Delta t = \text{Min}_i \left[\left(\Delta t_{1,i}^{-1} + \Delta t_{2,i}^{-1} \right)^{-1} \right], \quad (5.11)$$

where for each SPH particle i , we use

$$\Delta t_{1,i} = C_{N,1} \frac{h_i}{\text{Max} [\text{Max}_j (\kappa_{ij}), \text{Max}_j (\kappa_{ji})]} \quad (5.12)$$

with

$$\kappa_{ij} \equiv \left[\left(\frac{p_i}{\rho_i^2} + \frac{1}{2} \Pi_{ij} \right) \rho_i \right]^{1/2}, \quad (5.13)$$

and

$$\Delta t_{2,i} = C_{N,2} \frac{u_i}{|du_i/dt|}. \quad (5.14)$$

For the simulations presented in this paper, $C_{N,1} = 0.2$ to 0.3 and $C_{N,2} = 0.05$. The Max_j function in equation (5.12) refers to the maximum of the value of its expression for all SPH particles j that are neighbors with i . The denominator of equation (5.12) is an approximate upper limit to the signal propagation speed near particle i . The incorporation of Δt_2 enables us to treat shocks accurately without drastically decreasing the timestep during intervals in which the flow is subsonic.

5.2.4 Choice of Units

Throughout this paper, numerical results are given in units where $G = M_\odot = R_\odot = 1$, where G is the Newtonian gravitational constant and M_\odot and R_\odot are the mass and radius of the Sun. The units of time, velocity, and energy are then

$$t_u = \left(\frac{R_\odot^3}{GM_\odot} \right)^{1/2} = 1594 \text{ s}, \quad (5.15)$$

$$v_u = \left(\frac{GM_\odot}{R_\odot} \right)^{1/2} = 437 \text{ km s}^{-1}, \quad (5.16)$$

$$E_u = \frac{GM_\odot^2}{R_\odot} = 3.79 \times 10^{48} \text{ erg}. \quad (5.17)$$

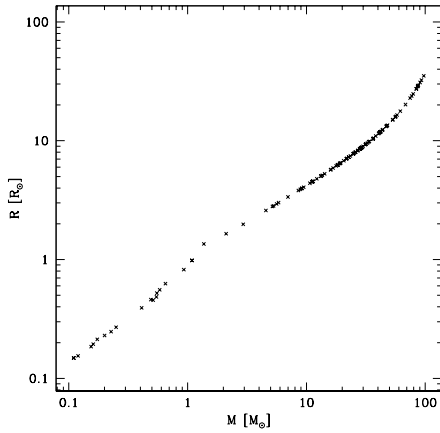


Figure 5.1: Stellar radius versus mass for the stars considered in this work.

5.2.5 Relaxing a single star

In order to initiate a triple star collision, we must prepare an SPH model of each star in isolation. To compute the structure and composition profiles of our parent stars, we use the TWIN stellar evolution code (Eggleton, 1971a; Glebbeek & Pols, 2008; Glebbeek, 2008) from the MUSE software environment¹. We evolve main sequence stars with initial helium abundance $Y = 0.28$ and metallicity $Z = 0.02$ for a time $t = 2$ Myr, a short enough age that even the most massive stars in a star cluster are still on the main sequence. The mass-radius relation which resulted from these calculations is shown in Figure 5.1.

Initially, we place the SPH particles on a hexagonal close packed lattice, with particles extending out to a distance only a few smoothing lengths less than the full stellar radius. After the initial particle parameters have been assigned according to the desired profiles from TWIN, we allow the SPH fluid to evolve into a state of hydrostatic equilibrium. During this calculation, we include the artificial viscosity contribution to the SPH acceleration equation so that energy is conserved, and we do not find it necessary to include a drag force on the particles. For the relaxation calculations of massive stars, we do however implement a trick that helps to keep low mass particles from being pushed to large radii: namely, during the initial stages of the relaxation, we implement a variation on the XSPH method (Monaghan, 1992, 2002), in which the velocity used to update positions is the average of the actual particle velocity and the desired particle velocity (zero). All of our relaxed models remain static and stable when left to dynamically evolve in isolation.

This approach allows us to model the desired profiles very accurately,

¹<http://muse.li>

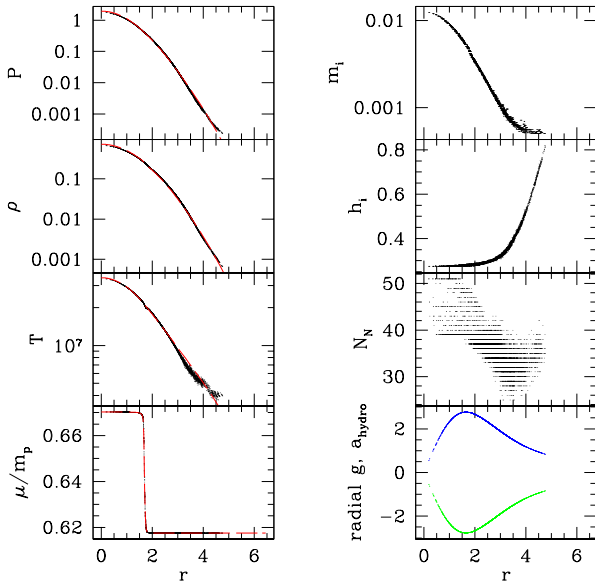


Figure 5.2: Properties of the SPH model of a $19.1M_\odot$ star. Profiles are shown as a function of radius, after relaxation for 730 time units. The frames in the left column show profiles of pressure P , density ρ , temperature T (in Kelvin), and mean molecular weight μ in units of the proton mass m_p , with the dashed curve representing results from the TWIN evolution code and dots representing particle data from our SPH model. The right column provides additional SPH particle data: individual SPH particle mass m_i , smoothing length h_i , number of neighbours N_N , and radial component of the hydrodynamic acceleration a_{hydro} (upper data) and gravitational acceleration g (lower data).

and we present an example in Figure 5.2, where we plot desired profiles and SPH particle data for a $19.1M_\odot$ star. The structure and composition profiles of the SPH model closely follow those from TWIN profiles, and the model remains stable when allowed to evolve dynamically.

5.3 Relaxing a binary star

In this section we present our algorithm to model the close binary systems that are used in most of the triple star collisions. The first step in creating a binary is to relax each of the two stellar components in isolation, as described in the previous section. In the case of detached binaries, we place these relaxed stellar models along the x -axis with their centres of mass separated by the desired separation r . For contact binaries, however, we begin with the well separated stars and gradually decrease the semi-major axis until

the desired separation is achieved, in order to minimise oscillations initiated by tidal forces. In all cases, the centre of mass of the system remains at the same place, which we choose to be the origin.

During the binary relaxation process, the positions of the particles within each star are adjusted at each timestep by simple uniform translations along the binary axis, such that the separation between the centres of mass equal to the desired separation r . Simultaneously, the angular velocity Ω_{orb} defining the co-rotating frame is continuously updated, such that the net centrifugal and gravitational accelerations of the two stars cancel exactly:

$$\Omega_{\text{orb}}^2 = -\frac{1}{2} \left(\frac{\sum_{\star 1} m_i \dot{v}_{x,i}}{\sum_{\star 1} m_i x_i} + \frac{\sum_{\star 2} m_i \dot{v}_{x,i}}{\sum_{\star 2} m_i x_i} \right). \quad (5.18)$$

Here, the Cartesian coordinate x is measured along to the binary semi-major axis; $\dot{v}_{x,i}$ is the acceleration of particle i parallel to the axis of the binary in an inertial frame. A centrifugal acceleration is given to all particles such that the system approaches a steady state corresponding to a synchronised binary. As in the relaxation process of a single star, we also include the artificial viscosity contribution to the SPH acceleration equation.

This approach allows us to create close binaries that remain in dynamically stable orbits for many hundreds of orbits, and presumably even longer. An example is presented in Fig. 5.3 and Fig. 5.4. In Fig. 5.3 we plot column densities of a contact binary both before and after dynamical evolution through over 600 orbits. In Fig. 5.4 we show time evolution of various energies for the same binary. The epicyclic oscillations, with a period of 650 time units, are clearly visible. The fact that the epicyclic period is more than an order of magnitude larger than the orbital period of 35 time units underscores how close this binary is to the dynamical stability limit. As a binary approaches this limit, the epicyclic period would formally approach infinity (Rasio & Shapiro, 1994). The innermost dynamically stable orbit then marks the transition when the squared frequency of the epicyclic oscillations passes from a positive to a negative value, so that the qualitative behaviour of perturbations changes from oscillatory to exponential. Throughout the calculation, the perturbations remain small and actually damp with time: the internal energy U remains constant to within about 0.03%, the gravitational energy W to within about 0.008%, and the kinetic energy to within about 0.2%. Meanwhile, the total energy is conserved exceptionally well, specifically to within about 0.0004%.

In another example we relaxed a contact binary between $92.9M_{\odot}$ and $53.3M_{\odot}$ with semi-major axis equal to $43.8R_{\odot}$. In Fig. 5.5 we show column density snapshots for every 50 time units (0.92 days) of the binary during and after relaxation process. We began the relaxation process with an initial semi-major axis of $55.8R_{\odot}$, and we decrease it to $43.8R_{\odot}$ in 500 time units (9.2 days). The top-most left panel shows a binary during relaxation at $t = 350$ units (6.5 days), and the semi-major axis at this time is equal to

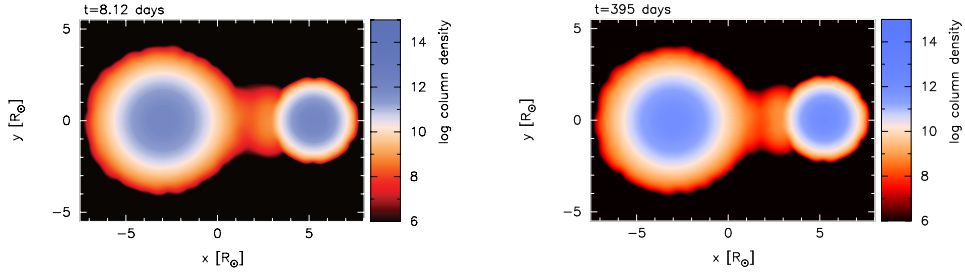


Figure 5.3: A contact binary consisting of a $12.2M_{\odot}$ primary and a $6.99M_{\odot}$ secondary both at the end of the relaxation (upper frame) and after dynamical evolution through more than 600 orbits (lower frame). Colours represent column density, measured in g cm^{-3} on a log scale, along lines of sight perpendicular to the orbital plane.

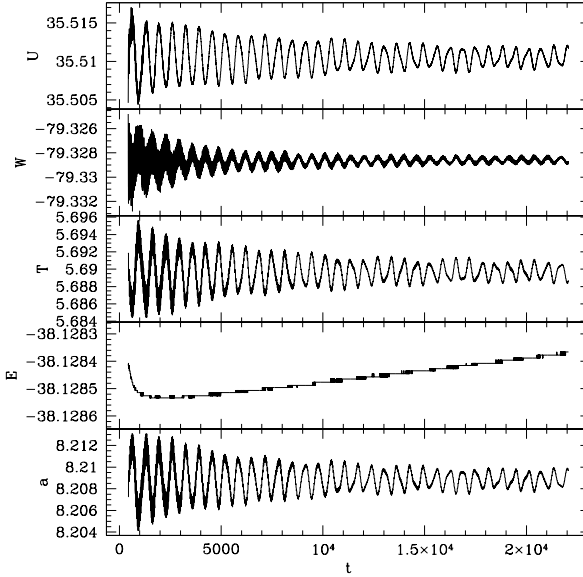


Figure 5.4: Internal energy U , gravitational potential energy W , kinetic energy T and total energy E versus time t for the dynamical evolution of an isolated contact binary consisting of a $12.2M_{\odot}$ primary and a $6.99M_{\odot}$ secondary. The orbital period is 35 time units, while the epicyclic period is 650 time units.

$48.0R_{\odot}$. It is possible to notice commencement of the mass transfer form the primary onto the secondary. At the time of 500 units (9.22 days), when the semi-major axis becomes $43.8R_{\odot}$, we stop the relaxation and dynamically evolve the system in the inertial frame. At this time half of the secondary star is already submerged in the fluid of the primary star. By the time of

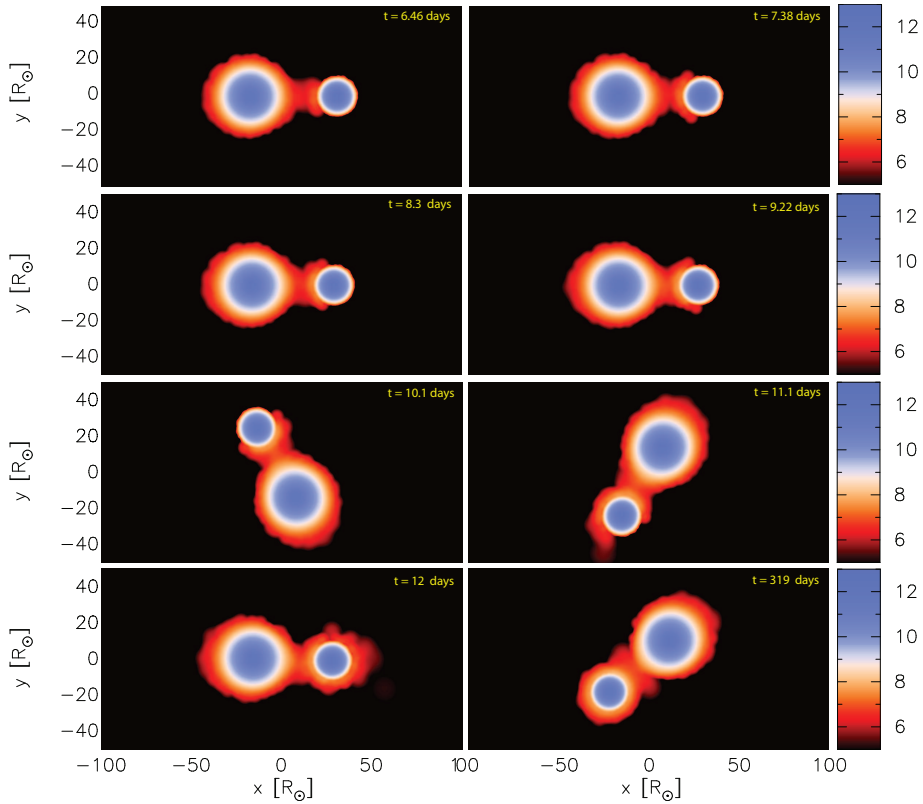


Figure 5.5: The relaxation and dynamical evolution of a close binary between $92.9M_{\odot}$ and $53.3M_{\odot}$ with the semi-major axis equal to $43.8R_{\odot}$. The calculation switches from a corotating frame to an inertial frame at a time of 9.22 days.

650 units (12 days), the secondary star is completely engulfed in the fluid of the primary star. The bottom-most right panel shows the binary at the time of 17300 units (319 days), and the semi-major axis maintains its value of $43.8R_{\odot}$. In Fig. 5.6 we show energy and semi-major axis of the binary as a function of time.

5.4 Initial conditions

The parameter space of three-body encounters is immense and leaves no hope of complete coverage with SPH simulations. The approach we take in this work is to study a part it by using the initial conditions obtained from realistic N -body simulation. In particular, we take initial condition for three-body collisions from Gaburov et al. (2008a) who carried out an extensive set of N -body simulations of young star clusters. In these simulations, the stars were modelled as hard spheres with a given mass and corresponding radius. A collision occurs when two spheres experience physical contact,

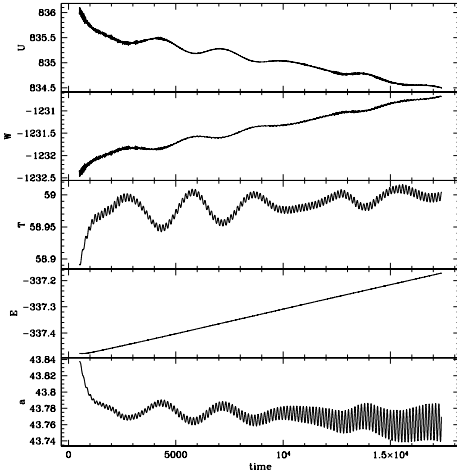


Figure 5.6: Internal energy U , gravitational potential energy W , kinetic energy T , total energy E and semi-major axis a versus time t for the dynamical evolution of an isolated close binary between a $92.9M_{\odot}$ primary and a $53.3M_{\odot}$ secondary stars. The orbital period of the binary is 150.6 time units (2.78 days), and the binary is therefore stable for more than 100 orbits. The small increase in the total energy occurs due to a few low mass particle that are escaping to infinity.

or in other words, when the separation between the centres of these spheres is equal to the sum of their radii. This treatment of collisions, known as the “sticky-sphere” approximation, conserves total mass and momentum.

In this paper, however, we resolve the stellar structure and focus on isolated three-body close interactions. This can be justified by the fact that usually such interactions last less than a year, and therefore local conditions hardly change on such a timescale. All three-body interactions we split in two groups: the interaction between a binary and a single star, and the interaction between three single stars which are in the middle of a resonant interaction. The latter case is straightforward to model, as we need to prepare only relaxed single star models, as described in §5.2, and then assign the appropriate initial positions and velocities to each of the stars. The actual dynamical interaction process is modelled with our SPH code.

In the case of an interaction between a binary and a single star, we initially relax the binary as described in §5.3. The binary separation is taken from the N -body simulations. Because most of the binaries have separations of a few stellar radii, tidal circularisation plays an important role, and therefore eccentricity is nearly equal to zero. In some of the cases, the synthetic stellar evolution part of N -body calculations predicts a binary separation too small to be dynamically stable, and in such circumstances we relax an SPH model of the binary near the smallest possible semi-major axis such that the binary remains stable.

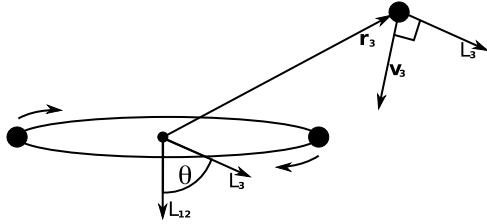


Figure 5.7: The orientation of a binary and an intruder star. Here, θ is the angle between two angular momentum vectors: one of the binary, L_{12} , and one of the intruder star with respect to the binary centre of mass, L_3 .

Table 5.1 describes the initial positions and trajectories in a way that is meant to aid in the mental visualisation of each scenario; in almost all of these scenarios, the eccentricity of the trajectory of the intruder about the binary is nearly parabolic ($0.9 < e < 1.1$). For example, in Table 5.1, comparing the periastron separation $r_{\text{p,ib}}$ to the binary semimajor axis a_{12} provides an indication of where within the binary the intruder strikes. The ratio E_{ib}/E_{12} gives a measure of how much energy is being brought to the system by the intruder, relative to the binding energy of the binary. Since binding energy between two stars is always negative quantity, the positive value of E_{ib}/E_{12} implies that the intruder star is bound to the binary, otherwise it is unbound. We note, however, that the magnitude of this ratio is mostly much less than one, which corresponds to nearly parabolic encounter between the intruder and the binary star. The final column indicates the angle of approach of the intruder toward the binary, with $0 \leq \theta \leq 180^\circ$. More precisely, the angle θ is the angle between the angular momentum vector of the binary and the angular momentum vector of the intruder calculated about the center of mass of the binary (Fig. 5.7). For example, $\theta = 0$ corresponds to coplanar trajectories with the intruder orbiting the binary in the same direction (clockwise or counter-clockwise) as the binary is orbiting; $\theta = 90^\circ$ corresponds to the third star incident on the binary from a direction perpendicular to the orbital plane of the binary; and $\theta = 180^\circ$ again corresponds to coplanar trajectories, although now the intruder approaches with an angular momentum that is antiparallel to that of the binary. All of our initial binaries are on nearly circular orbits ($e_{12} < 0.02$), with the exceptions of those in scenario 249 ($e_{12} = 0.41$).

We initiate two types of hydrodynamic calculations of triple collisions. The first type, which comprises the majority of our calculations, consists of a co-rotating binary intruded upon by a third star. In these situations, a circular binary is relaxed by the means described in §5.3. If it is a contact binary, then the circular orbit is maintained with the orbital plane, and the phase is shifted to match those of the desired initial conditions. In the case

id	$m_{b,1}$	$m_{b,2}$	m_i	a_{12}	$r_{p,ib}$	E_{ib}/E_{12}	θ
203	47.1	36.3	1.09	33.8	33.3	-7.6e-3	80
206	24.6	21.9	20.6	13.3	7.46	+1.7e-1	68
207	42.2	18.2	0.65	30.6	16.3	+3.0e-1	124
208	86.7	0.16	0.51	54.0	6.27	+3.8e-2	41
211	61.7	8.89	18.4	23.3	52.8	+1.1e-1	42
212	87.6	27.1	22.7	35.1	10.9	-7.0e-2	102
213	76.8	13.6	0.23	32.3	2.77	+2.2e-3	160
217	86.4	28.9	0.11	51.1	9.58	+1.2e-3	123
222	22.8	11.1	5.28	34.8	10.5	+3.4e-1	73
223	28.6	4.57	19.4	13.0	12.1	-4.3e-3	107
224	48.1	22.0	0.2	22.5	5.85	+2.6e-3	147
227	16.0	0.17	5.62	25.6	4.05	-1.2e-1	59
231	25.8	0.411	26.1	26.0	12.9	-4.4e-1	43
232	12.2	6.99	19.1	8.26	2.10	+1.7e-4	20
233	28.9	2.94	47.6	26.7	12.2	+1.0e-2	91
236	40.5	31.4	29.3	23.5	19.2	+1.4e-2	84
241	28.1	11.3	41.7	13.6	12.8	-1.6e-2	51
245	43.5	16.0	79.1	33.2	32.7	-2.0e-2	97
242	41.1	23.5	0.490	21.3	1.54	-2.5e-3	142
246	42.2	38.3	1.37	28.4	19.1	+8.7e-3	161
249	74.7	0.11	0.15	101	5.88	-1.6e-1	51
250	44.0	31.9	0.550	36.4	3.48	-2.1e-1	63
253	53.4	8.55	0.583	22.4	12.5	-2.5e-2	35
256	33.4	2.11	5.84	18.6	7.50	-5.2e-2	58
257	97.3	24.9	5.18	51.5	2.69	-2.9e-1	132
258	90.4	0.55	0.93	28.6	10.2	-3.5e-3	86
259	55.9	21.7	11.4	26.3	6.72	+2.9e-2	46
260	92.9	53.3	13.3	43.9	54.6	+5.7e-1	14
267	28.6	14.2	19.1	26.3	0.28	-5.3e-1	126
298	56.7	25.3	28.1	26.2	18.9	-1.8e-1	143
299	52.3	16.9	52.3	26.2	0.0	-0.952e-4	94

Table 5.1: In the first column, we present the scenario identification number. The second and third columns show the masses of the components of the binary, while the fourth column gives the mass of the intruder. The fifth column gives the semimajor axis a_{12} of the binary. Column 6 gives the periastron separation $r_{p,ib}$ of the equivalent two-body Kepler orbit between the intruder and the center of mass of the binary. Column 7 gives the ratio of the energy E_{ib} in this orbit of the intruder and binary to the binding energy E_{12} of the binary itself. Column 8 gives the angle θ , in degrees, between the angular momentum of the binary and the angular momentum of the intruder about the binary.

id	m_1	m_2	m_3
201	84.1	0.25	27.1
202	57.9	0.12	29.9
204	42.4	11.5	16.5
214	9.49	16.8	17.8
219	36.6	9.10	10.7
220	84.3	68.3	32.7
257	5.18	24.9	97.3
261	33.9	13.2	9.17
262	29.3	31.5	18.4

Table 5.2: The masses of single stars which participate in the resonance interaction. The first column show the case number, while the second, third and forth columns display the masses of participating stars.

of a detached binary, the velocity of each star is adjusted to give desired orbital orientation, phase and eccentricity as well. In this way, we account for tidal bulging in the binary components. The third star, relaxed by the means described in §5.2, is initially non-rotating and separated from the binary by many times the radius of the larger star, which allows tidal effects on it to be neglected in the initial configuration.

The second type of hydrodynamic calculation involves the collision of three individual stars (Table 5.2). These scenarios also represent cases in which a binary has been disrupted by an intruder, but here the three stars orbit in long-lived resonant interactions that would be too computational expensive to follow with a hydrodynamic code in their entirety. Each of the three stars is first relaxed by the means described in §5.2. Their initial positions and velocities in the collision calculation represent a snapshot from the point mass dynamical calculation in which the stars were widely separated but nearing the end of their resonant interaction.

5.5 Results

In this section, we report on the results of simulations of 40 different encounters between three parent stars. In terms of computational time, most of the runs with $N \sim 10^4$ lasted somewhere between a week or two on a modern PC at the time of writing, which is equipped with an MD-GRAPE2 (Fukushige et al., 1996) card or a GPU (Hamada & Iitaka, 2007; Belleman et al., 2008) for self-gravity calculation. Our higher resolution calculations ($N \sim 10^5$) would typically take up to few months to complete; the total number of integration steps are usually between 10^5 and 10^6 .

id	method	outcome	speed [km/s]	f_L	E_{ej} [10^{48} erg]
201	pm	(1,2,3) → (1,2),3			
	ss	(1,2,3) → ({1,3},2)	0		
14118		(1,2,3) → ({1,3},2)	< 0.1	< 0.001	< 0.1
28296		(1,2,3) → ({1,3},2)	< 0.1	< 0.001	< 0.1
113046		(1,2,3) → ({1,3},2)	< 0.1	< 0.001	< 0.1
202	pm	(1,2,3) → (1,2),3			
	ss	(1,2,3) → ({1,3},2)	0		
6138		(1,2,3) → ({1,3},2)	< 0.1	< 0.001	< 0.1
11466		(1,2,3) → ({1,3},2)	< 0.1	< 0.001	< 0.1
22380		(1,2,3) → ({1,3},2)	< 0.1	< 0.001	< 0.1
91956		(1,2,3) → ({1,3},2)	< 0.1	< 0.001	< 0.1
203	pm	(1,2),3 → (1,2,3) → (1,2),3			
	ss	(1,2),3 → (1,2,3) → ({1,3},2)	0		
10398		(1,2),3 → (1,2,3) → ({1,3},2)	< 0.1	< 0.001	0.13
204	pm	(1,2,3) → (1,3), 2			
	ss	(1,2,3) → ({1,3},2) → {2,{1,3}}			
11946		(1,2,3) → ({1,2},3) → {{1,2},3}	7.2	0.13	12.
60024		(1,2,3) → ({1,2},3) → {{1,2},3}	3.8	0.082	12.
206	pm	(1,2),3 → (1,2,3) → (1,2),3			
	ss	(1,2),3 → (1,{2,3}) → {{2,3},1}	0		
14475		(1,2),3 → (1,2,3) → ({1,2},3) → {{1,2},3}	1.2	0.048	13.
207	pm	(1,2),3			
	ss	(1,2),3 → (1,{2,3})	0		
9492		(1,2),3	0		
208	pm	(1,3),2			
	ss	(1,3),2 → ({1,2},3)	0		
15018		(1,3),2 → ({1,2},3)	< 0.1	< 0.001	0.22
211	pm	(1,3),2			
	ss	(1,3),2 → {1,3},2			
11028		(1,3),2 → {1,3},2	39	0.026	6.7
212	pm	(1,2),3 → (1,2,3) → (1,3),2			
	ss	(1,2),3 → ({1,3},2) → {{1,3},2}	0		
22080		(1,2),3 → (1,2,3) → ({1,3},2) → {{1,3},2}	3.6	0.17	66.
213	pm	(1,2),3			
	ss	(1,2),3 → ({1,3},2)	0		
13314		(1,2),3 → ({1,3},2)	< 0.1	< 0.001	< 0.1
125130		(1,2),3 → ({1,3},2)	< 0.1	< 0.001	1.5
214	pm	(1,2,3) → (1,2),3			
	ss	(1,2,3) → ({1,2},3)	0		
11016		(1,2,3) → ({2,1},3) → {{2,1},3}	1.4	0.14	3.9
217	pm	(1,2),3 → (1,2,3) → (1,2),3			
	ss	(1,2),3 → ({1,3},2)	0		
17442		(1,2),3 → ({1,3},2)	< 0.1	< 0.001	< 0.1
139656		(1,2),3 → ({1,3},2)	< 0.1	< 0.001	< 0.1
219	pm	(1,2,3) → (1,2),3			
	ss	(1,2,3) → ({1,3},2) → {{1,3},2}	0		
14160		(1,2,3) → ({1,2},3) → {{1,2},3}	8.1	0.038	33.
220	pm	(1,2,3) → (1,2),3			
	ss	(1,2,3) → ({1,2},3) → {{1,2},3}			
20178		(1,2,3) → (1,{2,3}) → {{2,3},1}	14.	0.062	130
46296		(1,2,3) → (1,{2,3}) → {{2,3},1}	11.	0.062	130
222	pm	(1,2),3			
	ss	(1,2),3 → ({1,3},2) → {{1,3},2}	0		
17076		(1,2),3	0		
223	pm	(1,3),2 → (1,2,3) → (1,2),3			
	ss	(1,3),2 → ({1,2},3) → {{1,2},3}	0		
12456		(1,3),2 → (1,2,3) → ({2,1},3) → {{2,1},3}	12.	0.25	14.
224	pm	(1,2),3			

	ss	$(1,2),3 \rightarrow (\{1,3\},2)$	0		
14472		$(1,2),3 \rightarrow (1,2,3) \rightarrow (\{1,3\},2) \rightarrow \{\{1,3\},2\}$	0.94	0.023	3.4
227	pm	$(1,3),2 \rightarrow (1,2,3) \rightarrow (1,3),2$			
	ss	$(1,3),2 \rightarrow (\{1,2\},3) \rightarrow \{\{1,2\},3\}$	0		
10008		$(1,3),2 \rightarrow (1,2,3) \rightarrow (\{1,2\},3) \rightarrow \{\{1,2\},3\}$	3.6	0.027	2.3
231	pm	$(2,3),1 \rightarrow (1,2,3) \rightarrow (1,2),3$			
	ss	$(2,3),1 \rightarrow \{1,2\},3$	0		
13554		$(2,3),1 \rightarrow (1,2,3) \rightarrow (\{1,3\},2) \rightarrow \{2,\{1,3\}\}$	0.25	0.036	1.9
232	pm	$(2,3),1 \rightarrow (1,2,3) \rightarrow (1,2),3$			
	ss	$(2,3),1 \rightarrow (1,\{2,3\}) \rightarrow \{\{2,3\},1\}$	0		
13110		$(2,3),1 \rightarrow (\{1,3\},2) \rightarrow \{\{1,3\},2\}$	4.0	0.067	20.
233	pm	$(2,3),1 \rightarrow (1,3),2$			
	ss	$(2,3),1 \rightarrow (\{1,2\},3) \rightarrow \{\{1,2\},3\}$	0		
13020		$(2,3),1 \rightarrow (1,2,3) \rightarrow (\{1,2\},3) \rightarrow \{\{1,2\},3\}$	3.7	0.17	20
236	pm	$(1,2),3 \rightarrow (1,2,3) \rightarrow (2,3),1$			
	ss	$(1,2),3 \rightarrow (1,\{2,3\}) \rightarrow \{\{2,3\},1\}$	0		
12672		$(1,2),3 \rightarrow (1,2,3) \rightarrow (\{1,2\},3) \rightarrow \{\{1,2\},3\}$	5.8	0.14	25.
241	pm	$(2,3),1 \rightarrow (1,2,3) \rightarrow (1,3),2$			
	ss	$(2,3),1 \rightarrow (\{1,3\},2) \rightarrow \{\{1,3\},2\}$	0		
19956		$(2,3),1 \rightarrow (1,2,3) \rightarrow (\{1,3\},2) \rightarrow \{\{1,3\},2\}$	8.0	0.086	32.
242	pm	$(1,2),3$			
	ss	$(1,2),3 \rightarrow (\{1,3\},2) \rightarrow \{\{1,3\},2\}$	0		
10224		$(1,2),3 \rightarrow (1,2,3) \rightarrow (\{1,3\},2) \rightarrow \{2,\{1,3\}\}$	0.26	0.016	2.0
245	pm	$(2,3),1 \rightarrow (1,2,3) \rightarrow (1,2),3$			
	ss	$(2,3),1 \rightarrow (\{1,3\},2) \rightarrow \{\{1,3\},2\}$	0		
16884		$(2,3),1 \rightarrow (1,2,3) \rightarrow (\{1,2\},3) \rightarrow \{\{1,2\},3\}$	5.3	0.027	26.
246	pm	$(1,2),3$			
	ss	$(1,2),3 \rightarrow (1,\{2,3\}) \rightarrow \{1,\{2,3\}\}$	0		
5232		$(1,2),3 \rightarrow (1,2,3) \rightarrow (\{1,3\},2) \rightarrow \{2,\{1,3\}\}$	2.5	0.017	7.6
10554		$(1,2),3 \rightarrow (1,2,3) \rightarrow (1,2),3 \rightarrow \{1,2\},3$	11.8	0.010	3.7
21204		$(1,2),3 \rightarrow (1,2,3) \rightarrow (1,\{2,3\}) \rightarrow \{1,\{2,3\}\}$	1.1	0.023	6.3
42294		$(1,2),3 \rightarrow (1,2,3) \rightarrow (1,\{2,3\}) \rightarrow \{1,\{2,3\}\}$	0.71	0.020	5.3
249	pm	$(1,3),2 \rightarrow (1,2,3) \rightarrow (1,3),2$			
	ss	$(1,3),2 \rightarrow (\{1,2\},3)$	0		
10374		$(1,3),2 \rightarrow (\{1,2\},3)$	< 0.1	< 0.001	< 0.1
82812		$(1,3),2 \rightarrow (\{1,2\},3)$	< 0.1	< 0.001	< 0.101
250	pm	$(1,2),3 \rightarrow (1,2,3) \rightarrow (1,2),3$			
	ss	$(1,2),3 \rightarrow (1,2,3) \rightarrow (\{1,3\},2)$	0		
10254		$(1,2),3 \rightarrow (1,2,3) \rightarrow (\{1,3\},2)$	0.4	< 0.001	0.50
253	pm	$(1,2),3$			
	ss	$(1,2),3 \rightarrow (\{1,3\},2)$	0		
10374		$(1,2),3 \rightarrow \{1,2\},3$	1.0	0.032	5.3
256	pm	$(1,3),2 \rightarrow (1,2,3) \rightarrow (1,3),2$			
	ss	$(1,3),2 \rightarrow (\{1,2\},3) \rightarrow \{\{1,2\},3\}$	0		
10200		$(1,3),2 \rightarrow (1,2,3) \rightarrow (\{1,2\},3) \rightarrow \{\{1,2\},3\}$	7	0.15	11.
257	pm	$(1,2,3) \rightarrow (1,2),3$			
	ss	$(1,2,3) \rightarrow (\{1,3\},2) \rightarrow \{\{1,3\},2\}$	0		
10236		$(1,2,3) \rightarrow (\{1,3\},2) \rightarrow \{\{1,3\},2\}$	2.9	0.087	36.
258	pm	$(1,3),2$			
	ss	$(1,3),2 \rightarrow (\{1,2\},3) \rightarrow \{\{1,2\},3\}$	0		
10104		$(1,3),2 \rightarrow (1,2,3) \rightarrow (\{1,2\},3) \rightarrow \{\{1,2\},3\}$	0.6	< 0.001	2.0
259	pm	$(1,2),3$			
	ss	$(1,2),3 \rightarrow (\{1,3\},2) \rightarrow \{\{1,3\},2\}$	0		
10272		$(1,2),3 \rightarrow (1,2,3) \rightarrow (\{1,3\},2) \rightarrow \{\{1,3\},2\}$	5	0.085	30.
260	pm	$(1,2),3 \rightarrow (1,2,3) \rightarrow (1,2),3$			
	ss	$(1,2),3 \rightarrow (1,\{2,3\})$	0		
22518		$(1,2),3 \rightarrow \{1,2\},3$	14	0.024	6.6
261	pm	$(1,2,3) \rightarrow (1,2),3$			
	ss	$(1,2,3) \rightarrow (\{1,3\},2)$	0		
10092		$(1,2,3) \rightarrow (\{1,3\},2)$	7.1	0.020	22.
262	pm	$(1,2,3) \rightarrow (1,2),3$			

	ss	$(1,2,3) \rightarrow (1,\{2,3\})$	0		
	10314	$(1,2,3) \rightarrow (1,2),3 \rightarrow \{2,1\},3$	68	0.011	2.1
267	pm	$(1,3),2 \rightarrow (1,2),3$			
	ss	$(1,3),2 \rightarrow (\{1,3\},2) \rightarrow \{2,\{1,3\}\}$	0		
	14934	$(1,3),2 \rightarrow (\{1,2\},3) \rightarrow \{\{1,2\},3\}$	9.6	0.063	67.
298	pm	$(1,3),2 \rightarrow (1,2,3) \rightarrow (1,2),3$			
	ss	$(1,3),2 \rightarrow (\{1,2\},3) \rightarrow \{\{1,2\},3\}$	0		
	13818	$(1,3),2 \rightarrow (1,2,3) \rightarrow (\{1,3\},2) \rightarrow \{\{1,3\},2\}$	7	0.21	52.
299	pm	$(1,3),2 \rightarrow (1,2,3) \rightarrow (2,3),1$			
	ss	$(1,3),2 \rightarrow (\{1,2\},3) \rightarrow \{\{1,2\},3\}$	0		
	10194	$(1,3),2 \rightarrow (\{1,2\},3) \rightarrow \{\{1,2\},3\}$	6.9	0.15	310
	102540	$(1,3),2 \rightarrow (\{1,2\},3) \rightarrow \{\{1,2\},3\}$	2.7	0.16	330

Table 5.3: The first column gives the scenario identification number. The second column either gives the number N of SPH particles used to simulate this scenario, or names the treatment as “pm” (point mass) or “ss” (“sticky-spheres”). The third column summarizes the interaction that resulted. The fourth column lists the projected speed(s) at infinity of the resulting object(s), in units of km s^{-1} . The fifth column gives the fractional mass loss 200 time units after the final change of state, while the sixth column lists the total ejecta energy, in units of 10^{48} erg, at that same time.

In Table 5.3 we summarise the outcomes of all collisions from Tables 5.1 and 5.2. Binaries are represented by $(1, 2)$, whereas resonances are represented by $(1, 2, 3)$, with the masses satisfying $M_1 > M_2 > M_3$. The merger product between stars 1 and 2, due either to a binary coalescence or a direct collision, is represented using curly brackets, $\{1, 2\}$, where the more massive component *at the time of the merger* is listed first. In addition, the notation can be embedded. Consider, for example, scenario 242 with the following interaction sequence: $(1,2),3 \rightarrow (1,2,3) \rightarrow (\{1,3\},2) \rightarrow \{2,\{1,3\}\}$. The initial state $(1,2),3$ represents a primary 1 and a secondary 2 in a binary being intruded upon by the least massive star 3. The $(1,2,3)$ indicates that there is neither an immediate retreat of the intruder nor an immediate merger, but instead the three stars move in a resonant interaction. The state $(\{1,3\},2)$ means that the intruder next merges with the primary, leaving the merger product in a binary with the secondary star. Finally, $\{2,\{1,3\}\}$ indicates that these two remaining objects coalesce. Note that in this final state, the secondary star is listed before $\{1,3\}$ within the outer curly brackets, because the former was more massive at the time of the merger due to dynamical mass transfer during the final stages binary in-spiral.

Here, we chose scenario 232 as the case of interest. In Figures 5.8 and 5.9 we show trajectories and column density plots from calculations of this case, in which a $12.2 + 6.99M_\odot$ binary collides with a $19.1M_\odot$ intruder. The set up of the initial conditions for these three particular stars is described in §5.2 (Figs. 5.2, 5.3 and 5.4). Figure 5.9a shows the three bodies shortly after the start of the calculation. Figure 5.9b shows the three bodies just prior to the impact and merger of the intruder and the secondary from the binary. The first apocentre passage in the resulting binary star is shown in Figure 5.9c, while Figure 5.9d shows the binary in the process of merger. In

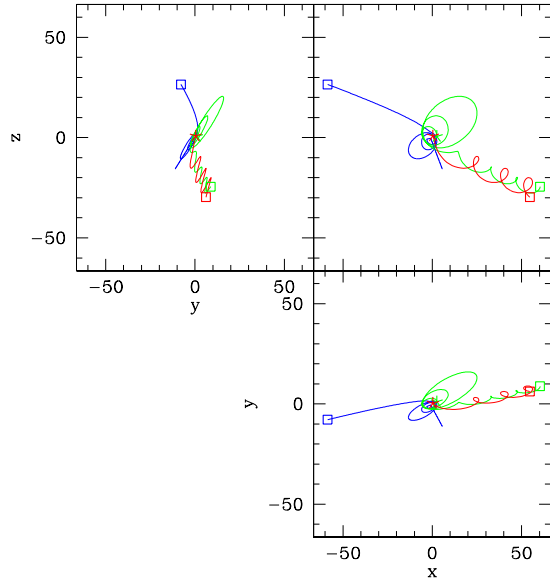


Figure 5.8: Trajectories in the xy (lower right), xz (upper right), and yz (upper left) planes for scenario 232, as given by our hydrodynamics calculation. The initial conditions are marked by squares, while the final position of an object before merger is marked by a 5-point asterisk.

Figure 5.9e we show the snapshot shortly after the fluid from the three stars has merged into a single object, and finally, Figure 5.9f shows a snapshot from near the end of our calculation: the merger product has drifted away from the origin due to asymmetric mass loss. In this scenario, the merger product has little angular momentum and the calculated mass loss quickly asymptotes to a constant value of approximately $2.6M_{\odot}$ (see Fig. 5.10).

Another case of interest is scenario 260, in which a massive binary star being perturbed by a slightly less massive intruder. In this case, the intruder is a catalyst which triggers binary merger. In the Figure 5.11 we show time evolution of energies (left panel) and global quantities (right panel), such as masses of individual stars and ejected fluid. In Figure 5.12 we present time snapshots of the column density from the calculations of this scenario. Figure 5.12a shows a snapshot at the beginning of the simulations, and Figure 5.12b shows a snapshot at the moment of closest approach between the intruder star and the binary. The binary merger process is shown in Figures 5.12c, 5.12c and 5.12e where it can be seen that fluid is gradually lost from outer Lagrangian points. Finally, the merged binary is shown in Figure 5.12f. In contrast to scenario 232, binary orbital angular momentum is converted into spin of the product, and this explains elongated shape of the collisions product in Figure 5.12f. One may also notice that the collision

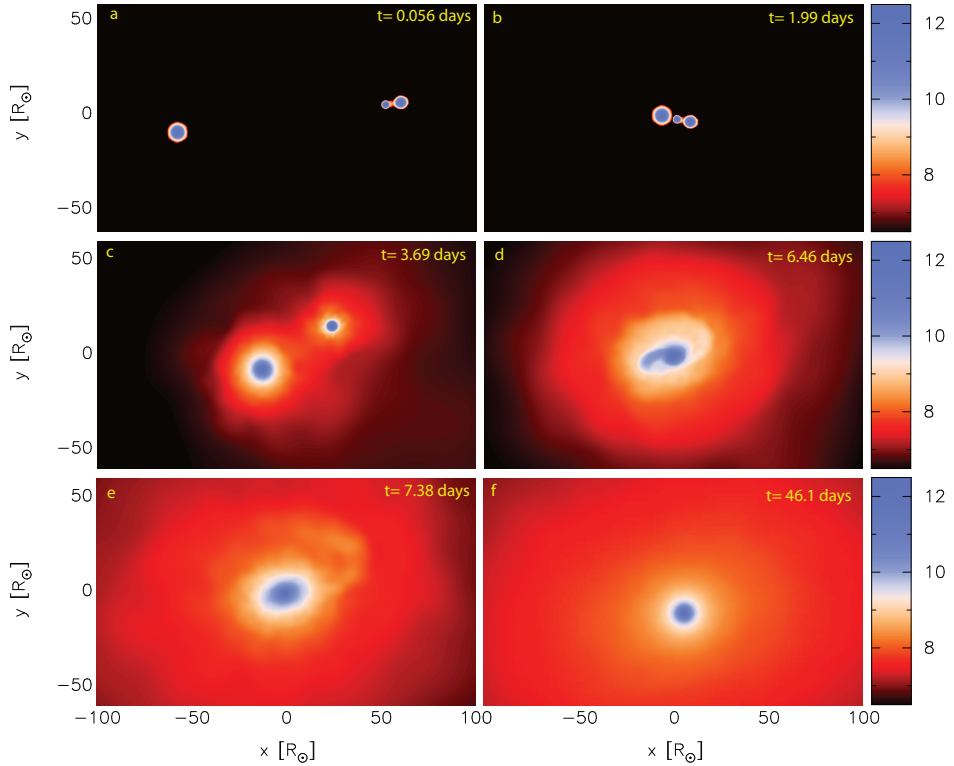


Figure 5.9: Column density along lines of sight perpendicular to the xy plane at various times for the same hydrodynamic calculation of scenario 232 presented in Figure 5.8.

product is quickly drifting away from the centre with velocity of 14 km/s. Most of this kick velocity comes from the escaping intruder star rather than from the asymmetric mass ejection.

The second episode of mass ejection, which occurs after merger of the binary, as can be seen in the right panel of Figure 5.11 for $t \gtrsim 8000$, is an artifact of the artificial viscosity (AV) used in SPH. Initially, the collision product is in the state of both differential rotation and hydrostatic equilibrium. It is however a known effect that AV tends to transfer angular momentum (AM) from the quickly rotating shells to slower ones (Lombardi et al., 1999). Since the inner regions of the collision product are spinning much faster than the outer ones, the AM is transferred outwards. The net effect is that the inner regions of the collision product contract, because of loss of the rotational support, but the outer regions expand because of the continuously increasing supply of AM, and this case be seen in Fig. 5.13. Eventually, these outer regions become unbound and escape, and this result in the second episode of the mass loss.

From the data of Table 5.3, we note that in the case when only two

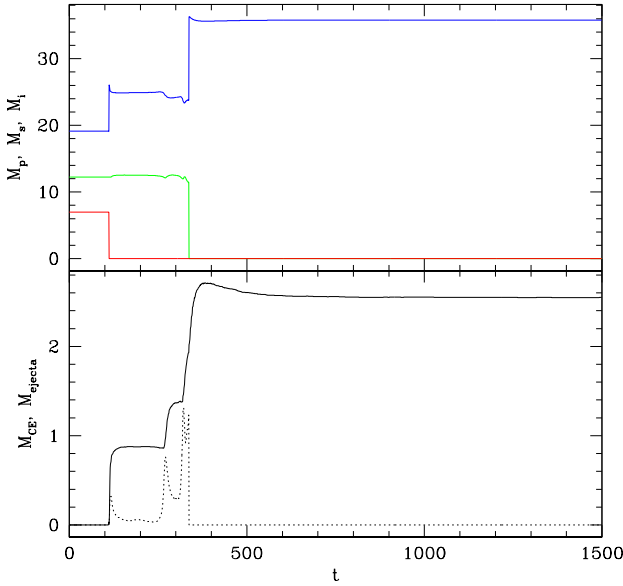


Figure 5.10: Masses versus time for scenario 232. The top frame shows the time evolution of the mass of the primary, secondary, and intruder. The bottom frame shows the amount of mass ejected (solid curve) and bound in a circumbinary envelope (dotted curve).

stars merge, the mass loss never exceeds a few percent and is often much less than this. It is known that mass loss in parabolic collision between two main-sequence stars is small (Freitag & Benz, 2005; Gaburov et al., 2008). The mass loss percentage is typically larger for scenarios in which all three stars ultimately merge, exceeding 10% in the hydrodynamic simulations of scenarios 212, 214, 223, 233, 236, 256, and 298. The hydrodynamic evolution in these more extreme cases is qualitatively similar from case to case: the first merger event is between the most massive main-sequence star and one of the other two, and typically occurs after a quick resonant interaction. The resulting merger product is enhanced in size by shock heating and rotation, leaving its outermost layers loosely bound. The third star, often after being flung out to large distances, can make several periastron passes through the envelope of the first merger product before ultimately donating its fluid to the mix. In this process, substantial amounts of gas are ejected from the diffuse envelope at every periastron passage.

An example of this type of interaction is summarised in Figures 5.14 and 5.15, for scenario 298. The features of these curves can be associated with events during the encounter. In this situation, the intruding star initiates a short lived resonance that ends with the induced merger of the binary

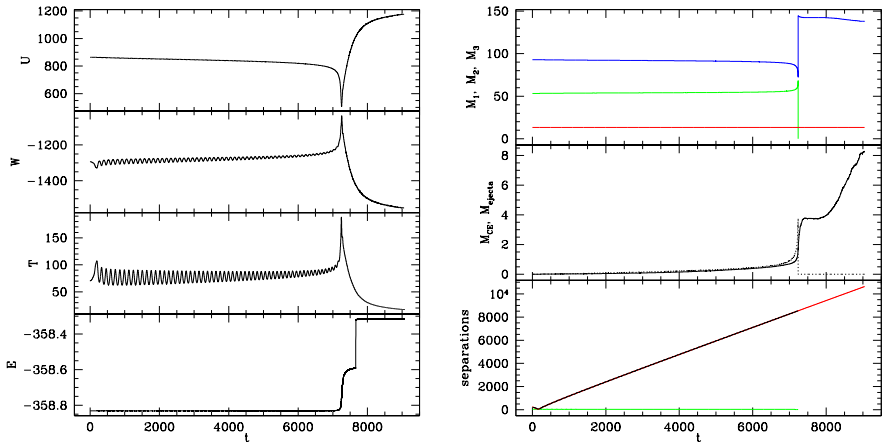


Figure 5.11: On the left panel we show the evolution of internal energy U , gravitational potential energy W , kinetic energy T and total energy E . On the right panel we display time evolution of stellar masses and separations. The top frame shows the masses of components 1, 2, and 3, represented by blue, green, and red curves, respectively. The middle frame plots the amount of mass ejected (solid curve) and bound in a circumbinary envelope (dotted curve). The bottom curves show the separations between components 1 and 2 (green), between 1 and 3 (red), and between 2 and 3 (black).

components near the time $t = 400$. As can be seen in the middle frame of Figure 5.15, approximately $2M_{\odot}$ of fluid is ejected in the process. The intruder retreats on an eccentric orbit, reaching an apastron separation of more than $200R_{\odot}$ and returning for its next epicentre passage shortly before $t = 1000$. As the intruder moves through the circum-binary envelope and the outer layers of the first merger product, its orbit decays and more mass is ejected. By the time $t = 1400$ when the three-body merger product is formed, more than $20M_{\odot}$ of fluid has been ejected in total.

Another double merger resulting in significant mass loss is summarised in Figure 5.16, which shows the masses and separations relevant to the hydrodynamic calculation of scenario 256. Here the initial merger occurs between the two most massive stars near a time $t = 1800$, with about $1.5M_{\odot}$ of fluid being ejected in the process. The third star is left on a highly eccentric orbit, reaching an apastron separation of more than $600R_{\odot}$ at $t = 4100$, and returning for its next pericentre passage at $t = 7200$. With each passage through the envelope of the first merger product, the orbit of the third star decays and more mass is ejected until ultimately, at $t = 8000$, the three-body merger product is formed.

In scenarios 250 and 261, the impact of the intruder into the primary causes the outer layers of the later to expand and overflow its Roche lobe, resulting ultimately in a stable binary. Figure 5.17 shows masses and sep-

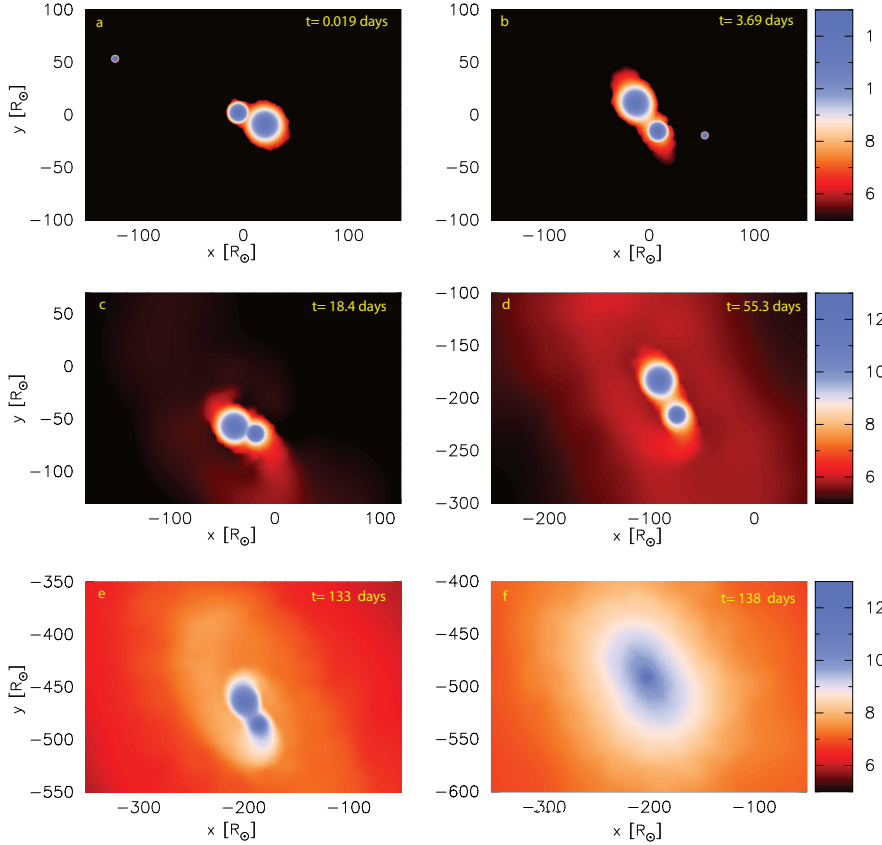


Figure 5.12: Column density along lines of sight perpendicular to the xy plane at various times for the same hydrodynamic calculation of scenario 260.

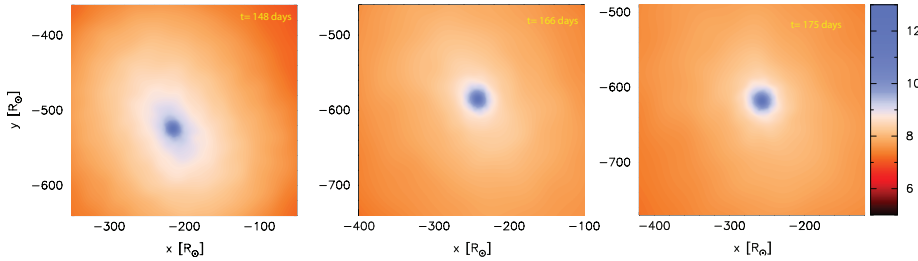


Figure 5.13: Column density along lines of sight perpendicular to the xy plane at various times for the same hydrodynamic calculation of scenario 260. It can be seen that the inner regions of the product become more compact and spherically symmetric, whereas the outer regions increase in size and have elongated shape.

arations of stars for scenario 261, which begins with the three stars in a resonant interaction. At a time $t = 83$, the lowest mass star is absorbed into the largest star. The collision immediately ejects $1M_\odot$ of material and

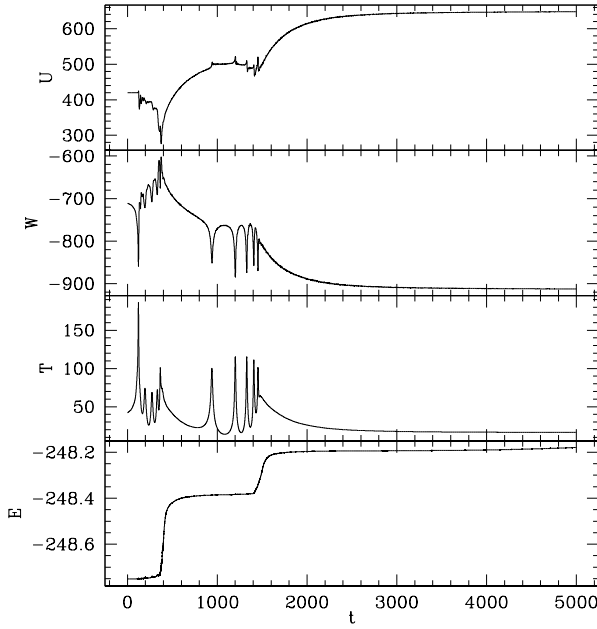


Figure 5.14: Internal energy U , gravitational energy W , kinetic energy T , and total energy E versus time for scenario 298. Peaks in T and associated dips in W correspond to close passes or mergers between the stars. Note that the total energy is conserved to about 0.2% over the interval shown.

leaves the remaining two stars in an eccentric binary ($e \approx 0.4$). A fraction of a solar mass is also placed into a circum-binary envelope: this fluid is not gravitationally bound to either star individually but rather to the remaining binary as a whole. As the binary grinds through the envelope, the orbit gradually circularises, as can be seen by examining the separation curve in the bottom frame of Figure 5.17. By a time $t \approx 6 \times 10^4$, the envelope has been effectively removed and the binary has essentially reached a steady state with an orbital period of 113 time units (50 hours) and a separation of $26R_\odot$. The calculation for this scenario lasted more than 3.3×10^6 iterations and covered a timespan of over 80000 time units (over 4 years physical time). During this calculation, total energy and angular momentum was conserved to better than 0.1%.

Because of the complexity of three-body interactions, most of our simulations are limited to $N \gtrsim 10^4$ particles. Even with this number of particles, a single simulation may take up to a few weeks to complete. To test whether our results are affected by numerical artifacts, we recalculated few of our short-lived simulations in high resolution. We find that in most of the cases the results are weakly dependent on the resolution. In particular, the case of interest is scenario 204 where three single stars are in the middle of the resonant interaction. In Figure 5.18 we display time evolution of energies

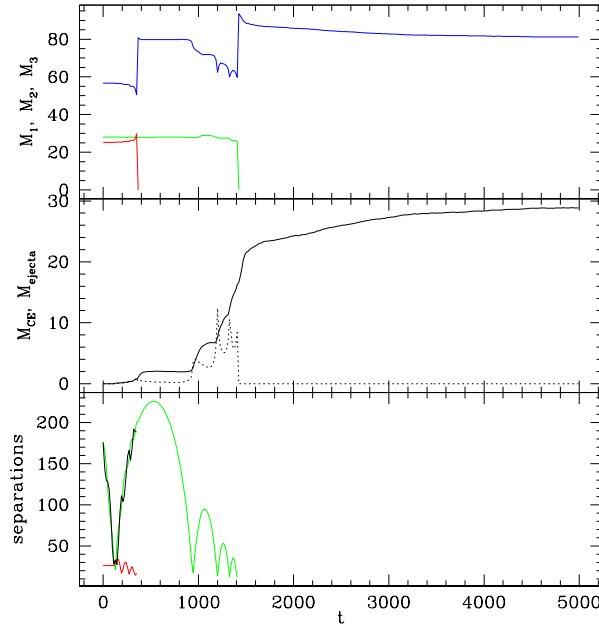


Figure 5.15: Masses and separations versus time for the calculation displayed in Fig. 5.14, scenario 298. The top frame shows the masses of components 1, 2, and 3, represented by blue, green, and red curves, respectively. The middle frame plots the amount of mass ejected (solid curve) and bound in a circumbinary envelope (dotted curve). The bottom curves show the separations between components.

for two resolutions. One may see from the kinetic energy plot that the first close interaction occurs at $t \simeq 75$. The further behaviour of three stars bears characteristics of a resonant interaction with kinetic and gravitational potential energy exhibiting aperiodic oscillations of different magnitudes until $t \simeq 200$. At this time two of the three stars merge together (Table 5.3), and the final evolution of the system is decay of a resulted binary star. In high resolution case (right panel in Figure 5.18), the merger occurs somewhat earlier than in the low resolution case. Since this kind of interaction is of tidal nature, it is a known result that the details at level of trajectories are resolution sensitive (Davies et al., 1993; Freitag & Benz, 2005). However, the final outcome is consistent between two resolution: all three stars eventually merge together. Moreover, mass and energy of the ejected fluid as well as kick velocity of the product differs by at most a factor of two. In Figure 5.19 we show time evolution of masses of three stars, the mass of ejected fluid and the separation between stars. The over results are consistent across these two simulations.

Another case of interest is scenario 299, where a massive binary is being intruded by a massive star. In Figure 5.20 and 5.21 we show the time

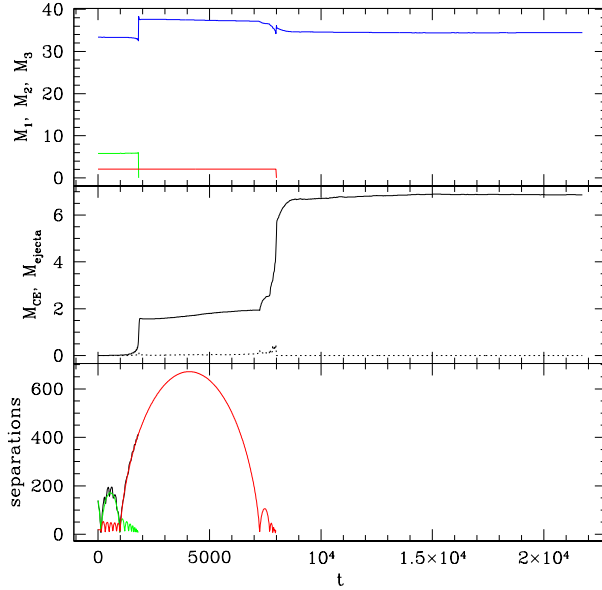


Figure 5.16: Like Fig. 5.15, but for scenario 256.

evolution of energies and global quantities, such as masses of stars, ejecta and stellar separation, respectively. We notice a remarkable agreement between these two simulations. The merger between two of the three stars, intruder and the most massive binary member, occur at $t \simeq 110$, and further binary decay lasts for another 1000 units. Mass, energy of the ejecta and kick velocity of the collision product are consistent between these two runs.

In Figure 5.22, we examine the effects of resolution for four separate simulations of scenario 202 with the number of particles varying by a factor of 15 from the lowest resolution treatment to the highest resolution. The agreement is excellent, with even the lowest resolution simulation capturing all important aspects of the orbital dynamics. The small bump in the kinetic energy T shortly after the time $t = 100$ corresponds to the absorption of the $0.120M_{\odot}$ star into the $57.9M_{\odot}$ star, which excites oscillations in the merger product that are visible in the internal energy U and gravitational potential energy W curves. The merger product is left orbiting the $29.9M_{\odot}$ star in a stable binary with eccentricity $e = 0.583$ and semimajor axis $a = 127R_{\odot}$: the peaks in T and simultaneous dips in W correspond to the periastron passages.

In Figure 5.23 we show the projected trajectories of the three stars in scenario 246 of masses 42.2 , 38.3 and $1.37M_{\odot}$, as calculated by a point-mass integrator (top left frame), by a sticky sphere code (top right frame), and by our hydrodynamics code (bottom four frames) with different resolution. In

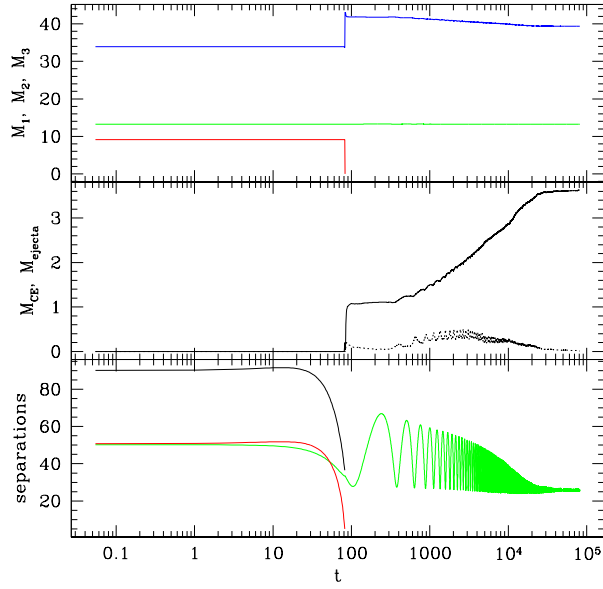


Figure 5.17: Like Fig. 5.15 and Fig. 5.16, but for scenario 261, and with time plotted on a logarithmic scale so that the long term evolution and circularization of the resulting binary can be more easily observed.

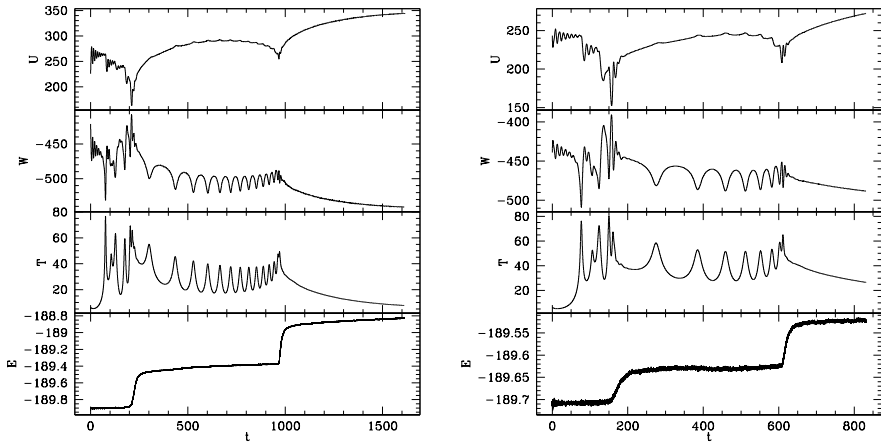


Figure 5.18: Internal energy U , gravitational potential energy W and kinetic energy T versus time t for two simulations of scenario 204 that differ in resolution: $N = 11946$ (left panel) and 60024 (right panel).

all cases, the $1.37M_{\odot}$ intruder approaches the circular binary on a hyperbolic trajectory with eccentricity $e = 1.09$. In the point mass approximation, the intruder reaches a minimum separation of $4.90R_{\odot}$ from the secondary and

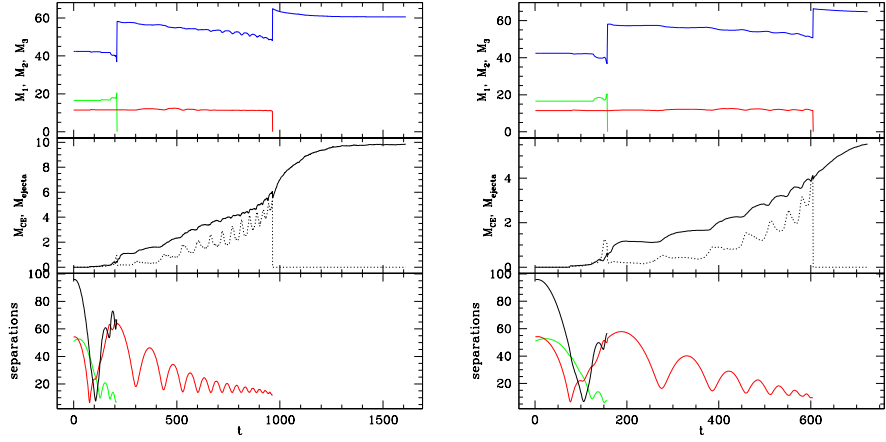


Figure 5.19: Masses and separations versus time for two simulations of scenario 204: $N = 11946$ (left panel) and 60024 (right panel). The top frame shows the masses of components 1, 2, and 3, represented by blue, green, and red curves, respectively. The middle frame plots the amount of mass ejected (solid curve) and bound in a circumbinary envelope (dotted curve). The bottom curves show the separations between components.

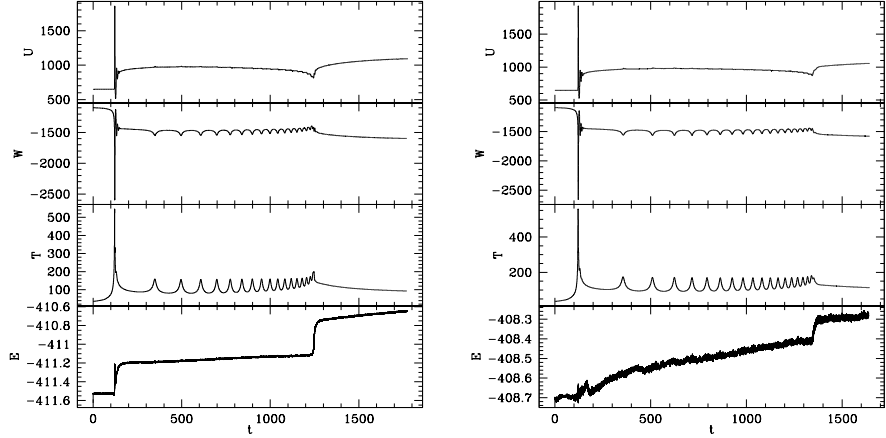


Figure 5.20: Internal energy U , gravitational potential energy W and kinetic energy T versus time t for two simulations of scenario 299 that differ in resolution: $N = 10194$ (left panel) and 102540 (right panel).

then slingshots back outward on a trajectory with eccentricity $e = 1.05$. In the sticky sphere approximation, a merger between the intruder and the secondary of the binary occurs during the initial pericenter passage, followed shortly thereafter by a second merger with the primary.

The scenario plays out qualitatively differently when the hydrodynamics is followed. The intruder again passes to a minimum separation of about

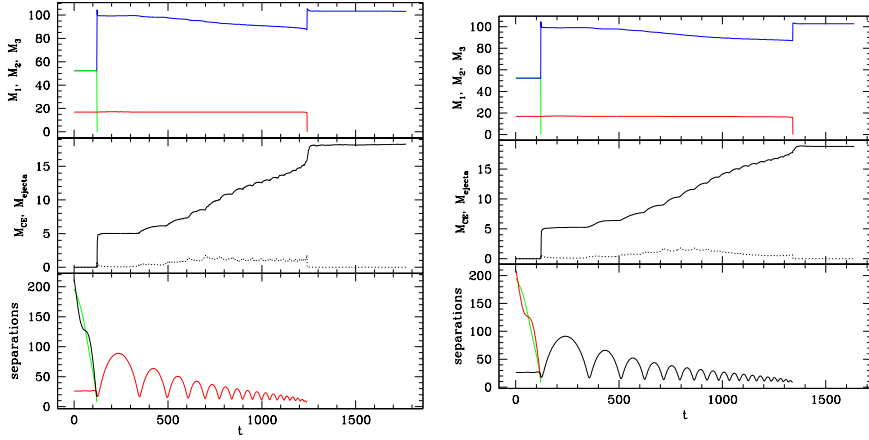


Figure 5.21: Masses and separations versus time for two simulations of scenario 299: $N = 10194$ (left panel) and 102540 (right panel). The top frame shows the masses of components 1, 2, and 3, represented by blue, green, and red curves, respectively. The middle frame plots the amount of mass ejected (solid curve) and bound in a circumbinary envelope (dotted curve). The bottom curves show the separations between components 1 and 2 (green), between 1 and 3 (red), and between 2 and 3 (black).

$5R_\odot$ from the core of the secondary, well within its $11R_\odot$ stellar radius, and then begins to retreat. The impact, however, transfers energy into oscillations of the secondary and the intruder is not moving fast enough to escape further than about $40R_\odot$ from the secondary. Our hydrodynamic calculations show that the intruder makes a second pericenter passage through the secondary, but these calculations then deviate depending on the resolution: the resulting trajectories do not converge as the number of particles is increased up to $N = 84642$ due to the chaotic nature of the orbits.

In the case of our $N = 10554$ calculation of scenario 246, the intruder is shot out to a distance of over $100R_\odot$. Finally, the intruder makes one final pass through the secondary, and is ejected out of the system on a trajectory with eccentricity $e = 1.3$. The removal of orbital energy from the binary triggers a mass transfer instability. The primary canibalizes the secondary and, as the binary merges, $0.06M_\odot$ of material is ejected out to infinity. At this time, the blue and green curves in Figure 5.23 merge into a single blue curve (see the lower right hand corner of the middle left frame).

The $N = 21204$ and 42294 calculations of scenario 246 yield qualitatively similar results. After the third pericenter passage of the intruder through the secondary, the two stars merge. The resulting binary, surrounded by an envelope of gas removed from the secondary by the impacts, ultimately merges. In our highest resolution calculation of this scenario ($N = 84642$), the intruder does not immediately merge with either star in the binary, but

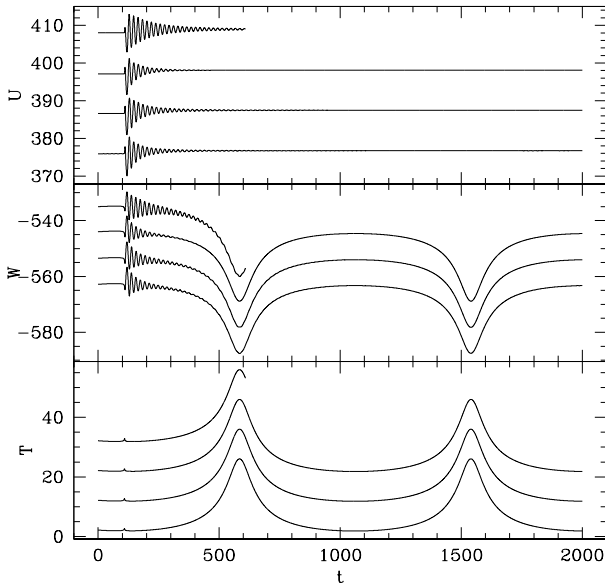


Figure 5.22: Internal energy U , gravitational potential energy W and kinetic energy T versus time t for four simulations of scenario 202 that differ in resolution: $N = 6138$ (bottom curve), 11466 (second from bottom), 22380 (third from bottom), 91956 (top). The energy scale on the left axis corresponds to the low resolution $N = 6138$ case: the other energy curves have been offset by 10, 20, and 30 energy units to facilitate the comparison.

rather the three stars move around one another in a long-lived resonant interaction.

5.6 Discussion and Conclusions

In this work we carried out hydrodynamic simulations of a set consisting of 40 close encounters between three stars, and the initial conditions were taken from realistic N -body simulations. Most of the collisions (31) involve a massive binary star intruded upon by, generally, a lower mass star. The rest of the collisions (9) are between three single stars which are in the middle of the resonant interaction. All the simulations were carried out with both SPH method and sticky sphere approximation.

At bird's view, it appears that sticky sphere method provides a good approximation for the outcome of the encounter, if only initial and final states are of interest. In other words, if the sticky sphere method predicts a merger of all three stars, this is most likely the outcome in more realistic hydrodynamic simulations. However, if one is interested in mass loss, a

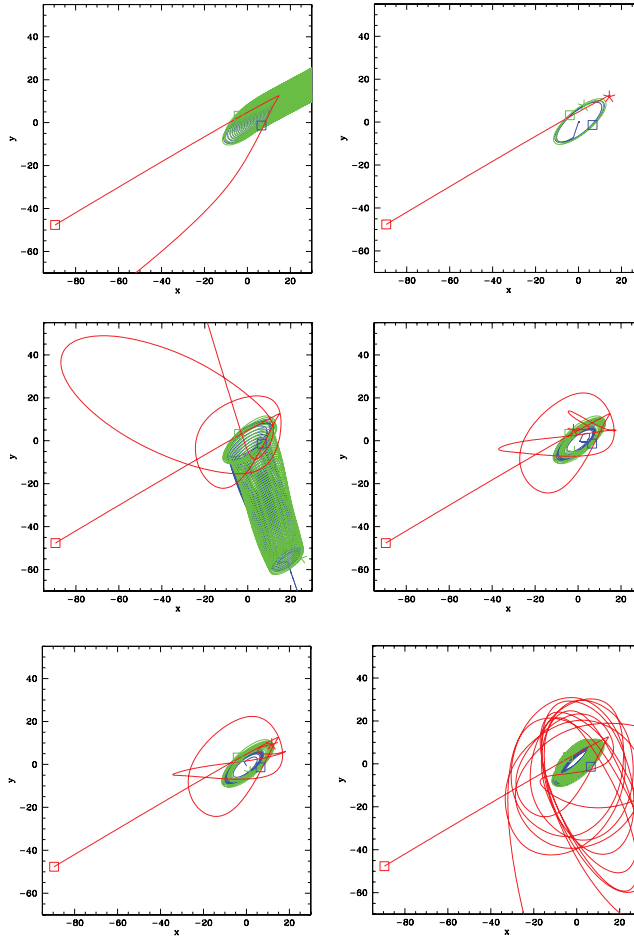


Figure 5.23: Trajectories projected onto the xy plane for scenario 246 as calculated in a pure point mass approximation (top left), in a sticky sphere approximation (top right), by our hydrodynamics code with $N = 10554$ (middle left), with $N = 21204$ (middle right), with $N = 42294$ (bottom left), and with $N = 84642$ (bottom right). We adopt the convention that the trajectory of the most massive star is represented by the blue curve, the intermediate mass star by the green curve, and the lowest mass star by the red curve. The initial conditions are marked by squares, while the final position of an object before it merges with another one is marked by a 5-point asterisk.

close inspection reveals that in some cases a considerable amount of mass is ejected during the collisions, and this only happens in double merger cases. In addition, the collision product acquires kick velocity, which is usually a result of the asymmetric mass ejection. This kick velocity could even be high enough to eject the product out of the core to the outskirts of a star cluster. In three cases (scenario 211 and 262), in which only two

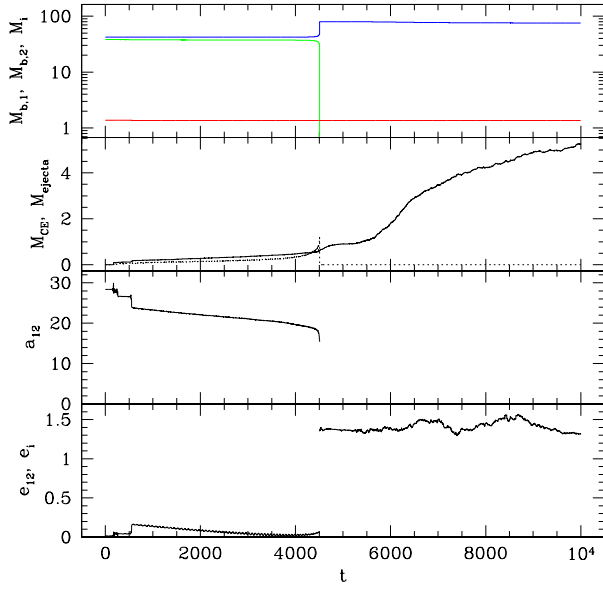


Figure 5.24: Evolution versus time of, from the top of the figure to the bottom, the stellar masses, mass in common envelope (dotted curve) as well as in ejecta (solid curve), semimajor axis a_{12} of the binary, and eccentricity e_{12} of the binary ($t < 4500$) as well as eccentricity e_i of the third star as it departs from the merger product ($t > 4500$) for the $N = 10554$ SPH calculation of scenario 246.

stars merge and the third escapes, the kick velocity is large enough that the collision product can be ejected out of the star cluster. Therefore, it is not completely unreasonable to expect collision products to be observed in the outer regions of a young star cluster, and the Pistol star in the Quintuplet cluster (Figer et al., 1998a) may well be a merger product produced either in a resonant interaction or a binary merger.

The sticky sphere approximation however fails in few cases. On occasions, this approximation predicts a formation of a binary with a merger product as one of the components (scenario 214, 253, 260 and 262). As interesting as it could be from either observational or theoretical point of view, detailed hydrodynamic modelling, however, predicts that complete merger is more likely outcome if the interaction is mild; otherwise, the outcome is two unbound stars, in which one of them is the collision product. In another case, sticky sphere method predicts either one (scenario 207) or two collisions (scenario 222) in a system, but hydrodynamic simulations predict a fly-by. These are the cases where an intruder star is slingshot by a binary. The gain in the orbital kinetic energy of the intruder is large enough to be completely absorbed by tidal interaction, and therefore the intruder

star escapes to infinity. If semi-major axis of the binary is large enough, the merger is avoided and the binary acquires eccentricity.

For those situations in which the sticky sphere algorithm predicts a single merger event, the result is incorrect in almost half of the situations. It is important to keep in mind that the condition for a merger in the sticky sphere approximation is energy independent, and therefore if two stars with large enough velocities will experience a grazing collision, this method will predict complete merger, even though we would not expect one. Nevertheless, the sticky sphere approximation appears to be a valid method to quickly detect collisions in star clusters. There is still however a chance that a collision reported in the sticky sphere method is a false one, but this however could be easily checked by means of hydrodynamic simulations. In the environment with high velocity dispersion, such as galactic nuclei, sticky sphere approximation will most likely fail more often since the velocity dispersion in there is at least an order of magnitude higher than in the cores of young massive star clusters. In such environments, the collision cross-section will be reduced, since grazing interactions between stars may not necessary lead to mergers (Freitag & Benz, 2005). While this could be improved by a more sophisticated effective radius of the merger product (we use simply $R_1 + R_2$), it is unlikely that simple recipes can correctly reproduce the richness of the hydrodynamic results, especially if one is interested in the close interaction between three or more stars.

Stellar collisions in a young dense star cluster are expected to occur in the first few million year of the cluster lifetime. At this age, the star cluster may still be embedded into natal gas (Lada & Lada, 2003), and therefore if ejecta is energetic enough, the state of the gas may be considerably perturbed. If we assume star formation efficiency of about 50%, there is about $10^{49} - 10^{50}$ ergs in gravitational binding energy of gas. From our results, we find that in about half of the cases the energy of the ejected matter exceeds 10^{49} ergs, and in two cases (scenarios 220 and 299) even 10^{50} ergs. Since collisions are expected to occur in the core of a star cluster, it is just a matter of few collisions to significantly perturb and partially expel the natal gas from the central regions. In the case of a runaway merger (Portegies Zwart et al., 2004; Freitag et al., 2006), we expect that the gas will be expelled form the central regions before the end of runaway. Umbreit et al. (2008) has proposed similar mechanism to expel dust from globular clusters by ejecta resulted from stellar collisions.

All of the collisions products resulting from our simulations posses some amount of angular momentum. In some cases, the amount of angular momentum is large enough that the shape of the collision product substantially deviates from spherical symmetry. Evolving such an object is a real challenge for stellar evolution codes, given that even evolution of a non-rotating massive collision product is a formidable task (Glebbeek, 2008). In addition, there still exist problems on even hydrodynamical grounds since some

of our rotating collision products are still gradually losing mass even at the termination of our hydrodynamic calculations. The reason for this mass loss is spurious transport of angular momentum outward caused by the artificial viscosity (Lombardi et al., 1999). The precise timescale of this effect depends on numerical parameters and the treatment of AV. For example, in scenario 220, the progression of the stellar collisions is essentially the same in the N=20178 and N=46296 calculations. In the higher resolution simulation, however, the angular momentum transport and resulting mass loss in the final collision product progresses more slowly. It is worth noting, however, that *physical* angular momentum transport mechanisms, such as stellar winds and magnetic braking, would have a similar qualitative effect but on a longer timescale (Sills et al., 2005).

Acknowledgements

We acknowledge the use of the 3D virtual collaboration environment **Qwaq Forums**, which greatly facilitated the remote collaboration leading to this paper. JCL is supported by the National Science Foundation under Grant No. 0703545, and EG and SPZ are supported by NWO (grants #635.000.303 and #643.200.503). Column density plots in this paper were produced using SPLASH, a publicly available visualization tool for SPH (Price, 2007).

Chapter 6

Mixing in massive stellar mergers

Based on:

E. Gaburov, J. C. Lombardi and S. Portegies Zwart

Monthly Notices of the Royal Astronomical Society, 383L, 5, 2008

ABSTRACT

The early evolution of dense star clusters is possibly dominated by close interactions between stars, and physical collisions between stars may occur quite frequently. Simulating a stellar collision event can be an intensive numerical task, as detailed calculations of this process require hydrodynamic simulations in three dimensions. We present a computationally inexpensive method in which we approximate the merger process, including shock heating, hydrodynamic mixing and mass loss, with a simple algorithm based on conservation laws and a basic qualitative understanding of the hydrodynamics of stellar mergers. The algorithm relies on Archimedes' principle to dictate the distribution of the fluid in the stable equilibrium situation. We calibrate and apply the method to mergers of massive stars, as these are expected to occur in young and dense star clusters. We find that without the effects of microscopic mixing, the temperature and chemical composition profiles in a collision product can become double-valued functions of enclosed mass. Such an unphysical situation is mended by simulating microscopic mixing as a post-collision effect. In this way we find that head-on collisions between stars of the same spectral type result in substantial mixing, while mergers between stars of different spectral type, such as type B and O stars (~ 10 and $\sim 40 M_{\odot}$ respectively), are subject to relatively little hydrodynamic mixing.

6.1 Introduction

The cores of star clusters can become so dense that close encounters and even collisions between stars become quite common (Portegies Zwart et al., 1999). This effect is particularly important in young star clusters where a broad range of stellar masses dominates the dynamical evolution of the cluster core. In a star cluster with an initial half-mass relaxation time smaller than a few tens of million years, core collapse can occur well before the most massive stars leave the main-sequence and explode in a supernova. In such star clusters, these massive stars will dominate the core dynamics. This is most noticeable in both the arrest of core collapse by the formation of tight massive binaries and the occurrence of physical collisions between stars which are mediated by the binaries (Gaburov et al., 2008b).

Simulating stellar collisions in globular clusters has attracted considerable attention over the last decade. These calculations were mainly initiated to explain the presence and characteristics of blue stragglers (Sills et al., 2002; Lombardi et al., 2002a, 1996a). In many cases, collisions occur infrequently enough that the already computationally expensive dynamical modelling of a cluster would hardly be slowed down by a simple treatment of collisions. However, it was recently recognised that the number of collisions in young star clusters can become quite large, and this may lead to formation of a very massive object (Portegies Zwart et al., 2004; Freitag et al., 2006). Furthermore, the subsequent evolution of such objects, and of collision products in general, can depend on their internal structure.

To determine the structure of a collision product accurately, one can resort to high-resolution numerical simulations of stellar mergers. Such simulations are generally carried out by means of the smoothed particle hydrodynamics (SPH) method (Monaghan, 2005). This however becomes computationally expensive, especially if one is interested in multiple collisions which may occur in the course of N -body simulations. On the other hand, components of multiple systems, such as binaries and triples, may experience a collision (Gaburov et al., 2008b), and careful treatment of such collisions might play an important role for further evolution of these multiple systems. Therefore, faster methods are needed to compute the outcome of a stellar merger event, and these methods can eventually be included in N -body simulations.

Lombardi et al. (1996a) constructed a method which has been successfully used for collisions between low-mass main-sequence stars, and in this work we extend this method to collisions between massive stars. Our method has a general applicability, in the sense that it is suitable for mergers of all stellar types, including compact objects.

6.2 Methods

6.2.1 Guiding Principle

The guiding idea of our method is Archimedes' principle. To determine how fluid will redistribute itself when brought out of equilibrium, perhaps by a stellar merger, we need to consider densities: a fluid element with a greater density than its environment will accelerate downward, while one with a smaller density will be buoyed upward. Any such element can ultimately settle into hydrostatic equilibrium once its density equals that of its environment. The density of a fluid element will not in general remain constant during the collision. Instead, it will be continuously adjusted in such a way that pressure equilibrium with the environment is achieved. In other words, parcels of gas expand or contract as necessary to equilibrate their pressure with the environment.

We begin by considering a distribution of gas, in our case stars, and specify distribution functions for the pressure P , density ρ , and abundance of chemical species X_i as a function of the enclosed mass. For a given equation of state, the expression for the entropy can be determined. It is often mathematically simpler, although not formally necessary, to define an entropic variable A which is related to the specific entropy and conserved by fluid elements in adiabatic processes; we call this entropy variable A the buoyancy.

The buoyancy can be calculated from the equation of state, $P = P(A, \rho, X_i)$. In the case of an ideal gas $A = P/\rho^\Gamma$, where Γ is the adiabatic index. By construction, the buoyancy A depends directly upon entropy and composition, and it remains constant for each fluid element in the absence of heating and mixing. Therefore, it is an important starting point for understanding the hydrodynamics of collisions.

This idea has been successfully used to describe the underlying hydrodynamics of collisions among low mass main sequence stars (Lombardi et al., 1996a, 2002a, 2003), which are well described by a monatomic ideal gas equation of state. In this case $\rho = (P/A)^{3/5}$, such that at a given pressure, a smaller A yields a greater value of ρ . Consequently, fluid with smaller values of A sink to the bottom of a potential well, and the A profile of a star in stable hydrostatic equilibrium increases radially outwards. Indeed, it is straightforward to show that the condition $dA/dm > 0$ is equivalent to the usual Ledoux criterion for convective stability of a nonrotating star (Lombardi et al., 1996a).

6.2.2 Sorting method

The fluid in high mass main-sequence stars is well described by a mixture of monatomic ideal gas and radiation in thermal equilibrium. In such cases,

the total pressure is

$$P = \frac{\rho k T}{\mu} + \frac{a T^4}{3}, \quad (6.1)$$

where k is the Boltzmann constant, T is temperature, μ is the mean molecular mass, and a is the radiation constant. The specific entropy is (Clayton, 1983)

$$s - s_0 = \frac{3}{2} \frac{k}{\mu} \left[\log \left(\frac{kT}{\rho^{2/3} \mu} \right) + \frac{8}{3} \frac{1-\beta}{\beta} \right] \equiv \frac{3}{2} \frac{k}{\mu} \log A, \quad (6.2)$$

where the quantity s_0 depends only on composition and β is the ratio of gas to total pressure. To achieve the equality in Eq. 6.2, we define the buoyancy A through the following relation

$$P = \frac{A \rho^{5/3}}{\beta} e^{-\frac{8}{3} \frac{1-\beta}{\beta}}. \quad (6.3)$$

Through manipulations with Eq. 6.1, Eq. 6.2, Eq. 6.3 and definition of β , we find

$$\rho = \frac{3k^4}{A^3 \mu^4 a} \frac{1-\beta}{\beta} e^{8 \frac{1-\beta}{\beta}}. \quad (6.4)$$

Together, Eq. 6.3 and Eq. 6.4 provide the desired relationships between the pressure, buoyancy, density, and composition. Given a prescription for shock heating and an estimate of the mass loss, it is possible to determine the structure of a non-rotating product resulting from a head-on collision of two massive main-sequence stars, which we call parent stars.

To begin with, we consider fluid elements at the centre of each parent star and determine which one will settle in the centre of the collision product. For this purpose, we both make an initial estimate of the central pressure of the collision product and test which fluid element would have larger density when brought to this central pressure: a process that can be completed in two steps. First, as the composition and post-shock buoyancy of each fluid element can be considered known, Eq. 6.3 gives what would be the final β value of each element if it were to settle at the centre of the collision product. Second, these β values correspond to densities through Eq. 6.4. The fluid element with the greater density is the one that actually settles in the centre of the collision product. Next, we integrate the equations of hydrostatic equilibrium to determine the local pressure P throughout the product. This local pressure is used to determine which of subsequent fluid elements from the parent stars contribute to the structure of the product. This procedure is repeated until the mass supply of the parent stars is depleted. As in the case of low-mass main-sequence stellar collisions, the central pressure is iteratively improved until the outer boundary condition, namely that the surface pressure vanishes, is satisfied.

As a consequence of this merging procedure, one must expect that fluid of a certain composition that has originated in one parent star can be located

arbitrarily close to fluid of a different composition from the other parent. These fluid elements must be in pressure equilibrium and also, by the condition of hydrostatic equilibrium, have the same density. Therefore, in order to have adjacent fluid elements of different μ , Eq. 6.3 and Eq. 6.4 imply that these elements must have different buoyancies A . We therefore should not expect that the A and μ profiles in a nascent collision product will be single-valued, at least not before mixing has occurred on the microscopic level.

If the parent stars have essentially the same homogeneous composition as in the merger of two unevolved stars, then μ will be uniform throughout the collision product, and for any given pressure, greater densities will correspond to smaller values of the buoyancy. In other words, the structure of the collision product can then be simply determined by sorting the fluid in order of increasing A : the lowest A fluid is placed at the centre of the product and is surrounded by shells with increasingly higher values of A . The merging procedure also reduces to sorting by A in another special case, namely when radiation pressure is negligible ($\beta \rightarrow 1$), as Eq. 6.3 clearly reduces to the monatomic ideal gas result in this limit. The merging procedure presented here is therefore a natural generalization of that presented for low mass stars in Lombardi et al. (2002a, 2003).

6.2.3 Stability Criterion in High Mass Stars

The unusual profiles that can be achieved in stellar mergers suggest that we take a careful look at the condition for convective stability:

$$\left(\frac{d\rho}{dr} \right)_{\text{env}} < \left(\frac{d\rho}{dr} \right)_{\text{el}}. \quad (6.5)$$

Here, the subscripts “env” and “el” refer to the environment and the fluid element respectively. Since pressure equilibrium between the element and its immediate environment is established nearly instantaneously, the condition for convective stability can be written in the following way:

$$\left(\frac{d \log P}{d \log \rho} \right)_{\text{env}} < \left(\frac{d \log P}{d \log \rho} \right)_{\text{el}}. \quad (6.6)$$

Using Eq. 6.3 and Eq. 6.4, we evaluate derivatives on both sides of Eq. 6.6. We then note that

$$\Gamma_1 = \frac{-3\beta^2 - 24\beta + 32}{24 - 21\beta} = \frac{5}{3} - \frac{3\beta^2 - 11\beta + 8}{24 - 21\beta}, \quad (6.7)$$

and this allows us to write the stability condition in the following form

$$\frac{3\Gamma_1 - 4}{4} \left(\frac{d \log A}{d \log \rho} \right)_{\text{env}} < \frac{5 - 3\Gamma_1}{3} \left(\frac{d \log \mu}{d \log \rho} \right)_{\text{env}}. \quad (6.8)$$

Model	M_1	M_2	Evolutionary State	N
T88, H88	80	8	TAMS, HAMS	880k
T48, H48	40	8	TAMS, HAMS	480k
T28, H28, Z28	20	8	TAMS, HAMS, ZAMS	280k
T18, H18, Z18	10	8	TAMS, HAMS, ZAMS	180k

Table 6.1: The simulations carried out in this work. The model name of the simulations are given in the first column. The masses of the primary and the secondary stars are shown in the second and the third column respectively. The evolutionary state of the parent stars is given in the fourth column: TAMS, HAMS, and ZAMS stand for turn-off age, half-age, and zero-age main-sequence respectively. In the fifth column we show the number of SPH particles in the simulations; in all cases, we use well over 100k equal mass SPH particles in order to achieve high resolution in the dense stellar interiors and to insure convergent results.

As the $d \log \rho / d \log m$ is always negative throughout the star, we can rewrite the stability condition in a more convenient form:

$$\left(\frac{d \log A}{d \log m} \right)_{\text{env}} > \frac{4 \frac{5}{3} - \Gamma_1}{3 \Gamma_1 - \frac{4}{3}} \left(\frac{d \log \mu}{d \log m} \right)_{\text{env}}. \quad (6.9)$$

In a star in which Eq. 6.9 is satisfied, a perturbed element will experience restoring forces that cause it to oscillate around its equilibrium position. It can be seen that in the limit of ideal gas ($\Gamma_1 = 5/3$), or when the composition is uniform, we recover the usual stability criteria $dA/dm > 0$. In the general case, however, A will typically increase outward, but can decrease in regions with an inverted composition gradient.

6.3 Validation

6.3.1 Initial conditions

In the previous section we have presented a sorting algorithm that generates a collision product in hydrostatic equilibrium. As the method deals with non-rotating products, we validate it by carrying out simulations of head-on collisions between main-sequence stars of different mass and age. The full set of simulations is presented in Tab. 6.1.

Simulations of stellar collisions were carried out by means of a modified version of the GADGET2 code (Springel, 2005). In particular, we included radiation pressure in the equation of state and the functionality which allows generation of relaxed models of parent stars in quasi-hydrostatic equilibrium (Lombardi et al., 2006; Turner et al., 1995).

We have prepared three-dimensional SPH stellar models from one-dimensional stellar models computed with the EZ stellar evolution code (Paxton, 2004).

In particular, we have used EZ to evolve a non-rotating zero age main-sequence (ZAMS) model with a primordial helium abundance $Y \simeq 0.3$ and metallicity $Z = 0.02$. The resulting star is composed of spherical mass-shells which store necessary stellar data, such as local composition, temperature, and density, as well as enclosed stellar mass and radius. The stars are evolved until the primary star reaches its half-age of its main-sequence lifetime (HAMS) or until the primary has only 1% hydrogen abundance in its core (TAMS). In all cases the secondary star is evolved to the same age as the primary with which it collides.

6.3.2 Results

We have shown in Sect. 6.2 that the two main quantities which determine the structure of the collision product is buoyancy and composition. Since in main-sequence stars the mean molecular mass is mostly dependent on hydrogen mass fraction, we present in Fig. 6.1 buoyancy and hydrogen mass fraction profiles for a selection of the parent stars. In the case of TAMS stars, the primary consumed nearly all of hydrogen in its core. Nevertheless, the secondary has consumed less than the half of its initial hydrogen supply. HAMS parents, on the other hand, are barely evolved; all of the parent models have burnt less than the half of the initial amount of hydrogen in their cores.

The buoyancy of the parent stars is shown in the two lowest panels of Fig. 6.1. Even though the $20M_{\odot}$ and $40M_{\odot}$ stars are at the end of the main-sequence, the buoyancy in their cores is noticeably higher than that of the secondary star. Therefore, based on the results of Sect. 6.2, it is natural to expect that the $8M_{\odot}$ star will occupy the centre of the merger product. In the case of the $10M_{\odot}$ primary, however, one may expect mixing, since the buoyancy of the primary and the secondary stars differ by less than a factor of two, and this difference can be modified by shock heating.

In this work, we model shock heating by increasing the buoyancy of each fluid element. For this we need to assume a particular distribution of shock heating. Motivated by the results of Lombardi et al. (2002a), we adopt the following simple distribution:

$$\log(A_f/A_i) = a + b \cdot \log(P_i/P_{c,i}). \quad (6.10)$$

Here, A_i and A_f are the initial and the final buoyancy of a fluid element, respectively, P_i is the initial pressure, and $P_{c,i}$ is the central pressure of a parent stars from which the fluid has come. We compute parameters a and b by fitting Eq. 6.10 to the simulation data.

One of the advantages of using Eq. 6.10 can be seen by looking at Eq. 6.3. As an SPH particle preserves its composition in the course of a simulation, Eq. 6.10 describes the change in entropy due to the shock heating process. This, in turn, potentially expands the range of applicability

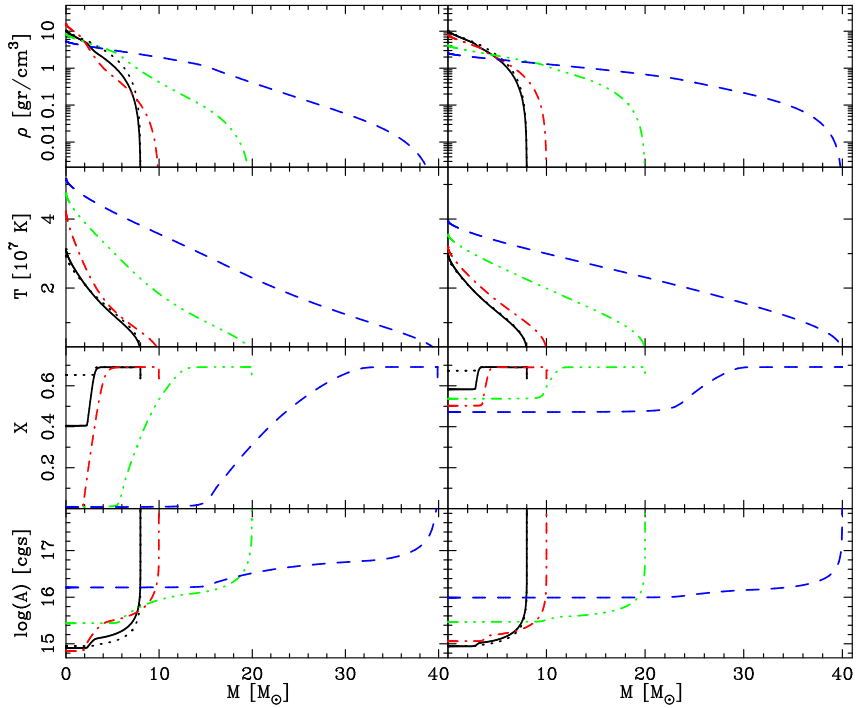


Figure 6.1: Internal structure of a selection of TAMS (left side) and HAMS (right side) parent stars which were used in simulations. The upper panels show density profile as a function of enclosed mass. The black solid and dotted lines on the left side show density profile of the $8M_{\odot}$ star from T18 and T48 models respectively, while on the right side the $8M_{\odot}$ star is taken from H18 and H48 models. The red dash-dotted, green dash-dot-dot-dot and blue dashed lines show density profiles of $10M_{\odot}$, $20M_{\odot}$, and $40M_{\odot}$, stars respectively. The second panels from the top show temperature profiles, while the third and fourth panels present hydrogen mass fraction and buoyancy profiles respectively.

of the sorting algorithm presented in Sect. 6.2 to an arbitrary equation of state, such as of degenerate matter inside white dwarfs.

For every simulation from Tab. 6.1, we obtain a and b values in Eq. 6.10 for each of the parent stars. We use this equation to compute the change in the buoyancy for each of the mass shells of the parent stars, and then we apply the sorting algorithm to generate the structure of the collision product which we compare with the simulation results.

In Fig. 6.2 we present the results of the sorting algorithm and simulations. The sorting algorithm is able to reproduce two distinct branches in temperature, composition and buoyancy for TAMS collisions; the density, on the other hand, is single valued as one would naturally expect. In the case of HAMS collisions, the branches are less pronounced, as expected, because the parent stars have roughly the same composition (see Fig. 6.1).

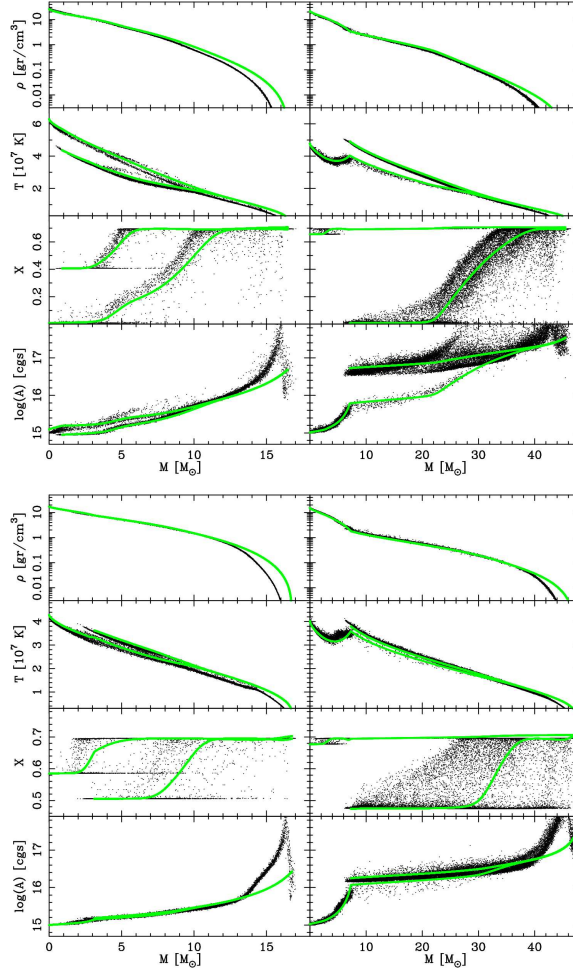


Figure 6.2: The non-mixed structure of the collision products from a selection of simulations. The top set of panels displays results for TAMS collisions, whereas the bottom set displays the same data for HAMS collisions. The black dots are the results of simulations, while the green circles are the results of the sorting algorithm. The upper panels show the density profile as a function of enclosed mass for T18, T48, H18 and H48 simulation models from left to right respectively. In the second panels from the top, we show the temperature profile, and in the third and the fourth panels, we show the hydrogen mass fraction and buoyancy profiles respectively.

A noticeable discrepancy in the density of the outer layers is caused by an inadequate representation of shock heating in these layers by Eq. 6.10; indeed, both the density and buoyancy of our simple model diverge from the SPH results at about the same enclosed mass. The mass loss in the collisions from Tab. 6.1 never exceeds 10%: T18(8.3%), T28(8.9%), T48(5.0%),

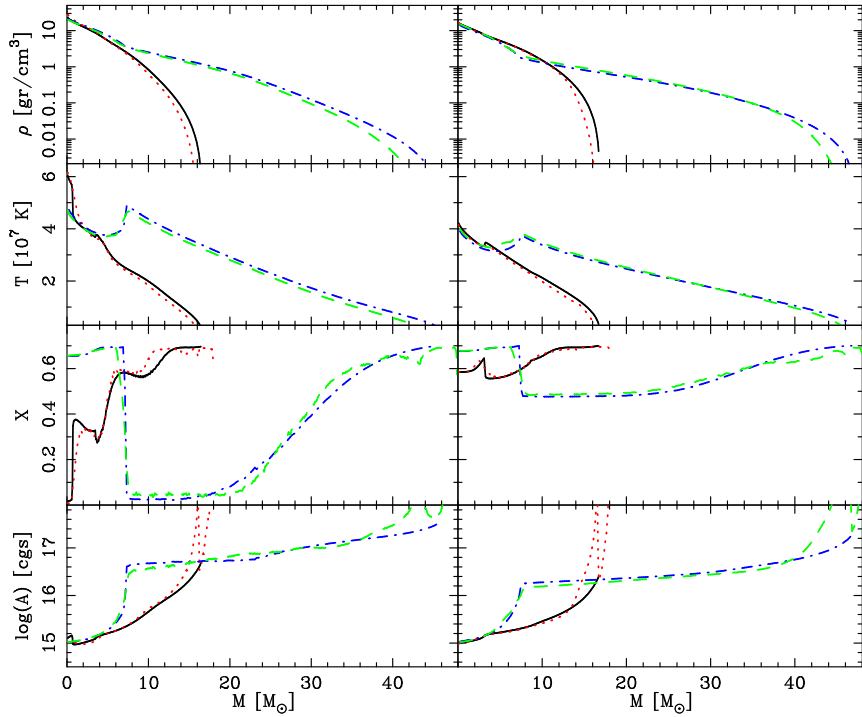


Figure 6.3: The structure of the mixed collision products from the same selection of models as presented in Fig. 6.2. Here, the black solid and red dotted lines show the results of the sorting algorithm and of the simulation respectively for the cases T18 on the left side and H18 on the right side. The blue dash-dotted and green dashed lines show the results of sorting algorithm and of the simulation respectively for the cases T48 on the left side and H48 on the right side. The upper panels show density profiles as a function of enclosed mass, and the second panel from the top shows temperature profiles. The third and the fourth panels from the top show hydrogen mass fraction and buoyancy profiles respectively.

T88(1.9%), H18(6.8%), H28(4.7%), H48(2.1%), H88(0.8%), Z18(6.4%) and Z28(4.5%). As we expect, mass loss is less in collisions involving stars of significantly different mass, as less kinetic energy is redirected into the ejecta. In addition, we observe that mass loss is larger in collisions with evolved stars, due to their weakly bound envelopes.

We note that the very existence of two branches in the results of Fig. 6.2 means that the buoyancy A *does not* increase outward at all locations. In the case of model T18, it is actually the higher buoyancy branch, corresponding to hydrogen depleted fluid from the TAMS primary, which extends into the core of the merger product. Such a configuration is stable only because it is accompanied by a sufficiently steep gradient in composition. Indeed, in model H18, the parent stars are too young to yield large gradients in com-

position, and consequently it is the lower buoyancy fluid from the secondary that sinks to the centre of the merger product. It is also worth noting that in models Z18 and Z28, in which the ZAMS parent stars have uniform composition, we find that the buoyancy increases outwards throughout the collision products, as expected from Eq. 6.9.

As we increase the resolution of parent stars as treated by the sorting algorithm, adjacent mass shells in different branches become increasingly closely spaced. The resulting large gradients will eventually be smoothed by the microscopic mixing between neighbouring fluid elements. To simulate such mixing, we process the results from the sorting algorithm into equal-mass bins, such that each bin accommodates a sufficiently large number of mass shells. We then average the stellar data, such that the total volume and thermal energy of each bin, as well as the total mass of each of the chemical elements, are conserved. From the average values of density, thermal energy and composition, we compute the rest of the thermodynamic quantities, such as temperature. We find that this procedure converges once the high resolution model has roughly 10^5 mass shells averaged into 200 bins. The simulation data is averaged in the same way.

In Fig. 6.3 we show the results of the mixing applied to the models shown in Fig. 6.2. Whereas no significant mixing occurs in models T48 and H48 as the $8M_\odot$ star settled in the centre of the primary, the interior of the collision product in model T18 is mixed. In model H18, however, only the core of the secondary star settles in the centre of the primary star; the rest of the fluid is mixed. The resulting buoyancy increases outwards throughout the product in all models, except in the very centre of T18. Here, the decrease in buoyancy at $\simeq 0.8M_\odot$ is accompanied by an increase in mean molecular mass in such a way that Eq. 6.9 is satisfied.

6.4 Discussion and conclusions

We have presented a new sorting algorithm which generates the structure of collision products in hydrostatic equilibrium. We have tested the algorithm by carrying out a set of SPH simulations of head-on stellar collisions between massive main-sequence stars of different masses and ages. By calibrating the shock heating with the simulation data, we have been able to quickly generate the structure of the collision products consistent with the results of the simulations.

It takes less than a minute to generate a collision product for any of the models presented in Tab. 6.1, whereas an SPH simulations takes at least a day of CPU time on the same computer. Such a speed-up will help to make it possible to include realistic stellar collisions in simulations of star clusters.

We have found that the chemical composition and temperature can be a multivalued function of the enclosed mass, if microscopic mixing processes

are ignored. This is exhibited by the fact that the neighbouring mass shells have a discontinuously changing temperature and chemical composition, whereas the density and pressure remains continuous. Using the sorting algorithm, we have found that the situation is unaffected by increasing the number of shells. Instead, the chemical composition and temperature become double-valued in the continuous limit. Such an obviously unphysical situation is mended by microscopic mixing. We have simulated the mixing process by conservatively averaging multiple mass shells into a single mass bin. The resulted profiles are both single valued and consistent with the simulation data.

We have found significant mixing in only the T18 and H18 models. The reason for this is that buoyancy in the core of the primary and the secondary stars are similar, whereas for the other models, such as T48 and H48, the buoyancy of the primary stars is substantially larger than that of the secondary stars. Therefore, in those cases, fluid from the secondary star occupies the central region of the collision product without being mixed with the fluid from the primary star. We therefore conclude, that hydrodynamic mixing in collisions between main-sequence stars occurs only when the masses and ages of the parents stars are similar to each other. We find that mixing already becomes unimportant at the mass ratio $q \simeq 0.4$, which is the mass ratio of models T28, H28 and Z28. In such cases, the secondary star simply occupies the centre of the collision product without much mixing (Dale & Davies, 2006; Suzuki et al., 2007b).

Microscopic mixing may play an important role during the collision process itself. If the diffusion processes are ignored, the turbulent motion of the fluid can result in a discontinuous distribution of chemical composition and temperature, while maintaining continuity in density and pressure. Such a distribution is susceptible to microscopic mixing which tends to smooth the discontinuities (Dimotakis, 2005). If the timescale of microscopic mixing is larger than the time a collision product takes to settle into quasi-hydrostatic equilibrium, the mixing can be ignored during the collision event and applied only as a post-collision process. On the other hand, if the timescale of the microscopic mixing is shorter than the timescale of a collision event, then one must include the effects of mixing into the simulation itself.

The sorting algorithm can in principle be applied to any type of stars; for example, it is possible to apply it to the merger of white dwarfs. The basic requirement is simply to have the equation of state which gives the relationship between pressure, density, composition, and specific entropy (or buoyancy), analogous to Eqs. 6.3 and 6.4. While it is also necessary to determine mass loss and shock heating of the fluid, these can be estimated through energy conservation arguments.

Acknowledgements

We thank Alexander Brown, Evert Glebbeek, and Ujwal Kharel for useful discussions. We also acknowledge the use of the 3D virtual collaboration environment **Qwaq Forums**, which greatly sped up the remote collaboration leading to this paper. The calculation for this work have been carried out on LISA cluster, which is hosted by SARA supercomputing centre. JCL is supported by the National Science Foundation under Grant No. 0703545, and EG and SPZ are supported by NWO (grants #635.000.303 and #643.200.503). This project has been started during the Modest-7f workshop, which was hosted by the University of Amsterdam and supported by NOVA, NWO, LKBF and ASTROSIM grants.

Chapter 7

The evolution of runaway stellar collision products

Based on:

E. Glebbeek, E. Gaburov, S. de Mink, O. Pols and S. Portegies Zwart
Astronomy & Astrophysics, submitted

ABSTRACT

In the cores of young dense star clusters repeated stellar collisions involving the same object can occur, which has been suggested to lead to the formation of an intermediate-mass black hole. In order to verify this scenario we compute the detailed evolution of the merger remnant of three sequences. We follow the evolution until the onset of carbon burning and estimate the final remnant mass to determine the ultimate fate of a runaway merger sequence.

We use a detailed stellar evolution code to follow the evolution of the collision product between collisions. At each collision, we mix the two colliding stars, taking account of mass loss from the collision. During the stellar evolution we apply mass loss rates from the literature, as appropriate for the evolutionary stage of the merger remnant. We compute models for high ($Z = 0.02$) and low ($Z = 0.001$) metallicity to quantify metallicity effects.

We find that the merger remnant becomes a Wolf-Rayet star before the end of core hydrogen burning. Mass loss from stellar winds dominates over the mass increase due to repeated mergers for all three merger sequences that we consider. In none of our high metallicity models an intermediate-mass black hole is formed, instead they end their lives as $10\text{--}14 M_{\odot}$ black holes. For low metallicity we expect the final remnant of the merger sequence to explode as a pair creation supernova. We find that our metal-rich models become inflated as a result of developing an extended low-density envelope. This may increase the probability of further collisions, but self-consistent N -body calculations with detailed evolution of runaway mergers are required to verify this.

7.1 Introduction

The usual mode of star formation leads to a spectrum of masses between the theoretical hydrogen burning limit and some upper limit, which appears to be close to about $100 M_{\odot}$ (Elmegreen, 1999; Weidner & Kroupa, 2004; Figer, 2005). In young and dense star clusters more massive stars can form when two or more high-mass stars coalesce. The cluster environment helps in driving these stars together. If this happens in sufficiently young and dense star cluster the same star may experience multiple collisions in what is named a ‘collisional runaway’ (Portegies Zwart et al., 1999). During such a chain collision several stars collide in short succession. The trigger for a chain collision is the gravothermal collapse (Bettwieser & Sugimoto, 1984) of the core of a young and dense star cluster. If cluster core collapse is initiated before the most massive stars leave the main sequence the collision runaway sets in (Portegies Zwart & McMillan, 2002) and continues until the target star leaves the main sequence (Portegies Zwart et al., 1999).

If the star explodes as a supernova, this supernova is likely to be unusually bright and rich in hydrogen (Portegies Zwart & van den Heuvel, 2007). The star may also collapse completely into a black hole, without a visible supernova. The black hole remnant of such a star may be considerably more massive than hitherto observed (Portegies Zwart et al., 2004), though less massive than the supermassive black holes found in the nuclei of large galaxies (Kormendy & Richstone, 1995). Various groups have now confirmed the evolution of such collision runaways, and conjecture that the final merger product collapses to a black hole of up to about $10^3 M_{\odot}$ (Portegies Zwart et al., 1999, 2004; Freitag et al., 2006; Gürkan et al., 2006).

Two of our aims in understanding merger runaways are understanding the structure of the merger remnant and the influence of stellar evolution of the merger runaway. Stellar evolution of very massive stars (with masses above $150 M_{\odot}$) has recently been studied by Belkus et al. (2007), Yungelson et al. (2008) and Langer et al. (2007). These studies all seem to come to the same conclusion: at high metallicity mass loss is copious enough to prevent the formation of a black hole of more than $50 M_{\odot}$, which is much lower than the conjectured intermediate-mass black hole mass. These studies, however, either used approximate formulae for stellar evolution (Belkus et al., 2007) or studied the evolution of very massive stars from the zero-age main sequence with an initially homogeneous composition (Yungelson et al., 2008; Langer et al., 2007). According to the dynamical simulations the massive star grows in mass by means of repeated collisions with less massive stars. The consequences of the collisions, the evolution between collisions and the differences in stellar age and structure at the moment of collision are not considered by these studies. A first attempt to overcome these problems by calculating collisions between massive stars and computing the evolution of these merged objects did not result in very different conclusions (Suzuki et al., 2007c). Ide-

ally, one would like to perform a fully self-consistent simulation in which the stellar dynamics, the hydrodynamics of the stellar collisions and the further evolution of the collision products are taken into account self consistently. Such multiscale simulations, however, will have to await the development of the appropriate numerical methodology. The MUSE software environment may provide the necessary functionality for such simulations¹.

In this work we investigate the evolution of three massive stellar collision runaways with a detailed stellar evolution code. The template simulations we chose are three of the sequences published in Portegies Zwart et al. (2004). Each of the stars in the collision sequence are evolved up to the moment they collide using a stellar evolution code (described in §7.2.2) and each merger is resolved as described in §7.2.1. These hydrodynamical events result in a composition and structure of the collision product, of which the evolution is continued. We follow the evolution of the merger product until the evolution code fails to converge or until the onset of carbon burning, applying mass loss rates from the literature. We estimate the final mass of the merger and estimate the mass of the remnant of such a merger event. We also provide the chemical yields that result from such a merger sequence and compare them to the combined yields of a population of normal single stars. Finally we comment on the effect of the initial composition, especially the heavy element content Z (metallicity) on the structure of the merger remnant.

7.2 Methods

7.2.1 Stellar collisions

We use two different methods to model stellar collisions. The first assumes that the collision product is in hydrostatic and thermal equilibrium and mixed homogeneously. The second method uses the prescription of Gaburov et al. (2008) to model the structure of the remnant. In this case the collision product is not homogeneously mixed and it is not in thermal equilibrium (although it is still in hydrostatic equilibrium).

All collisions are treated as head-on collisions with vanishing velocity at infinity (*i.e.*, parabolic collisions). We ignore rotation in this work despite the fact that rotation can have a significant influence on the evolution of a massive star (Maeder & Meynet, 2000b).

Homogeneous mixing

In this approach, detailed models of the progenitor stars were merged and homogeneously mixed at each step of the sequence. We assume that the merger remnant is in hydrostatic and thermal equilibrium. The mass loss from the collision is estimated according to Gaburov et al. (2008).

¹see <http://muse.li>.

In general, homogeneous mixing is not a good approximation for the structure of a merger remnant (Lombardi et al., 1996b; Gaburov et al., 2008; Glebbeek et al., 2008; Gaburov et al., 2008). However, Suzuki et al. (2007c) find that their collision products are almost completely mixed due to mixing processes during stellar evolution. Similarly, we find (§7.3.1) that the central convection zone in our merger remnants encompasses most ($\gtrsim 90\%$) of the stellar mass. Rotational mixing, which we have ignored, will result in even more extended mixing of the collision product, so homogeneous mixing is a reasonable approximation in this case.

Detailed merger models

Our detailed merger models were calculated using the Make Me A Massive Star (MMAMS) code by Gaburov et al. (2008). The code has a prescription for the mass lost from the collision that is based on the results of smooth particle hydrodynamics calculations. Heating due to the dissipation of the kinetic energy of the progenitor stars in shocks and tides is also taken into account. After the ejected mass has been removed and heating has been applied to the material from the parent stars the structure of the collision remnant is determined by searching for a configuration that is dynamically stable (*i.e.* satisfies the Ledoux stability criterion, Kippenhahn & Weigert, 1990). An algorithm for doing this was first developed by Lombardi et al. (2002b) for low-mass stars, for which it is sufficient to sort the mass shells in order of increasing entropy and then integrate the equation of hydrostatic equilibrium. This algorithm is referred to in the literature as *entropy sorting*. For massive stars where radiation pressure is important this does not necessarily produce a stable configuration and some mass shells need to be moved again after the equation of hydrostatic equilibrium has been integrated. This is repeated until a stable model is converged upon.

The output model is imported into the stellar evolution code using the method described in Glebbeek et al. (2008) and evolved until the time of the next collision.

Due to heating during the collision the merger product is not in thermal equilibrium. The excess of internal heat is radiated away during the contraction of the star to the main sequence. Because the stars were out of thermal equilibrium, we encountered more numerical problems when importing the stellar models than we did for the homogeneously mixed models, so that we could only follow one of the merger sequences until the seventh collision.

7.2.2 Stellar evolution

Our stellar evolution code is a version of the STARS code originally developed by Eggleton (1971b) and later updated by others (*e.g.* Pols et al., 1995). This version of the code uses the opacities from Iglesias & Rogers (1996) that

take into account enhancement of C and O, as described in Eldridge & Tout (2004) and Ferguson et al. (2005). The assumed heavy-element composition is scaled to solar abundances (Anders & Grevesse, 1989). Chemical mixing due to convection (Böhm-Vitense, 1958; Eggleton, 1972) and thermohaline mixing (Kippenhahn et al., 1980; Stancliffe et al., 2007) is taken into account. Note that thermohaline mixing is not important in these very massive stars, since most of the star is convective.

STARS uses an adaptive mesh in which the mesh points automatically redistribute themselves according to a mesh spacing function that places more meshpoints in regions of the star where a higher resolution is required. This allows us to calculate the structure of the star with a fairly small number of mesh points. For the models presented here we used 200 mesh points for the main sequence phase and 500 for the core helium-burning evolution. Because our stars form an extended low-density envelope (see §7.3.1) we have found it necessary to increase the number of mesh points in the outer layers compared to our standard stellar models.

We use a mass fraction of heavy elements $Z = 0.02$ for our standard runs. In order to study the effect of metallicity we have also recalculated one of our sequences with $Z = 0.001$. This affects the mass-loss rate and therefore the mass of the progenitors at each collision. We terminate the evolution at central carbon ignition and estimate the final remnant mass according to Belczynski et al. (2002).

7.2.3 Mass loss

Since our collision products become very massive and luminous, even exceeding the Humphreys-Davidson limit (a luminosity cutoff above which few stars are observed, Humphreys & Davidson, 1979), mass loss plays a key role in their evolution. Unfortunately, neither observations nor theoretical models of mass loss exists for the full range of masses and luminosities reached by our models. We have considered three possible mass-loss prescriptions: the empirical rate from de Jager et al. (1988) and theoretical rates from Vink et al. (2000, 2001) and Kudritzki (2002). None of these rates cover the range of parameters of our models well. The empirical de Jager rate has too few data points for luminosities above the Humphreys-Davidson limit. Their 20 point Chebyshev fit needs to be extended beyond $\log L/L_\odot = 6.7$. The theoretical rate from Kudritzki needs to be extrapolated for $T_{\text{eff}} < 40\,000\text{K}$ while the models for the Vink rate are calculated for $\log L/L_\odot < 6.25$ and $50\,000\text{K} \lesssim T_{\text{eff}} \lesssim 10\,000\text{K}$.

We have made some trial calculations using these three mass loss prescriptions to decide which rate we should adopt for our calculations. The results of our trial calculations were qualitatively similar and independent of the mass-loss recipe used. For our quantitative analysis we have adopted the Vink et al. (2001) rate because of the three rates mentioned it best cov-

ers the range of effective temperatures for our models and only needs to be extrapolated in luminosity. By contrast, the Kudritzki (2002) rate needs to be extrapolated to lower effective temperatures, which is less reliable than extrapolating to higher luminosities because the presence of spectral lines that drive the wind depends sensitively on the temperature. In the region where the Kudritzki (2002) rate is valid it is very similar to our extrapolated Vink et al. (2001) rate. Note that our adopted mass-loss rate likely underestimates the true mass loss rate since our stars are much closer to their Eddington limit than the model calculations on which the Vink rate is based. We will return to this point in the discussion. The Vink rate is not applicable to red supergiants and predicts a mass loss rate that is too low for cool stars. For this reason we adopt the de Jager rate rather than the Vink rate at effective temperatures below 10 000K. Our models only reach this temperature for luminosities that are within the validity range of the de Jager rate.

All our models become helium-rich and evolve into Wolf-Rayet stars. We follow the criterion used by Eldridge & Vink (2006) to decide when our stars become Wolf-Rayet (WR) stars. Specifically, we start applying the mass-loss rate from Nugis & Lamers (2000) when the surface abundance of hydrogen drops below 40% by mass and $T_{\text{eff}} > 10\,000\text{K}$. This happens *before* the star finishes core hydrogen burning (compare Langer et al., 2007; Yungelson et al., 2008). For our low metallicity run we used the metallicity scaling found by Vink & de Koter (2005) for the WR mass-loss rate. The Vink et al. (2001) rate already includes metallicity scaling.

7.2.4 Rotation

It has been shown that for off-axis collisions the angular momentum of the collision product can be so large that it cannot reach thermal equilibrium before losing a large fraction of its angular momentum (Lombardi et al., 1996b; Sills et al., 1997). We may therefore underestimate mass loss from the collision. The mechanism for this angular momentum loss is unclear but it has been suggested that magnetic fields can play a key role (Leonard & Livio, 1995; Sills et al., 2005). Rapid rotation can also enhance the mass-loss rate of a star, especially close to the Eddington limit (Maeder & Meynet, 2000a). This increases the uncertainty in the mass-loss rate.

Rotation also influences the star through various instabilities that can induce mixing (Endal & Sofia, 1976; Pinsonneault et al., 1989; Heger et al., 2000). This mixing is important because it can bring helium to the surface, affecting the opacity of the envelope and increasing the luminosity and effective temperature of the star. As mentioned above, rotational mixing is not expected to alter the outcome of our calculations very strongly because our collision products are close to being fully convective.

N	t	$M_{1,N\text{body}}$	$M_{1,\text{mix}}$	$M_{1,\text{MMS}}$	M_2	M_{remnant}
1	0.22577	92.4	90.9	90.9	79.4	154.3
2	0.22782	171.8	154.3	152.8	85.3	217.1
3	0.23702	257.1	216.7	213.6	7.7	223.3
4	0.31217	264.8	219.8	215.3	77.8	274.4
5	0.40122	342.6	268.2	261.6	13.8	279.7
6	0.43480	356.4	277.2	268.0	71.9	327.1
7	0.43480	428.3	327.1	315.1	79.4	382.2
8	0.74123	507.7	348.2		30.1	371.8
9	0.83549	537.7	360.2		66.7	406.7
10	0.90575	604.5	397.3		1.2	398.5
11	1.29919	605.7	353.5		98.2	415.2
12	1.33450	703.9	411.0		24.2	430.8
13	1.42468	728.0	417.6		8.9	425.7
14	1.50261	736.9	409.0		2.2	411.2
15	1.60190	739.1	216.7		60.2	256.5
16	1.63186	799.4	221.0		9.2	228.9
17	1.68112	808.5	186.0		81.1	237.1
18	1.75684	889.6	177.3		40.9	205.5
19	1.90688	930.5	193.6		31.6	216.3
20	2.07245	961.9	129.9		2.6	132.2
21	2.59778	963.1	47.6		55.2	88.6
22	3.10786	1012.7	40.9		75.4 ^a	110.1
	3.72835	1118.9	13.9			

^a See text

Table 7.1: Parameters and results of the first collision sequence studied in this paper. For each subsequent collision N we list the time of collision t (in Myr), the primary mass according to the N -body model $M_{1,N\text{body}}$, the primary mass according to our models, assuming complete mixing during the collision $M_{1,\text{mix}}$, the mass of the secondary M_2 and the mass of the remnant after the collision M_{merger} (all in solar masses). For comparison we also give the masses $M_{1,\text{MMS}}$ for the MMAMS models that we were able to calculate. The final row gives the age at which our evolution calculations stopped and the mass of the collision product at the end of the evolution (assumed black hole mass).

7.3 Results

The initial conditions and outcome of each of our merger sequences are listed in Tables 7.1, 7.2 and 7.3. The tables give the time of collision t , the secondary mass M_2 and the mass of the primary according to the different merger prescriptions. Sequence three was recalculated for $Z = 0.001$ and the results for this run are given in Table 7.4.

N	t	$M_{1,N\text{body}}$	$M_{1,\text{mix}}$	M_2	M_{merger}
1	0.72251	91.8	86.5	81.9	150.1
2	0.72252	173.7	150.1	80.2	206.7
3	0.88257	253.8	198.9	68.6	245.6
4	0.88522	322.5	245.4	72.9	294.5
5	0.95998	395.4	287.7	1.8	289.4
6	1.41050	397.1	250.0	95.8	309.6
7	1.50639	492.9	298.4	86.1	352.3
8	1.97200	578.8	282.1	97.6	338.2
9	2.22324	676.2	79.8	75.2	130.4
10	2.22325	751.5	130.2	55.4	166.3
11	2.45320	806.7	83.9	23.5	100.4
12	2.68305	829.8	66.7	28.4	86.8
13	2.74781	858.0	78.8	1.0	79.8
14	3.08766	857.3	53.5	82.6	105.2
15	3.19983	939.2	46.1	56.3	86.3
16	3.27682	995.0	64.8	41.6	93.6
	4.51074	1036.6	10.1		

Table 7.2: As Table 7.1 for collision sequence 2

N	t	$M_{1,N\text{body}}$	$M_{1,\text{mix}}$	M_2	M_{merger}
1	0.53120	77.8	75.3	70.7	131.5
2	0.57294	148.5	130.7	82.8	191.3
3	0.65612	231.3	188.1	58.5	228.6
4	0.89154	289.8	215.4	96.6	279.9
5	0.89155	386.4	279.9	78.5	332.5
6	1.02208	464.9	318.1	1.5	319.5
7	1.31086	466.4	289.3	56.3	327.9
8	1.50575	522.6	305.7	48.9	340.1
9	2.05327	571.3	164.0	72.7	209.2
10	2.27966	643.8	73.1	2.0	74.8
11	2.60213	645.0	35.1	3.5	37.7
12	3.12235	642.8	19.8	49.3	60.7
	4.59400	692.1	9.7		

Table 7.3: As Table 7.1 for collision sequence 3

The evolution track in the Hertzsprung-Russell diagram for the first merger sequence (Table 7.1) is shown in Figure 7.1. The two other sequences are similar. The location of the ZAMS (up to $200 M_\odot$) is indicated with a dashed line and every 30 000yr is marked with \bullet . The repeated collisions

N	t	$M_{1,\text{Nbody}}$	$M_{1,\text{mix}}$	M_2	M_{merger}
1	0.53120	77.8	77.7	70.7	135.4
2	0.57294	148.5	135.4	82.8	198.3
3	0.65612	231.3	198.1	58.5	239.6
4	0.89154	289.8	239.1	96.6	308.5
5	0.89155	386.4	308.5	78.5	364.2
6	1.02208	464.9	363.5	1.5	364.9
7	1.31086	466.4	363.4	56.3	404.7
8	1.50575	522.6	403.4	48.9	440.2
9	2.05327	571.3	434.9	72.7	487.5
10	2.27966	643.8	390.1	2.0	392.0
11	2.60213	645.0	260.1	3.5	263.3
	2.83153	648.5	171.9 ^b		

^b Mass and time at the moment the evolution failed to converge, rather than the onset of carbon burning.

Table 7.4: As Table 7.3 but for $Z = 0.001$. Note that the merger sequence was terminated earlier than for $Z = 0.02$ and that the merger remnant did not finish its evolution before the evolution code broke down.

N	t	$M_{1,\text{Nbody}}$	$M_{1,\text{mix}}$	M_2	M_{merger}
1	0.88048	66.6	63.6	65.2	113.4
2	1.08887	131.8	110.4	16.4	114.1
	3.10786	106.2	75.4		

Table 7.5: Times t and secondary masses m_2 for the sub merger sequence leading to the secondary of collision 22 in the merger sequence in Table 7.1.

drive the collision product to high luminosities, exceeding the Humphreys-Davidson limit, but the collision product never moves far from the extension of the ZAMS, instead evolving nearly vertically in the HR diagram (similar to the evolution tracks for homogeneously evolving stars, Yoon & Langer, 2005). For reference, the locations of the Pistol Star and η Carinae are also shown. The location of η Car is based on Hillier et al. (2001), with the spread in effective temperature due to the spread in their radius estimates. The luminosity is based on the infrared flux. The location of the Pistol Star is based on the low luminosity solution of Figer et al. (1998b). We see that the merger remnant is always hotter than either of these two stars, except when it becomes a red supergiant (the red loop in Figure 7.1), at which time it is less luminous. During the merger sequence the luminosity can exceed the luminosity of these stars. On the other hand, η Carinae and the Pistol Star are both obscured by optically thick outflows, which means that comparing with the effective temperature of our model can be misleading

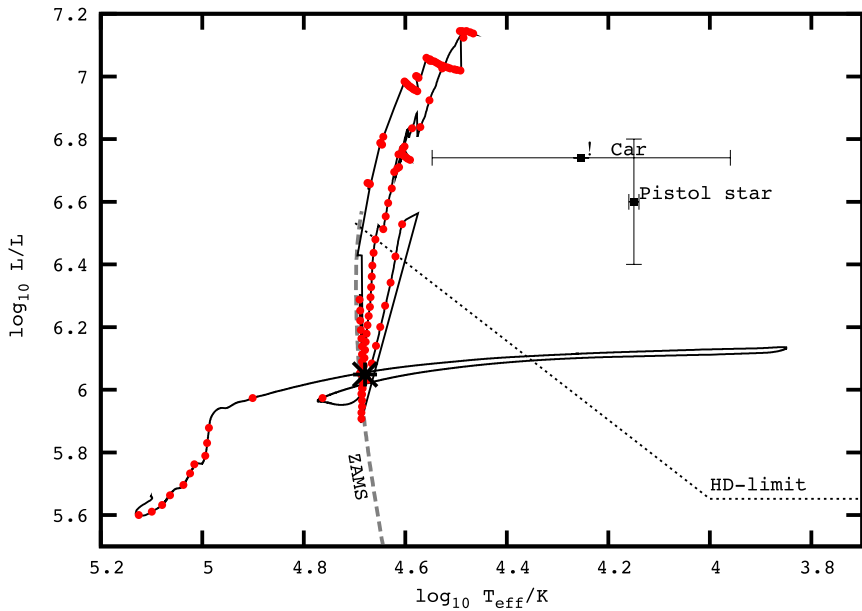


Figure 7.1: Evolution track of the merger from sequence 1 in the Hertzsprung-Russell diagram. The starting point is indicated by * and points are plotted on the evolution track after each 30 000 yr. The dotted line indicates the Humphreys-Davidson limit. For reference, the theoretical ZAMS (running up to $200 M_{\odot}$) and the locations of η Carinae and the Pistol Star are also plotted.

because we do not model such an optically thick wind. The location of the collision product above the Humphreys-Davidson limit suggests that it is a luminous blue variable (LBV) star, so that in reality its position in the HRD is likely to be variable.

The high luminosity increases the mass-loss rate, leading to a competition between mass loss due to stellar winds and mass increase due to collisions. The time evolution of the mass of the mergers is shown in Figure 7.2. The dashed lines give the mass that was predicted in the N -body simulation while the solid lines show our fully mixed models for $Z = 0.02$. The two agree well for the first few collisions, but mass loss due to stellar wind prevents the mass from exceeding $500 M_{\odot}$. The surface of the merger remnants becomes helium rich and after 1.5–2 Myr turns the star into a Wolf-Rayet star. The strong WR mass-loss rate (up to $3.6 \cdot 10^{-3} M_{\odot} \text{ yr}^{-1}$ when the collision product first becomes a WR star) brings the mass down very quickly, to $\sim 100 M_{\odot}$ after the final collision and $10\text{--}14 M_{\odot}$ at the time of carbon ignition.

In Figure 7.3 we follow the evolution of the radius. Our collision products have substantially larger radii (up to a factor three, note the logarithmic scale) than predicted by the N -body code, despite the smaller mass. This

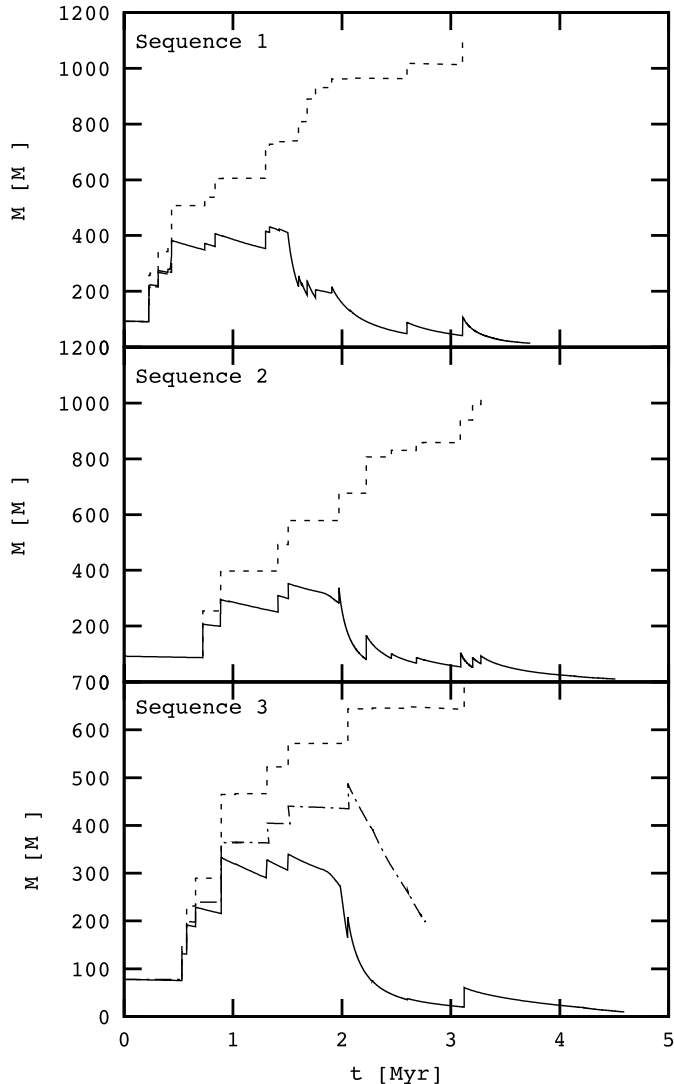


Figure 7.2: The mass of the merger product as a function of time for the three merger sequences listed in Tables 7.1–7.3. The solid line is the mass found from the detailed models assuming homogeneous mixing, the dashed line is the mass predicted from the N -body calculation. The dash-dotted line in the bottom panel is the mass of the $Z = 0.001$ run.

is due to a peculiarity in the structure of the collision product, which will be discussed in detail in §7.3.1. When the collision product becomes a WR star, the radius decreases substantially and the collision product can be up to an order of magnitude smaller than was assumed in the N -body calculation. After core hydrogen exhaustion the collision product still has a thin hydrogen-poor ($X \approx 4\%$) envelope. Expansion of this envelope is

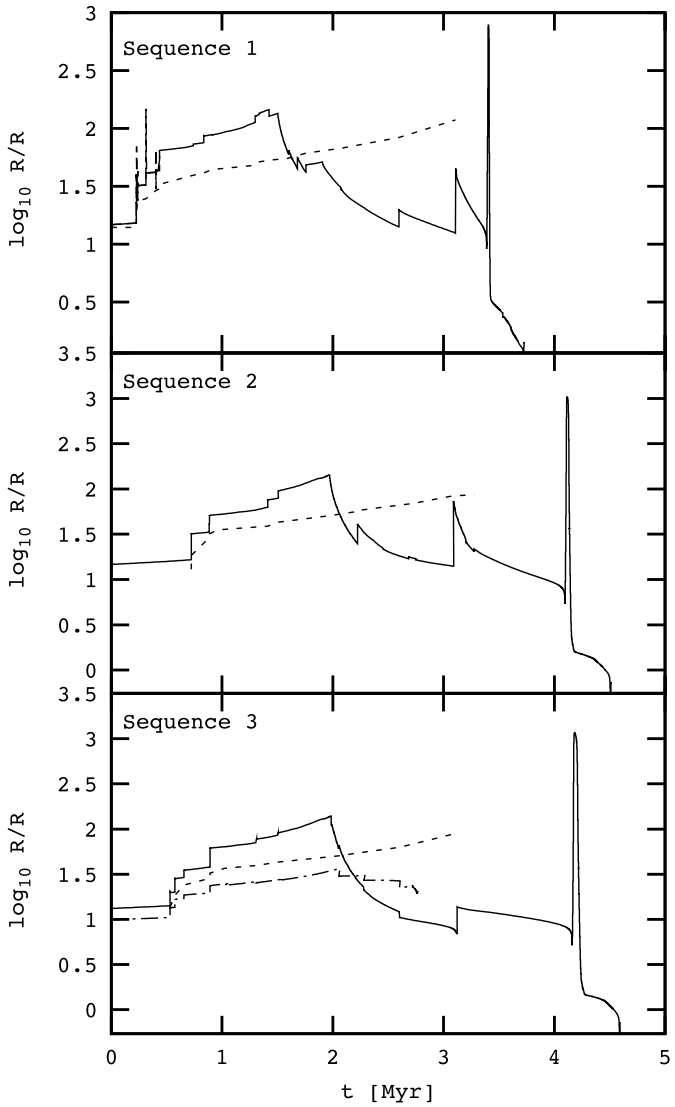


Figure 7.3: The radius of the merger remnant of the three sequences against time. The solid line is the prediction from our homogeneous models while the dashed line is the radius from the N -body code. The long dashed line in the top panel is the radius from the MMAMS model, which shows spikes at each collision because the merger remnant is out of thermal equilibrium immediately after the merger. The dash-dotted line in the bottom panel is the radius of the $Z = 0.001$ run.

responsible for turning the star into a red supergiant and causes the spike in the radius at 3.5 Myr (first sequence) and 4.1 Myr (second and third sequence). During the red supergiant phase the collision product is again above the Humphreys-Davidson limit, but this phase is very short, lasting

$17 \cdot 10^3$ yr ($< 1\%$ of the lifetime of the star).

We have also plotted the mass and radius from the MMAMS models that we were able to calculate. In the upper panel of Figure 7.2 the MMAMS model is indistinguishable from the homogeneous model. After the collision the merger remnant is out of thermal equilibrium and is inflated. The increase in radius at each collision can be seen in the upper panel of Figure 7.3. Once the collision product reaches thermal equilibrium (after $\sim 10^4$ yr) the radius closely follows the radius of the homogenised model, indicating that the homogenised model is indeed a reasonable approximation of the structure of the merger remnant. Because the radius is larger while the collision product is out of thermal equilibrium it is more likely to interact or collide with other stars at this time, but since we do not take feedback on the dynamics into account this effect is not important for our present considerations.

The collision sequences mostly involve main-sequence stars but a few of the listed collisions are special. Collision 22 of the first sequence involves the remnants of two collision runaways. The star that has undergone the longest sequence of collisions (the “primary”) is an early type Wolf-Rayet star at this point with a surface hydrogen abundance of 0.24 and a mass of $41M_\odot$. However, it is still undergoing core hydrogen burning. The star that has undergone the shortest merger sequence (the “secondary”, see Table 7.5) is a core helium burning star of $75M_\odot$ that has not yet become a Wolf-Rayet star (although it is close to fulfilling our criteria) and has a surface hydrogen abundance of 0.44. In our homogeneous mixing treatment the result is a collision product that has been enhanced in carbon (see the surface abundance plot in Figure 7.5), which is converted into nitrogen through CNO processing. In a more detailed treatment of the merger process we expect the dense helium core of the secondary to sink to the centre of the collision product so that the merger remnant would have a hydrogen depleted core.

A similar situation occurs for collision 14 from the second sequence, for which the secondary has also become a core helium-burning star at the time of collision.

7.3.1 Structure and size of the merger remnants

During dynamical interactions in a dense cluster, the size of the merger remnant is one of the parameters that determines the probability of subsequent collisions. As mentioned, the large radius of the $Z = 0.02$ models during the first 1.5–2 Myr in Figure 7.3 is caused by a peculiarity of the stellar structure.

The merger remnants become very massive and are almost fully convective. The lower panel in Figure 7.4 shows the location of convection zones against the enclosed mass, the upper panel shows the same information as a function of the radius. The central convection zone contains about 90%

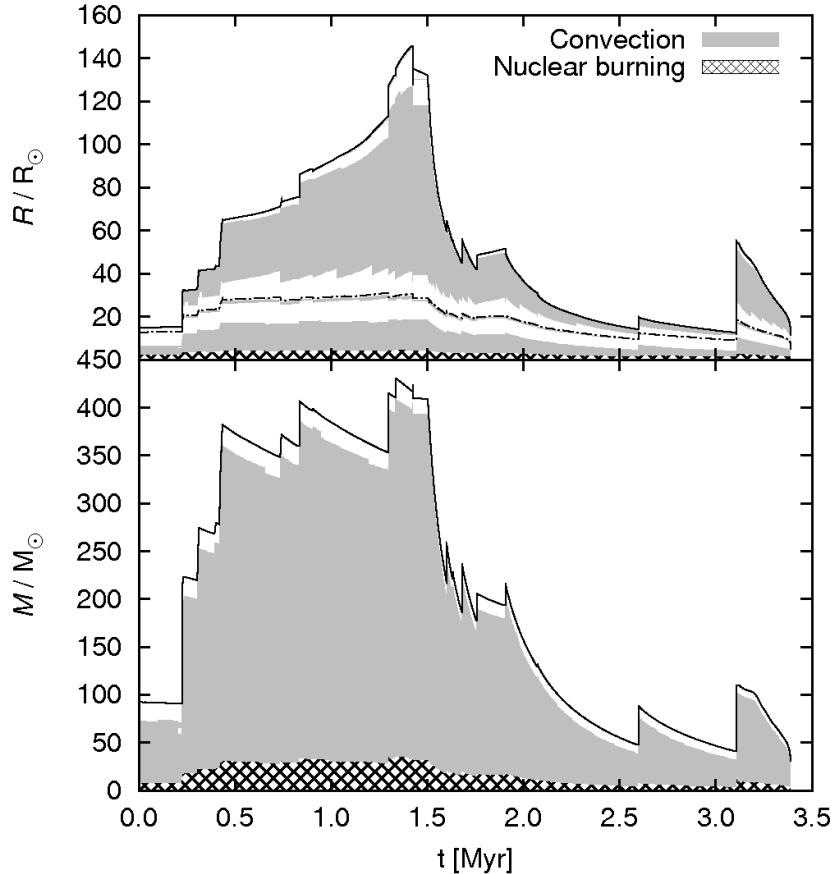


Figure 7.4: Kippenhahn diagram showing the evolution of the collision product of the first merger sequence. The plot shows convection zones against the radius (upper panel) and against mass coordinate (lower panel) as a function of time. In the upper panel the radius containing a fraction $1 - 10^{-5}$ of the stellar mass is indicated with a dash-dotted line. The convective core encompasses 90% of the mass but a much smaller fraction of the radius (at most $20 R_\odot$). Mass loss between collisions exposes material from the convective core.

by mass of the merger remnant. As can be seen from the figure, mass loss between the collisions can reveal material from the central convection zone at the stellar surface (for instance, the mass of the star at 1.3 Myr is lower than the mass of the convective core at 0.8 Myr).

The outer 10% by mass of the merger remnant is radiative, but the upper panel of Figure 7.4 shows two convection zones in this region which correspond to different peaks in the opacity of the stellar material. An

extended convective layer that corresponds to the “Fe bump” is located at large radii. The Fe bump is an increase in opacity around $\log T \approx 5.3$ which was found after introducing the treatment of spin-orbit splitting of iron and nickel into the computation of the opacity tables (Rogers & Iglesias, 1992; Seaton et al., 1994). Deeper down a thin convective layer can be seen, caused by the “deep Fe bump”, occurring around $\log T \approx 6.3$.

Together, these convection zones are very extended in radius but contain almost no mass. It is especially the convection zone corresponding to the Fe-bump which expands even more while the star evolves. When the star reaches its maximum radius of about $150 R_\odot$ after 1.4 Myr, this convection zone extends over $90 R_\odot$, while it contains only about $10^{-4} M_\odot$. At this moment the star consists of a core of less than $30 R_\odot$ in size containing almost all of the mass surrounded by an extended “halo” reaching from 30 to $150 R_\odot$. This halo has an almost constant temperature and density of $10^{-10} \text{ g cm}^{-3}$. This is indicated in Figure 7.4, which shows the radius outside which a fraction 10^{-5} of the stellar mass is located.

This “core-halo” structure has been found before in models of massive stars, for example by Ishii et al. (1999) for hydrogen-rich stars and by Petrovic et al. (2006) for helium stars. Petrovic et al. (2006) note that to provide the high mass-loss rate from the surface a large outward velocity is needed in the outer layers where the density is low. In their models the necessary velocity is larger than the local sound speed by an order of magnitude. This means that the halo cannot be modelled realistically under the assumption of hydrostatic equilibrium and may not be stable. They find that with a more detailed treatment the halo disappears as a result of the high mass-loss rate. Because our merger remnants have a much larger radius the outflow velocity in the halo is about 2–3 orders of magnitude smaller than the sound speed, which suggests that the halo structure is stable in this case. The halo disappears when the merger remnants become Wolf-Rayet stars and the mass-loss rate increases.

7.3.2 Final remnant masses

For each of the three merger sequences the collision product is close to core hydrogen exhaustion when the merger sequence ends. After the end of the main sequence hydrogen continues to burn in a shell very close to the surface. The hydrogen envelope expands, driving the star into a red loop in the HRD. Mass loss from the surface gradually removes the hydrogen envelope, reducing the efficiency of the hydrogen burning shell. When the hydrogen shell is extinguished the star returns to the blue part of the Hertzsprung-Russell diagram. The remaining hydrogen envelope is lost and the star becomes a massive ($\sim 20 - 30 M_\odot$) helium star. By the end of core helium-burning the mass has gone down to $10 - 14 M_\odot$, 80% of which is taken up by the C/O core. The expected outcome of the evolution for such stars is a

	Sequence 1 Single	Sequence 1				
		Collision	Wind			
ΔM	647.5	228.6	695.8	95.4		
H	0.4806	0.5648	0.4006	0.0899		
He	0.4965	0.4000	0.5794	0.8308		
C	0.0040	0.0012	0.0003	0.0306		
N	0.0092	0.0166	0.0132	0.0294		
O	0.0040	0.0013	0.0010	0.0060		
	Sequence 2			Sequence 3		
	Collision	Wind	Remnant	Collision	Wind	Remnant
ΔM	191.8	549.9	83.5	142.3	456.6	102.0
H	0.5599	0.3489	0.1944	0.5521	0.3361	0.2025
He	0.4093	0.6311	0.7637	0.4305	0.6439	0.7553
C	0.0090	0.0003	0.0133	0.0004	0.0003	0.0184
N	0.0117	0.0133	0.0128	0.0105	0.0134	0.0123
O	0.0044	0.0009	0.0081	0.0013	0.0008	0.0050

Table 7.6: Ejected mass and composition for the three computed merger sequences compared to a population of single stars. The first row lists the total mass ΔM (in solar units) lost through each of the three listed channels, the remaining rows give the abundances (by mass) of H, He, C, N and O. For each sequence the first column lists the ejecta from the collision, the second column lists the integrated values for the stellar wind during the merger sequence and the third column lists the values for the evolution of the merger remnant after the merger sequence has ended. The single star yields correspond to the stars involved in the first merger sequence.

complete collapse to a black hole (Belczynski et al., 2002).

In each of these sequences $600 - 900 M_{\odot}$ is lost to the interstellar medium. Most of this material is lost due to stellar wind between collisions (see Table 7.6) rather than in the ejecta of each collision.

7.3.3 Surface abundances and chemical yields

In the course of its evolution the surface of the merger remnant gradually becomes helium rich, as can be seen in the top panel of Figure 7.5. The CNO abundances (shown in the bottom panel of Figure 7.5) change strongly at the first collision and then stay mostly constant up to $t \approx 3$ Myr.

The abundances change most strongly during collisions. This is because the merger remnant is fully mixed at this stage. The abundances also change in between the collisions, as mass loss strips away the surface layers and reveals the deeper layers, but the change is not visible on the scale of the plots until the merger remnant becomes a Wolf-Rayet star. In sequences 1 and 2 the merger remnant undergoes a collision with a core helium-burning

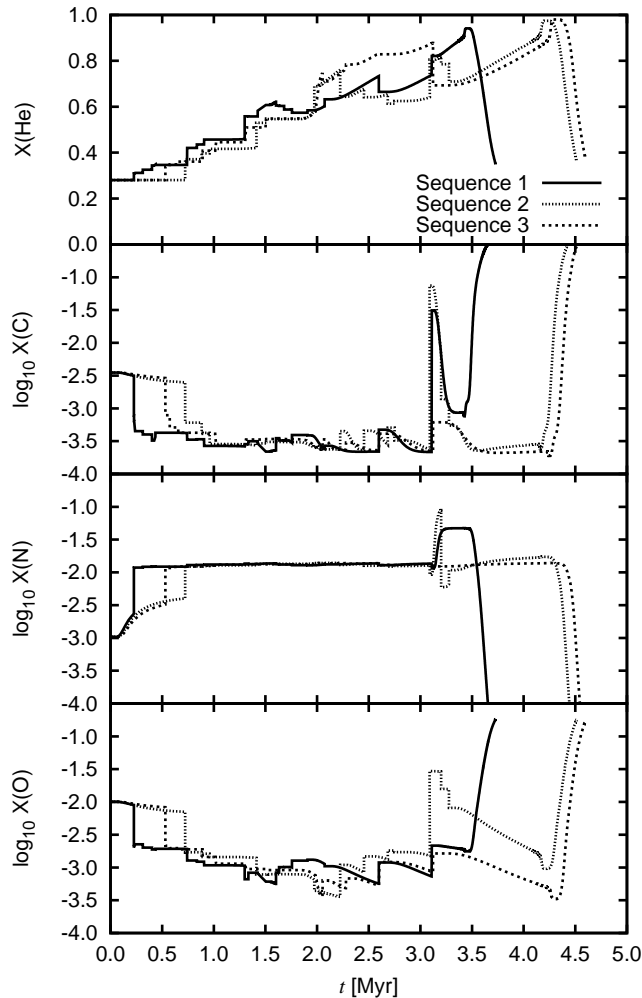


Figure 7.5: Surface He, C, N and O abundances (by mass fraction) for as a function of time (in Myr) for the three $Z = 0.02$ sequences.

star at 3Myr. This results in a strong increase in the carbon abundance (and oxygen, for sequence 2) and a decrease in the nitrogen abundance (through dilution). CNO cycling then converts the carbon into nitrogen, producing a nitrogen-rich WR star. However, our assumption of complete mixing is unlikely to be valid for collisions with core helium-burning stars. More likely, most of the carbon and oxygen would remain in the core of the collision product and such a strong increase in surface C and N probably

does not occur.

As the collision product continues to evolve after the end of the merger sequence, the surface helium abundance increases until the hydrogen envelope has been lost and the surface is nearly pure helium. The stellar wind continues to expose deeper layers of the star, eventually revealing at the surface the ashes of helium burning. At this point, the surface nitrogen and helium abundance decrease while the carbon and oxygen abundances increase strongly. At the end of the evolution, carbon is the most abundant element on the surface.

The expulsion of gas from the cluster is usually attributed to supernova explosions, which are expected to start after about 3 Myr. The merger remnant loses most of its mass before this time. Table 7.6 gives the composition of the material lost from the merger remnant as well as the amount of material lost, split into three categories: ejecta from the collisions, mass loss due to stellar wind during the merger sequence and mass loss from the collision product after the end of the merger sequence. Most of the material is ejected in the form of a stellar wind between collisions, followed by the material that is lost during the collisions. The material that is lost by the collision product after the end of the merger sequence is significantly more helium rich than the material that was lost before. This simply reflects the increased surface helium abundance of the collision product. The material lost from the collisions is less helium rich than the material that is lost in the wind. This is partially due to the increase in the surface helium abundance between collisions (Figure 7.5) and partially due to the fact that the estimated mass loss from the collision is larger for more equal masses and becomes smaller when the mass ratio is more extreme, which is the case for later collisions when the collision product is both massive and helium rich.

If we compare the yields of the first sequence to the yields that would have been obtained if the stars involved in the merger had been allowed to evolve on their own (column 2 in Table 7.6) we first note that the single stars eject much less material than the merger sequence. This is because the merger sequence produces one $13.9 M_{\odot}$ black hole, while the single stars above $30 M_{\odot}$ all produce black holes of $8\text{--}24 M_{\odot}$. The ejected material is also less helium rich than the material that is lost from the merger remnant: the single star models lose $321 M_{\odot}$ of helium and $311 M_{\odot}$ of hydrogen ($\text{He}/\text{H} \approx 1$), while the merger product loses $574 M_{\odot}$ of helium and $416 M_{\odot}$ of hydrogen ($\text{He}/\text{H} \approx 1.4$). This is directly related to the large size of the convective core: for the merger remnant, 90% of the material has undergone nuclear processing in the core, which is a much larger fraction than for the population of single stars.

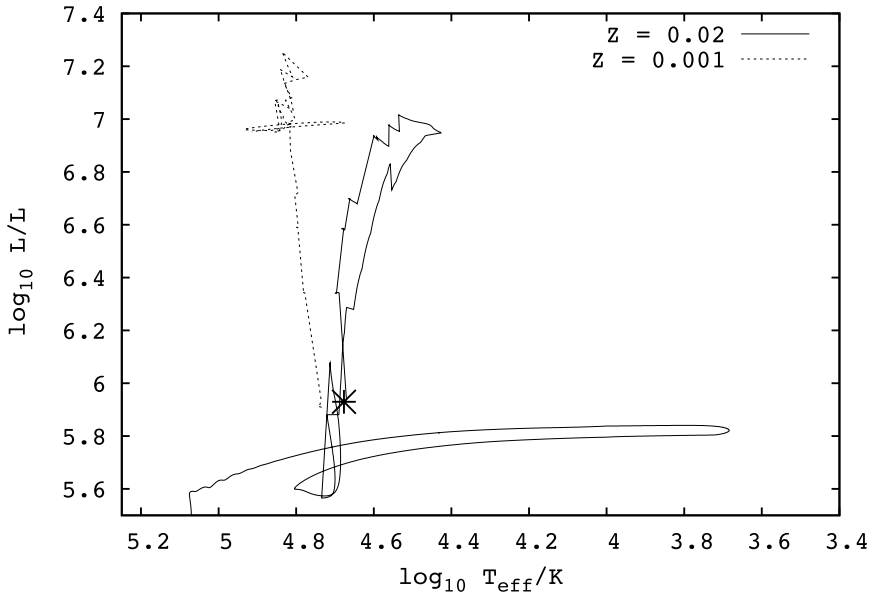


Figure 7.6: Evolution track of the merger remnant of sequence 3 for $Z = 0.02$ (solid line) and $Z = 0.001$ (dashed line). Note that the $Z = 0.001$ track remains much brighter than the $Z = 0.02$ track.

7.3.4 Metallicity effects

Because mass-loss rates are lower at low metallicity we have recalculated sequence 3 for $Z = 0.001$. At this metallicity the mass-loss rates are about 13 times lower than for $Z = 0.02$, which means that the remnant can become more massive.

The mass of the remnant after the last collision in the sequence is $263M_{\odot}$. We followed the evolution of the merger product through core helium burning until the core helium abundance has decreased to $Y_c \approx 0.63$ (about one third of the core helium-burning lifetime), at which time the mass is $172M_{\odot}$. Numerical problems prevented us from evolving this model further until carbon ignition. We extrapolated the mass loss as a linear function of the central helium abundance (rather than time) to the moment of helium exhaustion, which was found to give a good estimate of the final mass for $Z = 0.02$. Based on this extrapolation we expect the final mass to be $\sim 120M_{\odot}$ by the time of carbon ignition. The expected fate of this merger remnant is a pair-creation supernova (Langer et al., 2007; Portegies Zwart & van den Heuvel, 2007).

Because the opacity bump that gives rise to the core-halo structure is associated with iron, the core-halo structure does not appear at low metallicity and the collision product remains more compact. This is why in the bottom panel of Figure 7.3 the radius of the $Z = 0.001$ model (dash-dotted

line) is smaller than the radius of the $Z = 0.02$ model until 2 Myr, when the latter becomes a WR star. The radius is always smaller than the radius assumed in the N -body calculations.

The lower mass-loss rate makes it easier to build up more massive remnants, but the smaller radius reduces the probability of a collision and may prevent the occurrence of a runaway merger. The thermal timescale is also shorter at low metallicity, meaning that the star will reach thermal equilibrium faster after the collision. An additional complication is that the lifetime of the stars is reduced at lower metallicity (because of their larger mass) so that there is less time to form the merger sequence. Fully self-consistent dynamical models (in which the stellar evolution, stellar collisions and stellar dynamics are all treated consistently) are necessary to determine which of these effects dominates in practice.

7.4 Discussion and conclusions

We have found that the end result of a runaway merger at solar metallicity is a $\sim 100M_{\odot}$ WR star after the final collision that produces a $\sim 10M_{\odot}$ black hole. Most of the mass is lost in the form of a stellar wind enriched in N and He. At lower metallicity the mass-loss rates are reduced and the remnant mass can be larger ($\sim 260 M_{\odot}$), possibly leading to a pair-creation supernova. In none of the cases we studied an intermediate-mass black hole is formed.

The material that is lost from the collision remnant is helium rich and shows the signature of CNO processing (N enhancement, C depletion). Because the merger remnant loses most of its mass in the first 3 Myr, the timescale on which we expect the first supernovae to go off, the primordial gas may not yet have been expelled from the cluster. In this case the material that is lost from the merger remnant can be retained in the cluster and could be accreted onto other stars or used in further star formation. This offers the possibility of finding a chemical signature in clusters observed today where a merger sequence occurred in the past. In order to do this we require more detailed nucleosynthesis than the models described in this paper provide. The amount of ejected material is probably not enough to account for a second generation of helium-rich stars as is found in some globular clusters, since such a helium-rich population generally seems to comprise about 15–20% of the stars in the cluster (Pumo et al., 2008), which is larger than the fraction of mass lost from the merger remnant compared to the total cluster mass.

The main uncertainty in our models is the adopted mass-loss rate. We have used established mass-loss prescriptions from the literature. Our adopted Vink et al. (2001) rate is derived for stars that are further away from their Eddington luminosity than our collision products and is likely to be an un-

derestimate of the true mass-loss rate for our stars.

When the surface hydrogen abundance $X_s < 0.4$ we apply WR mass loss rates. This transition is somewhat arbitrary and ideally we would use a single mass loss recipe that predicts the mass-loss rate as a function of the local luminosity, temperature, effective gravity and composition. No such recipe is available in the literature at this time.

The mass-loss rate can become very high during the WR phase due to our extrapolation of the empirical rate to higher luminosity than for which it was derived. We have made sure that the power used to drive the wind is always less than that provided by the star's luminosity (Owocki et al., 2004). When the collision products first become WR stars, the mass-loss rate is still very high. In part this is due to the sudden transition to WR mass loss rates when X_s drops below 0.4. We expect that if the transition is made more smoothly the mass-loss rate would increase earlier and avoid the high peak value found in our current models. This again stresses the need for a unified single mass loss prescription.

Our collision products have luminosities close to their Eddington luminosity and for a substantial amount of time exceed the Humphreys-Davidson limit. Stars close to this limit become luminous blue variables which can lose a large amount of mass in outbursts. A model that describes mass loss from stars that exceed their Eddington luminosity is the so-called porosity model (Owocki et al., 2004; Owocki & van Marle, 2008). Our models come close, but do not exceed their Eddington luminosity. We have made one trial run with the mass-loss rate artificially enhanced by a factor of 50 and found that the star is very quickly stripped of its mass.

We have ignored rotation in this work. Rotational mixing is expected to be unimportant because our models are almost fully convective. Rapid rotation is also expected to enhance the mass-loss rate from stars, especially close to the Eddington limit. This enhanced mass loss is compounded by the need to lose angular momentum from the collision product before it can reach thermal equilibrium. In effect this increases the uncertainty in the already uncertain mass loss rate.

The radius of our detailed evolution models is different from the radius that was used to detect collisions in the N -body run. This demonstrates that it is important to perform fully self-consistent simulations of collision runaways. Calculations at lower Z are especially interesting since remnant masses can be higher due to a reduced stellar wind, but on the other hand collisions are less likely because the stars are more compact. Calculations like those by Belkus et al. (2007) in which the stellar evolution is treated with an analytic recipe, are an important step in this direction.

Summary

The research carried out in this thesis is focused on a systematic study of stellar collisions in young star clusters. Massive stars, which are abundant in young stars clusters, have a profound influence on the dynamical evolution of a star cluster. To simplify the matter, we split the evolution of a cluster in two phases: before and after stellar evolution has a significant impact on cluster dynamics. The evolution of individual stars has little influence on the dynamics of a star cluster in the first three million years of its life. However, after three million years the stellar evolution has a considerable impact on stellar motions due to mass loss in supernova explosions. In this thesis we have mostly focused on star clusters whose age does not exceed three million years, such as Arches cluster in the Galactic Centre or R136 in the Large Magellanic Clouds (LMC).

An important process in the early evolution of a star cluster is mass segregation: stars which are more massive than the average stellar mass migrate to the central region of a star cluster, known as the core of the cluster. As a result of mass segregation, the number of massive stars, and therefore the mean stellar mass, increases in the core and decreases in the outer regions of the cluster. This process continues until a massive binary star is formed in the cluster centre. The further evolution of a star cluster is modified by the presence of a massive binary star. This binary star prevents any further increase of the number of massive stars in the core. Such young clusters are mass segregated, and indeed there is observational evidence of mass segregation in various young star clusters.

It is important to quantify the degree of mass segregation that can be reached via the dynamical evolution alone. This can be compared to the observational data in order to identify the origin of mass segregation in young star clusters: primordial or due to dynamical evolution. An interesting example is the Arches cluster. The present day observational data reveals that the mass function in its core (core mass function) can be fitted with a double power law function: the mass function slope above about six solar masses, which we call pivot mass, is shallower than below. One of the proposed explanations is that Arches' mass function represents the initial cluster mass function (IMF), which has been developed during the cluster formation process. However, it remains unclear why other young star clusters do not have such properties in their IMF.

In this thesis we found that Arches' core mass function is the natural outcome of the dynamical evolution. We studied time and radial dependence of an initially non-segregated cluster with the Salpeter IMF. Even though the core mass function is initially described by a single power law, it eventually deviates from its initial state and develops a break at the pivot mass. We found that the best fit for the simulated mass function is a double, rather than a single, power law. Moreover, the simulation data predict that the pivot mass is equal to twice the mean stellar mass in the cluster. It is important to stress that this result does not require any peculiar mass function and is consistent with the assumption that the Arches was born in non-segregated. Moreover, it predicts that the mean mass of the Arches cluster is about three solar masses—a value which is consistent with the observational data.

A cluster which is non-segregated at birth takes some time to reach the state of mass segregation. This time depends on both the mass and the size of the cluster: the larger and the less massive cluster is, the more time it takes to become mass-segregated. Clusters with age below a certain value cannot reach a segregated state, unless they are born already mass-segregated. The ability to detect mass segregation in young star clusters is an important step in this venture. Observations that rely on the individual star count cannot be applied to the clusters located beyond LMC. For these clusters one has to rely on the integrated properties, such as photometric or spectroscopic.

Integrated photometric properties can, in principle, provide information about mass segregation in young star clusters of co-evolving stars. In segregated clusters, massive stars, which are first to leave main-sequence, are concentrated in the central regions of the cluster, whereas lower mass stars, which are located farther away, continue their evolution on main-sequence. Main-sequence stars emit most of their light in blue/green colours compared to post-main sequence stars, whose spectra is dominated by red colour. Therefore, size of the observed core of a segregated cluster with the age exceeding three million years should depend on the colour in which the cluster is observed: the core should appear smaller in red colour when compared to blue or green colour. This indeed has been observed in various young star clusters. However, it became clear later that this was caused by different effects, such as differential extinction or variation of point spread functions. After corrections for these effects, size of the observed core was consistent in all colours.

It is therefore desirable to have quantitative estimates on the degree to which mass segregation affects integrated photometric properties. We find in this thesis that most of the light in all colours are emitted by stars in a narrow mass interval concentrated near the turn-off mass at a given epoch. This is the result of a steep dependence of mass-luminosity relation. As a result, stars of similar masses dominate integrated photometric properties

for all colours and at all ages. But stars of similar mass have similar spatial distribution, and therefore the differences in observed core radii are small. In our models, which were motived by the Arches' mass function, these differences do not exceed ten percents.

Mass segregation in young star clusters is a necessary condition for stellar collisions. Accumulation of large number of massive stars in a compact region inevitable leads to close interactions between some stars, and some of these interaction are so close that stars may collide and merge. However, the path towards the first collision in young star clusters is rather complicated. The naive assumption that two single stars eventually collide with each other, like in globular cluster, does not hold in young star clusters. Instead, the formation of a massive binary star is a more likely outcome than a collision between two single stars. Collisions are likely to occur between one of the member of a massive binary star, either dynamically formed or of primordial origin, and a single star.

The outcome of a collision between a binary and a single stars can only be studied by means of hydrodynamical simulations. The exact details of the interaction depends on the geometry of the colliding stars, such as binary orientation with respect to the incoming single star, their velocities and masses. Despite the complicate interaction between three stars during a collision event, we found that all three stars participating in the collision are likely to merge. Initially, an intruder stars merges with one of the binary members. The resulting hydrodynamical mess exerts a drag force on the remaining binary system. As a result, the binary separation and eccentricity decreases. Moreover, if the binary separation is small enough, the unstable mass transfer will eventually commence, and binary will merge. In this case, the remaining collision product acquires kick velocity which is caused by the asymmetric mass loss during binary in-spiral. In some cases, this kick velocity is large enough that the collision product can be ejected from the core of a cluster. This therefore predicts an exciting possibility to observe collision products in the outer regions of a star cluster, and the Pistol star, which is located a parsec away from the core, in the Quintuplet cluster is a possible candidate.

In order to study the further evolution of a collision product, it is necessary to understand its structure. This can be obtained by carrying out high-resolution detailed three-dimensional hydrodynamic simulations. However, this is a computationally intensive procedure which can only be used to study individual cases. If one, on the other hand, is interested in modelling large number of merger events, such as in the case of the evolution of a runaway collision product, an approximate and quick modelling is desirable. It turns out that the final distribution of the fluid in the collisions product is governed by a single physical process: the Archimedes' principle. If two stars of same age and with different masses collide together, the fluid from

a dense low mass stars occupies the centre of the collision product and is being surrounded by the fluid from less dense high mass star. Nevertheless, some of the fluid from one star is mixed with the fluid of the other star.

In this thesis, we have developed an approximate method which quickly generates the structure of a collision product between two massive stars. In conjunction with stellar evolution methods, this allowed us to make a first attempt to consistently study the evolution of a runaway collision product, which is the result of the merger of a large number of stars within few million years. This process may take place in young dense star cluster. In star cluster simulations, the mass of the runaway collision product was exceeding one thousand solar masses. It was therefore hypothesised that such an object can be a progenitor of an intermediate mass black holes.

These simulations, however, ignore mass loss during the collision and during the evolution of the product between merger events. While the former seems to be a plausible assumption since the mass loss in a collision between two main-sequence stars is few percent, the mass loss between merger events, which is caused by strong stellar winds, strongly influences the evolution of the runaway collision product. The mass loss between merger events is strong enough to considerably slow down growth of the product. Moreover, after about two million years since the beginning of the runaway merger event, the collision product becomes a Wolf-Rayet star which have strong stellar winds. As a result, most of the mass gained in merger events for the past two million years is lost just in a half-million year. In this case, the outcome of a runaway merger event is a stellar mass black hole.

Samenvatting

Het onderzoek in dit proefschrift concentreert zich op een systematisch onderzoek van sterbotsingen in jonge sterrenhopen. Zware sterren, die veel voorkomen in jonge sterrenhopen, hebben grote invloed op de dynamica van een sterrenhoop. Ter versimpeling verdelen wij de evolutie van een sterrenhop in twee fasen: voordat de sterevolutie grote invloed op dynamica van een sterrenhoop uitgeoefend heeft, en de fase erna. De evolutie van individuele sterren heeft weinig effect op de dynamica van een sterrenhoop tijdens de eerste drie miljoen jaar sinds het ontstaan. Na die tijd heeft sterevolutie een aanzienlijk effect op de stellaire bewegingen, voornamelijk vanwege massa verlies in sterrenwinden en supernova explosies. In dit proefschrift concentreer ik mij voornamelijk op sterrenhopen die jonger zijn dan drie miljoen jaar, zoals de Arches sterrenhoop nabij het Galactische Centrum of R136 in de Grote Magelhaense Wolken.

Een belangrijk proces in de evolutie van jonge sterrenhopen is massa segregatie: sterren die zwaarder zijn dan de gemiddeld migreren naar de centrale regio (de kern) van een sterrenhoop. Als gevolg van de massa segregatie neemt het aantal zware sterren, en dus de gemiddelde stellaire massa toe in de kern en af in de buitenste regio's van de sterrenhoop. Dit proces duurt voort tot een zware dubbelster is gevormd in het centrum. De verdere evolutie van een sterrenhoop is vervolgens drastisch beïnvloed door de aanwezigheid van deze zware dubbelster. Deze dubbelster voorkomt verdere toename van het aantal zware sterren in de kern. Zulke jonge sterrenhopen zijn massa gesegregeerd, en inderdaad is er bewijs vanuit de waarnemingen van massa segregatie in verschillende jonge sterrenhopen.

Het is van groot belang om te bepalen hoeveel massa segregatie bereikt kan worden door de dynamische evolutie van sterren. Dit kan vergeleken worden met waarnemingen om te achterhalen of de oorsprong van massa segregatie in jonge sterrenhopen danwel primordiaal, danwel het gevolg van dynamische evolutie is. Een interessant voorbeeld is de Arches sterrenhoop. Uit recente waarnemingen blijkt dat de massafunctie van de kern kan worden benaderd met een dubbele machtswet: de massafunctie boven ongeveer zes zonsmassa's, de zogenaamde pivot massa, is minder steil dan eronder. Een van de voorgestelde verklaringen is dat de Arches' kern massafunctie grote gelijkenis vertoont met een initiele cluster massafunctie (IMF), die ontwikkeld is tijdens de vorming van de sterrenhoop. Het blijft echter onduidelijk waarom andere jonge sterrenhopen niet over dergelijke eigenschappen in hun IMF beschikken.

In dit proefschrift hebben we vastgesteld dat Arches' kern massafunctie het natuurlijke resultaat is van de dynamische evolutie. We hebben tijd en radiale afhankelijkheid van een aanvankelijk gewone sterrenhoop met Salpeter IMF zonder massa segregatie bestudeerd. Hoewel de kern massafunctie in eerste instantie is beschreven door een enkele machtwet, wijkt het uiteindelijk af van de oorspronkelijke toestand en vormt het een kromming rondom de pivot massa. Wij vinden dat de gesimuleerde data het best geapproximeerd kan worden door een dubbele machtwet functie, in tegenstelling tot gebruik van een enkele machtwet. Bovendien voorspellen we, op basis van onze resultaten, dat de pivot massa gelijk is aan tweemaal de gemiddelde stermassa in de sterrenhoop. Het is van belang te benadrukken dat dit resultaat geen merkwaardige massafunctie vereist en in overeenstemming is met de veronderstelling dat de Arches zonder massa segregatie is ontstaan. Bovendien voorspelt dit model dat de gemiddelde massa van het Arches cluster ongeveer gelijk is aan drie zonsmassa's - een aantal dat in overeenstemming is met waarnemingen.

Een cluster dat niet-gesegregeerd is bij de geboorte neemt enige tijd om een toestand van massa segregatie te ontwikkelen. Deze tijdsduur is afhankelijk van zowel de massa en de grootte van de sterrenhoop: naarmate een sterrenhoop groter en minder zwaar is, kost het meer tijd om een toestand van massa segregatie te bereiken. Sterrenhopen onder een bepaalde leeftijd bereiken geen toestand van massa segregatie, tenzij deze hiermee geboren zijn. De mogelijkheid om massa segregatie te ontdekken in jonge sterrenhopen is een belangrijke stap in dit onderzoek. Waarnemingen op basis van individuele sterren kunnen niet worden gemaakt van sterrenhopen voorbij de Grote Magelhaense Wolken. Voor deze sterrenhopen moeten wij gebruik maken van geïntegreerde eigenschappen, zoals fotometrie of spectroscopie.

In principe kunnen geïntegreerde fotometrische eigenschappen informatie verschaffen over massa segregatie in jonge sterrenhopen. In massa gesegregeerde sterrenhopen zijn zware sterren, die als eerste de hoofdreeksfase verlaten, geconcentreerd in de centrale regio's van de sterrenhoop. Daarentegen blijven de minder zware sterren, die zich op grotere afstand bevinden, in de hoofdreeks tijdens hun evolutie. Sterren in de hoofdreeks hebben meer blauwe en groene straling dan na-hoofdreeksfase sterren, waarvan de spectra wordt gedomineerd door rode straling. Daarom is de grootte van de waargenomen kern van een massa gesegregeerde sterrenhoop, ouder dan drie miljoen jaar, afhankelijk van de kleur waarin het cluster is waargenomen: de kern zal een kleinere verschijning hebben in de rode kleur dan in de blauwe. Dit is bevestigd met waarnemingen in verschillende jonge sterrenhopen. Toch werd later duidelijk dat dit veroorzaakt wordt door andere effecten, zoals de differentiële extinctie of variaties in de puntverspreidingsfunctie. Na correctie voor deze effecten was de waargenomen kern even groot in alle kleuren. In dit proefschrift bevestigen we dat het grootste deel van het licht in alle kleuren uitgestraald is door sterren binnen een klein

massa-interval, namelijk bij het eind van de hoofdreeksfase massa. Hierdoor domineren sterren van soortgelijke massa's de geïntegreerde fotometrische eigenschappen voor alle kleuren en op alle leeftijden. Sterren met soortgelijke massa's hebben echter een overeenkomstige ruimtelijke distributie, waardoor er slechts kleine verschillen zijn in de waargenomen straling van de kern. In onze modellen, die door de Arches' massa-functie gemotiveerd zijn, zijn deze verschillen niet groter dan tien procent.

Massa segregatie in jonge sterrenhopen is een noodzakelijke voorwaarde voor sterbotsingen. Door de bundeling van zware sterren in een compacte regio zijn sterke interacties tussen verschillende sterren onvermijdelijk. Sommige van deze interacties zijn zo nabij dat sterren met elkaar kunnen botsen en zich kunnen samenvoegen. De weg naar de eerste sterbotsing is echter vrij gecompliceerd in jonge sterrenhopen. De naïeve veronderstelling dat twee afzonderlijke sterren uiteindelijk met elkaar zullen botsen, zoals dat gebeurt in bolvormige sterrenhopen, gaat niet op voor jonge sterrenhopen. De vorming van een zware dubbelster is namelijk aannemelijker dan een botsing tussen twee afzonderlijke sterren. Botsingen ontstaan vaak tussen een lid van een zware dubbelster, dynamisch gevormd of van primordiale herkomst, en een afzonderlijke ster.

Het resultaat van een botsing tussen een dubbelster en enkele sterren kan alleen worden onderzocht door middel van hydrodynamische simulaties. De exacte details van de interactie is afhankelijk van de geometrie van de systeem, zoals de oriëntatie van de dubbelster met betrekking tot de inkomende afzonderlijke ster, de snelheid en de massa's van beide sterren. Ondanks de complexe interacties tussen de drie sterren tijdens een botsing hebben we vastgesteld dat alledrie de sterren zich waarschijnlijk zullen samenvoegen. In eerste instantie voegt de indringende ster zich met een van de binaire leden. De resulterende hydrodynamische puinhoop oefent dan een slepende kracht uit op het resterende binaire systeem. Hierdoor neemt de binaire scheiding en excentriciteit af. Indien de binaire scheiding klein genoeg is, zal er uiteindelijk een instabiele stofuitwisseling plaats vinden, waardoor de dubbelster fuseert. In dit geval krijgt het resterende overblijfsel van sterbotsingen een impulsnelheid die wordt veroorzaakt door asymmetrisch massaverlies tijdens de binaire inwaartse spiralisatie. In sommige gevallen is deze snelheid zo groot dat het overblijfsel wordt uitgeworpen uit de kern van de sterrenhoop. Dit resultaat voorspelt dus een spannende mogelijkheid om overblijfselen van sterbotsingen waar te nemen in de buitenste regio's van een sterrenhoop. Kandidaat voor deze waarnemingen is mogelijk de Pistolet ster, die op een parsec afstand ligt van de kern in de Quintuplet sterrenhoop.

Om de evolutie van de overblijfselen van botsingen te bestuderen, is het noodzakelijk om de structuur daarvan te begrijpen. Dit begrip kan worden verkregen door het uitvoeren van gedetailleerde 3D hydrodynamische simulaties met hoge resoluties. Dit is echter een computationeel intensieve procedure die alleen kunnen worden toegepast voor individu-

ele gevallen. Aangezien wij geïnteresseerd zijn om een groot aantal fusies te modelleren, bijvoorbeeld kettingbotsingen, is een snelle approximatiieve modellering wenselijk. Uit onze resultaten blijkt dat de definitieve verdeling van een vloeistof in de overblijfselen van de botsingen wordt geregeld door een fysiek proces: het Archimedes principe. Als twee sterren van dezelfde leeftijd en met verschillende massa's botsen, bevindt de vloeistof afkomstig van de geconcentreerde ster met weinig massa zich in het centrum van het botsing overblijfsel, en wordt deze omringd door de vloeistof uit de minder geconcentreerde hoge massa ster. Desondanks wordt een deel van de vloeistof van de ene ster gemengd met de vloeistof van de andere ster.

In dit proefschrift hebben we een approximatiieve methode ontwikkeld die snel de structuur van overblijfselen van een botsing tussen twee zware sterren genereert. In combinatie met sterevolutie technieken konden we een eerste studie maken van de evolutie van het eindproduct van een kettingbotsing, veroorzaakt door de fusie van een groot aantal sterren binnen een paar miljoen jaar. Dit proces kan plaatsvinden in jonge en geconcentreerde sterrenhopen. In simulaties van jonge sterrenhopen bereikt het eindproduct een massa van meer dan duizend zonsmassa's. Daarom wordt er verondersteld dat een dergelijk object een voorloper kan zijn van een middelzwaar zwart gat.

Deze simulaties negeren echter massa verlies tijdens botsingen en door evolutie van het eindproduct tijdens fusie gebeurtenissen. De eerste hypothese lijkt plausibel, aangezien het massaverlies in een botsing tussen twee hoofdreeks sterren een paar procenten bedraagt. Daarentegen is het massaverlies tussen gebeurtenissen, die worden veroorzaakt door sterke stellaire winden, van aanzienlijke invloed op de evolutie van het botsingsproduct. Het massaverlies tussen de gebeurtenissen is groot genoeg om de groei van het botsingsproduct aanzienlijk te vertragen. Bovendien wordt, ongeveer twee miljoen jaar na het begin van de botsingen, het eindproduct een Wolf-Rayet ster met zeer sterke sterrenwinden. Het gevolg is dat het grootste deel van de massatoename door samenvoeging in de laatste twee miljoen jaar verloren gaat in slechts een half miljoen jaar. In dit geval is het resultaat van een botsingsreeks een minder zwaar zwart gat van ongeveer tien zonsmassa.

Acknowledgements

These days getting a PhD is a journey which is impossible to accomplish without contributions from various people around the world. Here, it is excellent time and place to thank all those people who directly and indirectly contributed to the completion of this thesis.

In the first and the foremost place I would like to thank my supervisor, Simon Portegies Zwart, who, despite being very busy, has always been helping me in virtually every step of this adventure. I would like to use this opportunity to thank him for all time he spent in my office discussing science with me. I found his advises about how to write, present and carry out science very valuable, and they helped me to mature and grow scientifically: it is enough to compare my first and last published paper, my first and last presented talk.

I would like to thank my promotores, the members of the doctorate commission, my friends & colleagues, who took their valuable time to carefully and critically read my original manuscript and to provide valuable comments which helped me to improve the thesis. Unfortunately, getting the missing “s” & “d” at the end of, and “the” & “a” in front of, the words has always been a problem for me.

I also would like to thank Evert Glebbeek & Onno Pols, the second half of our collaboration between Amsterdam and Utrecht. We solved a number of technical and scientific problems, but there are still a few puzzles left to unravel. Greets to Rob with his interesting views on the life, and to Selma, Peter, Diederik.

Next, I would like to greet my previous & current office-mates. Michael, your Beeriodic table of the elements was very enlightening. Alessia, thanks for your valuable and conservative advises. Derek, you do have a genuine ability to talk, talk & talk (thanks for translating my summary to Dutch!), and you Stefan have an interesting ability to listen, listen & listen. Our visitors: Mark, Clovis, Hui-Chen, Stephanie, Keigo, Michiko, Piet & Steve it has been a great pleasure working with you.

I would like to express my gratitude to a good friend of mine, James Lombardi. Jamie, it is always great working with you, and I hope we will continue collaborating on various exciting topics. Another thank I send to my good friend Ofer Yaron. It has always been fun having you around!

My friends & colleagues at the astronomical institute & section of computational science. Dominik, I still remember the face of our Dutch class teacher. Lianne & Arjan, it has always been fun being a part of your conversations. Thijs, sadly I was not been able to return you a favour. And the rest of people who also have contributed to the pleasant atmosphere: Michiel, Ed, Ralph, Lex, Rens, Carsten, Huib, Joop, Alex, Alfons, Breanndán, Rudy, Peter, Alessandro, Alfredo, Anna, Asaf, Atakan, Atish, Bart, Casey, Diego, Dipankar, Eduardo, Gemma, Hanno, Hendrik, Jason, John, Jordi, Lucinda, Maciek, Manu, Martin, Michael, Michiel, Mihkel, Nanda, Nathalie, Paolo, Peter(s), Piergiorgio, Ramesh, Sera, Syed, Valeriu.

Special thank goes also to our librarians: Liesbeth & Sjoerd; and secretaries: Eva, Nicole, Minou, Annemiek, Lidewijde, Erik, Esther, Fieke, Gaby, Said, you have always been able to solve my little problems.

Life, luckily, is lot limited by research alone, and here I'd like to express my gratitude to all the people outside academia who contributed to the completion of this journey.

Denys & Cathy, I will eventually visit you in Taiwan, it is just a matter of time. Denis, it was fun talking to you about programming, computer graphics, string theory and lots of other interesting stuff. SDT, I hope you'll learn Spanish one of these days. Halim, Nick & Ismail, who could have imagined where we would be today. Rosie, thanks for your and your parents help during my studies at the University of Leicester.

Groeten aan mensen van mijn dansschool: Marianne & Gerard, jullie hebben een aardig gevoel voor humor; Vera, het is altijd leuk met je te dansen, vooral tijdens de danstoetsen; Jan-Jelle, Tatef, Eric, Loredana, Daniel, Mirjam.

Mucho recuerdos envío a buenos amigos de Barcelona: Gloria, Encarna, Irene & Lluis, siempre estáis alegre en es un placer estar con vosotros; Sandra, Laura & Rafa, espero que una día vais por fin a visitarme aquí; Carles, Dolores & Adréa, siempre recuerdo la comida grande en el día de los Reyes.

Хочу отдельно отблагодарить моих школьных учителей. Анатолий Васильевич, большое Вам спасибо за интерес к физике и математике который Вы во мне открыли. Стелла Георгиевна, спасибо Вам за поддержку и помочь в школьные времена. Мои учителя информатики, Михаил Цапу , и математики, Виктор Алексеевич Шелестов, спасибо Вам за уникальные знания которыми я пользуюсь и по сей день.

Ik wil graag mijn goede vrienden bedanken: Anneke, Anita & Jereon. Het was leuk jullie te ontmoeten. Anita, jij bent heel speciaal persoon, en ik waardeer alles dat ik van je geleerd heb.

Мои мама и папа, Нина, Витя и дядя Саша, вы всегда были со мной, в тяжёлые и весёлые моменты. Я очень рад что у меня небольшая но дружная семья.

Thank you all for your help. This journey would not have been completed without your contributions!

List of publications

Refereed publications

1. S. Portegies Zwart, E. Gaburov, H.-C. Chen and M. A. Gurkan, 2007, MNRAS, 378L, 29, *The present day mass function of Arches cluster*
2. E. Gaburov, A. Gulandris and S. Portegies Zwart, MNRAS, 2008, 384, 376, *On the onset of runaway stellar collisions*
3. E. Gaburov, J. C. Lombardi and S. Portegies Zwart, MNRAS, 2008, 383L, 5, *Mixing in massive stellar mergers*
4. E. Gaburov and M. Gieles, MNRAS, in press, arXiv/0801.0596, *Mass segregation in young star clusters: can it be detected from the integrated photometric properties?*
5. E. Glebbeek, E. Gaburov, O. Pols and S. Portegies Zwart, submitted to A&A, *Evolution of runway collision products*

Non-refereed publications

1. E. Gaburov and M. Gieles, 2008, IAU-246, 193, *Integrated properties of mass segregated star clusters*

In preparation

1. E. Gaburov, J. C. Lombardi and S. Portegies Zwart, to be submitted to MNRAS, *Hydrodynamics of stellar collisions in triple stellar systems*
2. E. Gaburov, S. Harfst, K. Nitadori, S. Portegies Zwart and J. Makino, to be submitted to New Astronomy, *Gravitational tree-code on graphics processing units: implementation in CUDA*
3. E. Gaburov, S. Harfst and S. Portegies Zwart, in preparation, *High-precision N-body simulations on graphics processing units*

Bibliography

- Aarseth S. J., 2003, Gravitational N-Body Simulations. Gravitational N-Body Simulations, by Sverre J. Aarseth, pp. 430. ISBN 0521432723. Cambridge, UK: Cambridge University Press, November 2003.
- Adams T., Davies M. B., Sills A., 2004, MNRAS, 348, 469
- Anders E., Grevesse N., 1989, Geochim. Cosmochim. Acta, 53, 197
- Ascenso J., Alves J., Lago M. T. V. T., 2007, A&A, submitted
- Bastian N., Gieles M., Goodwin S. P., Tranco G., Smith L., Konstantopoulos I., Efremov Y., 2008, ArXiv:0806.1460, MNRAS in press
- Bastian N., Gieles M., Lamers H. J. G. L. M., Scheepmaker R. A., de Grijs R., 2005, A&A, 431, 905
- Bastian N., Konstantopoulos I., Smith L. J., Tranco G., Westmoquette M. S., Gallagher J. S., 2007, MNRAS, 379, 1333
- Baumgardt H., Kroupa P., 2007, MNRAS, 380, 1589
- Baumgardt H., Makino J., 2003, MNRAS, 340, 227
- Belczynski K., Kalogera V., Bulik T., 2002, ApJ, 572, 407
- Belkus H., Van Bever J., Vanbeveren D., 2007, ApJ, 659, 1576
- Belleman R. G., Bédorf J., Portegies Zwart S. F., 2008, New Astronomy, 13, 103
- Benz W., Hills J. G., 1987, ApJ, 323, 614
- Bertelli G., Bressan A., Chiosi C., Fagotto F., Nasi E., 1994, A&AS, 106, 275
- Bettwieser E., Sugimoto D., 1984, MNRAS, 208, 493
- Binney J., Tremaine S., 1987, Galactic dynamics. Princeton, NJ, Princeton University Press, 1987, 747 p.
- Böhm-Vitense E., 1958, ZsAp, 46, 108
- Boily C. M., Lançon A., Deiters S., Heggie D. C., 2005, ApJL, 620, L27
- Bonnell I. A., Bate M. R., Clarke C. J., Pringle J. E., 1997, MNRAS, 285, 201
- Brandl B., Sams B. J., Bertoldi F., Eckart A., Genzel R., Drapatz S., Hofmann R., Loewe M., Quirrenbach A., 1996, ApJ, 466, 254

- Bruzual G., 2002, in Geisler D., Grebel E. K., Minniti D., eds, Extragalactic Star Clusters Vol. 207 of IAU Symposium, Stellar Populations in Star Clusters: The Rôle Played by Stochastic Effects. pp 616–+
- Cerviño M., Luridiana V., 2004, A&A, 413, 145
- Clayton D. D., 1983, Principles of stellar evolution and nucleosynthesis. Chicago: University of Chicago Press, 1983
- Cleary P. W., Monaghan J. J., 1990, ApJ, 349, 150
- Cohn H., Hut P., Wise M., 1989, ApJ, 342, 814
- Cotera A. S., Erickson E. F., Colgan S. W. J., Simpson J. P., Allen D. A., Burton M. G., 1996, ApJ, 461, 750
- Cotera A. S., Erickson E. F., Simpson J. P., Colgan S. W. J., Allen D. A., Burton M. G., 1992, in Bulletin of the American Astronomical Society Vol. 24 of Bulletin of the American Astronomical Society, A New Cluster of Hot Stars near the Galactic Center. pp 1262–+
- Dale J. E., Davies M. B., 2006, MNRAS, 366, 1424
- Davies M. B., Benz W., Hills J. G., 1993, ApJ, 411, 285
- Davies M. B., Benz W., Hills J. G., 1994, ApJ, 424, 870
- Davies M. B., Blackwell R., Bailey V. C., Sigurdsson S., 1998, MNRAS, 301, 745
- Davies M. B., Ruffert M., Benz W., Muller E., 1993, A&A, 272, 430
- de Grijs R., Gilmore G. F., Johnson R. A., Mackey A. D., 2002, MNRAS, 331, 245
- de Jager C., Nieuwenhuijzen H., van der Hucht K. A., 1988, A&AS, 72, 259
- De Marchi G., Paresce F., Pulone L., 2000, ApJ, 530, 342
- Dimotakis P. E., 2005, Annual Review of Fluid Mechanics, 37, 329
- Eggleton P. P., 1971a, MNRAS, 151, 351
- Eggleton P. P., 1971b, MNRAS, 151, 351
- Eggleton P. P., 1972, MNRAS, 156, 361
- Eggleton P. P., Tout C. A., Fitchett M. J., 1989, ApJ, 347, 998
- Eldridge J. J., Tout C. A., 2004, MNRAS, 348, 201
- Eldridge J. J., Vink J. S., 2006, A&A, 452, 295
- Elmegreen B. G., 1999, ApJ, 515, 323
- Endal A. S., Sofia S., 1976, ApJ, 210, 184

- Ferguson J. W., Alexander D. R., Allard F., Barman T., Bodnarik J. G., Hauschildt P. H., Heffner-Wong A., Tamanai A., 2005, ApJ, 623, 585
- Figer D. F., 2005, Nature, 434, 192
- Figer D. F., Kim S. S., Morris M., Serabyn E., Rich R. M., McLean I. S., 1999, ApJ, 525, 750
- Figer D. F., Morris M., Geballe T. R., Rich R. M., Serabyn E., McLean I. S., Puettter R. C., Yahil A., 1999, ApJ, 525, 759
- Figer D. F., Najarro F., Gilmore D., Morris M., Kim S. S., Serabyn E., McLean I. S., Gilbert A. M., Graham J. R., Larkin J. E., Levenson N. A., Teplitz H. I., 2002, ApJ, 581, 258
- Figer D. F., Najarro F., Morris M., McLean I. S., Geballe T. R., Ghez A. M., Langer N., 1998a, ApJ, 506, 384
- Figer D. F., Najarro F., Morris M., McLean I. S., Geballe T. R., Ghez A. M., Langer N., 1998b, ApJ, 506, 384
- Fleck J.-J., Boily C. M., Lançon A., Deiters S., 2006, MNRAS, 369, 1392
- Fregeau J. M., Cheung P., Portegies Zwart S. F., Rasio F. A., 2004, MNRAS, 352, 1
- Fregeau J. M., Gürkan M. A., Joshi K. J., Rasio F. A., 2003, ApJ, 593, 772
- Freitag M., Benz W., 2005, MNRAS, 358, 1133
- Freitag M., Gürkan M. A., Rasio F. A., 2006, MNRAS, 368, 141
- Fukushige T., Taiji M., Makino J., Ebisuzaki T., Sugimoto D., 1996, ApJ, 468, 51
- Gaburov E., Glebbeek E., Portegies Zwart S., Pols O., 2008, in preparation
- Gaburov E., Gualandris A., Portegies Zwart S., 2008a, MNRAS, 384, 376
- Gaburov E., Gualandris A., Portegies Zwart S., 2008b, MNRAS, 384, 376
- Gaburov E., Lombardi J. C., Portegies Zwart S., 2008, MNRAS, 383, L5
- Giersz M., Heggie D. C., 1996, MNRAS, 279, 1037
- Girardi L., Bertelli G., Bressan A., Chiosi C., Groenewegen M. A. T., Marigo P., Salasnich B., Weiss A., 2002, A&A, 391, 195
- Girardi L., Bressan A., Bertelli G., Chiosi C., 2000, A&AS, 141, 371
- Girardi L., Bressan A., Chiosi C., Bertelli G., Nasi E., 1996, A&AS, 117, 113
- Glebbeek E., 2008, PhD thesis, Utrecht University
- Glebbeek E., Pols O. R., 2008, ArXiv e-prints, 806
- Glebbeek E., Pols O. R., Hurley J., 2008, in preparation

- Gürkan M. A., Fregeau J. M., Rasio F. A., 2006, ApJL, 640, L39
- Gürkan M. A., Freitag M., Rasio F. A., 2004, ApJ, 604, 632
- Hamada T., Iitaka T., 2007, ArXiv Astrophysics e-prints
- Harrington R. S., 1970, AJ, 75, 1140
- Heger A., Langer N., Woosley S. E., 2000, ApJ, 528, 368
- Heggie D., Hut P., 2003, The Gravitational Million-Body Problem: A Multidisciplinary Approach to Star Cluster Dynamics. The Gravitational Million-Body Problem: A Multidisciplinary Approach to Star Cluster Dynamics, by Douglas Heggie and Piet Hut. Cambridge University Press, 2003, 372 pp.
- Heggie D. C., 1975, MNRAS, 173, 729
- Heggie D. C., Hut P., 1993, ApJS, 85, 347
- Heggie D. C., Mathieu R. D., 1986, in Hut P., McMillan S. L. W., eds, LNP Vol. 267: The Use of Supercomputers in Stellar Dynamics Standardised Units and Time Scales. pp 233–+
- Heggie D. C., Trenti M., Hut P., 2006, MNRAS, 368, 677
- Hillenbrand L. A., Hartmann L. W., 1998, ApJ, 492, 540
- Hillier D. J., Davidson K., Ishibashi K., Gull T., 2001, ApJ, 553, 837
- Hills J. G., 1992, AJ, 103, 1955
- Hills J. G., Day C. A., 1976, Astrophysical Letters, 17, 87
- Hodge P. W., 1967, PASP, 79, 29
- Humphreys R. M., Davidson K., 1979, ApJ, 232, 409
- Hunter D. A., Shaya E. J., Holtzman J. A., Light R. M., O’Neil Jr. E. J., Lynds R., 1995, ApJ, 448, 179
- Hurley J. R., 2007, MNRAS, 379, 93
- Hurley J. R., Pols O. R., Aarseth S. J., Tout C. A., 2005, MNRAS, 363, 293
- Hurley J. R., Tout C. A., Aarseth S. J., Pols O. R., 2001, MNRAS, 323, 630
- Hut P., 1983, ApJ, 268, 342
- Hut P., Bahcall J. N., 1983, ApJ, 268, 319
- Hut P., Verbunt F., 1983, Nature, 301, 587
- Iglesias C. A., Rogers F. J., 1996, ApJ, 464, 943
- Ishii M., Ueno M., Kato M., 1999, PASJ, 51, 417

- Jordán A., 2004, ApJL, 613, L117
- Kim S. S., Figer D. F., Kudritzki R. P., Najarro F., 2006, ApJL, 653, L113
- King I., 1962, AJ, 67, 471
- King I. R., 1966, AJ, 71, 64
- Kippenhahn R., Ruschenplatt G., Thomas H.-C., 1980, A&A, 91, 175
- Kippenhahn R., Weigert A., 1990, Stellar Structure and Evolution. Stellar Structure and Evolution, XVI, 468 pp. 192 figs.. Springer-Verlag Berlin Heidelberg New York. Also Astronomy and Astrophysics Library
- Kormendy J., Richstone D., 1995, ARA&A, 33, 581
- Kroupa P., 2001, MNRAS, 322, 231
- Kroupa P., Tout C. A., Gilmore G., 1993, MNRAS, 262, 545
- Kudritzki R. P., 2002, ApJ, 577, 389
- Lada C. J., Lada E. A., 2003, ARA&A, 41, 57
- Lançon A., Mouhcine M., 2000, in Lançon A., Boily C. M., eds, Massive Stellar Clusters Vol. 211 of Astronomical Society of the Pacific Conference Series, Stochastic Fluctuations in the Spectrophotometric Properties of Star Clusters. pp 34–+
- Langer N., Norman C. A., de Koter A., Vink J. S., Cantiello M., Yoon S.-C., 2007, A&A, 475, L19
- Larsen S. S., 2000, MNRAS, 319, 893
- Larsen S. S., Efremov Y. N., Elmegreen B. G., Alfaro E. J., Battinelli P., Hodge P. W., Richtler T., 2002, ApJ, 567, 896
- Larsen S. S., Origlia L., Brodie J., Gallagher J. S., 2008, MNRAS, 383, 263
- Larsen S. S., Richtler T., 2004, A&A, 427, 495
- Lejeune T., Schaerer D., 2001, A&A, 366, 538
- Leonard P. J. T., Livio M., 1995, ApJL, 447, L121+
- Lombardi J. C., Sills A., Rasio F. A., Shapiro S. L., 1999, Journal of Computational Physics, 152, 687
- Lombardi J. C., Thrall A. P., Deneva J. S., Fleming S. W., Grabowski P. E., 2003, MNRAS, 345, 762
- Lombardi Jr. J. C., Proulx Z. F., Dooley K. L., Theriault E. M., Ivanova N., Rasio F. A., 2006, ApJ, 640, 441
- Lombardi Jr. J. C., Rasio F. A., Shapiro S. L., 1995, ApJL, 445, L117

- Lombardi Jr. J. C., Rasio F. A., Shapiro S. L., 1996a, ApJ, 468, 797
- Lombardi Jr. J. C., Rasio F. A., Shapiro S. L., 1996b, ApJ, 468, 797
- Lombardi Jr. J. C., Warren J. S., Rasio F. A., Sills A., Warren A. R., 2002a, ApJ, 568, 939
- Lombardi Jr. J. C., Warren J. S., Rasio F. A., Sills A., Warren A. R., 2002b, ApJ, 568, 939
- Looney L. W., Tobin J. J., Fields B. D., 2006, ApJ, 652, 1755
- Mackey A. D., Broby Nielsen P., Ferguson A. M. N., Richardson J. C., 2008, ApJL, 681, L17
- Mackey A. D., Gilmore G. F., 2003, MNRAS, 338, 85
- Mackey A. D., Wilkinson M. I., Davies M. B., Gilmore G. F., 2007, MNRAS, 379, L40
- Maeder A., Meynet G., 2000a, A&A, 361, 159
- Maeder A., Meynet G., 2000b, ARA&A, 38, 143
- Maíz Apellániz J., 2008, ApJ, 677, 1278
- Makino J., 2001, in Deiters S., Fuchs B., Just A., Spurzem R., Wielen R., eds, Dynamics of Star Clusters and the Milky Way Vol. 228 of Astronomical Society of the Pacific Conference Series, Direct Simulation of Dense Stellar Systems with GRAPE-6. pp 87–+
- Makino J., Fukushige T., Koga M., Namura K., 2003, PASJ, 55, 1163
- Makino J., Taiji M., Ebisuzaki T., Sugimoto D., 1997, ApJ, 480, 432
- Marks M., Kroupa P., Baumgardt H., 2008, MNRAS, 386, 2047
- Massey P., Hunter D. A., 1998, ApJ, 493, 180
- McCrady N., Graham J. R., Vacca W. D., 2005, ApJ, 621, 278
- McMillan S. L. W., 1986, ApJ, 306, 552
- McMillan S. L. W., Vesperini E., Portegies Zwart S. F., 2007, ApJL, 655, L45
- Meaburn J., Hebden J. C., Morgan B. L., Vine H., 1982, MNRAS, 200, 1P
- Merritt D., Piatek S., Portegies Zwart S., Hemsendorf M., 2004a, ApJL, 608, L25
- Merritt D., Piatek S., Portegies Zwart S., Hemsendorf M., 2004b, ApJL, 608, L25
- Moffat A. F. J., Poitras V., Marchenko S. V., Shara M. M., Zurek D. R., Bergeron E., Antokhina E. A., 2004, AJ, 128, 2854
- Monaghan J. J., 1992, ARA&A, 30, 543

- Monaghan J. J., 2002, MNRAS, 335, 843
- Monaghan J. J., 2005, Reports on Progress in Physics, 68, 1703
- Noyola E., Gebhardt K., 2007, AJ, 134, 912
- Nugis T., Lamers H. J. G. L. M., 2000, A&A, 360, 227
- O'Connell R. W., Gallagher III J. S., Hunter D. A., Colley W. N., 1995, ApJL, 446, L1+
- Owocki S. P., Gayley K. G., Shaviv N. J., 2004, ApJ, 616, 525
- Owocki S. P., van Marle A. J., 2008, ArXiv e-prints, 801
- Paxton B., 2004, PASP, 116, 699
- Petrovic J., Pols O., Langer N., 2006, A&A, 450, 219
- Piatti A. E., Bica E., Claria J. J., 1998, A&AS, 127, 423
- Pinsonneault M. H., Kawaler S. D., Sofia S., Demarque P., 1989, ApJ, 338, 424
- Piotto G., Bedin L. R., Anderson J., King I. R., Cassisi S., Milone A. P., Villanova S., Pietrinferni A., Renzini A., 2007, ApJL, 661, L53
- Pols O. R., Tout C. A., Eggleton P. P., Han Z., 1995, MNRAS, 274, 964
- Portegies Zwart S., Gaburov E., Chen H.-C., Gürkan M. A., 2007a, MNRAS, 378, L29
- Portegies Zwart S., Gaburov E., Chen H.-C., Gürkan M. A., 2007b, MNRAS, 378, L29
- Portegies Zwart S. F., Baumgardt H., Hut P., Makino J., McMillan S. L. W., 2004, Nature, 428, 724
- Portegies Zwart S. F., Makino J., McMillan S. L. W., Hut P., 1999, A&A, 348, 117
- Portegies Zwart S. F., McMillan S. L. W., 2002, ApJ, 576, 899
- Portegies Zwart S. F., McMillan S. L. W., Hut P., Makino J., 2001, MNRAS, 321, 199
- Portegies Zwart S. F., van den Heuvel E. P. J., 2007, Nature, 450, 388
- Portegies Zwart S. F., Verbunt F., 1996, A&A, 309, 179
- Price D. J., 2007, Publications of the Astronomical Society of Australia, 24, 159
- Price D. J., Monaghan J. J., 2007, MNRAS, 374, 1347
- Pumo M. L., D'Antona F., Ventura P., 2008, ApJL, 672, L25
- Rasio F. A., Lombardi Jr. J. C., 1999, Journal of Computational and Applied Mathematics, 109, 213

- Rasio F. A., Shapiro S. L., 1994, ApJ, 432, 242
- Rogers F. J., Iglesias C. A., 1992, ApJS, 79, 507
- Salpeter E. E., 1955, ApJ, 121, 161
- Scheepmaker R. A., Haas M. R., Gieles M., Bastian N., Larsen S. S., Lamers H. J. G. L. M., 2007, A&A, 469, 925
- Seaton M. J., Yan Y., Mihalas D., Pradhan A. K., 1994, MNRAS, 266, 805
- Sills A., Adams T., Davies M. B., 2005, MNRAS, 358, 716
- Sills A., Adams T., Davies M. B., Bate M. R., 2002, MNRAS, 332, 49
- Sills A., Faber J. A., Lombardi Jr. J. C., Rasio F. A., Warren A. R., 2001, ApJ, 548, 323
- Sills A., Lombardi Jr. J. C., Bailyn C. D., Demarque P., Rasio F. A., Shapiro S. L., 1997, ApJ, 487, 290
- Spitzer L., 1987, Dynamical evolution of globular clusters. Princeton, NJ, Princeton University Press, 1987, 191 p.
- Springel V., 2005, MNRAS, 364, 1105
- Springel V., Hernquist L., 2002, MNRAS, 333, 649
- Stahler S. W., Palla F., 2005, The Formation of Stars. The Formation of Stars, by Steven W. Stahler, Francesco Palla, pp. 865. ISBN 3-527-40559-3. Wiley-VCH , January 2005.
- Stancliffe R. J., Glebbeek E., Izzard R. G., Pols O. R., 2007, A&A, 464, L57
- Sternberg A., 1998, ApJ, 506, 721
- Stolte A., Brandner W., Grebel E. K., Lenzen R., Lagrange A.-M., 2005, ApJL, 628, L113
- Stolte A., Grebel E. K., Brandner W., Figer D. F., 2002, A&A, 394, 459
- Sugimoto D., Bettwieser E., 1983, MNRAS, 204, 19P
- Suzuki T. K., Nakasato N., Baumgardt H., Ibukiyama A., Makino J., Ebisuzaki T., 2007a, ApJ, 668, 435
- Suzuki T. K., Nakasato N., Baumgardt H., Ibukiyama A., Makino J., Ebisuzaki T., 2007b, ArXiv Astrophysics e-prints
- Suzuki T. K., Nakasato N., Baumgardt H., Ibukiyama A., Makino J., Ebisuzaki T., 2007c, ApJ, 668, 435
- Turner J. A., Chapman S. J., Bhattacharyya A. S., Disney M. J., Pongracic H., Whitworth A. P., 1995, MNRAS, 277, 705

- Umbreit S., Chatterjee S., Rasio F. A., 2008, ApJL, 680, L113
- Šubr L., Kroupa P., Baumgardt H., 2008, MNRAS, 385, 1673
- Vesperini E., Heggie D. C., 1997, MNRAS, 289, 898
- Vink J. S., de Koter A., 2005, A&A, 442, 587
- Vink J. S., de Koter A., Lamers H. J. G. L. M., 2000, A&A, 362, 295
- Vink J. S., de Koter A., Lamers H. J. G. L. M., 2001, A&A, 369, 574
- Weidner C., Kroupa P., 2004, MNRAS, 348, 187
- Whitmore B. C., Schweizer F., 1995, AJ, 109, 960
- Yoon S.-C., Langer N., 2005, A&A, 443, 643
- Yungelson L. R., van den Heuvel E. P. J., Vink J. S., Portegies Zwart S. F., de Koter A., 2008, A&A, 477, 223
- Zinnecker H., Yorke H. W., 2007, ARA&A, 45, 481